MASTER'S THESIS

Spatio-Temporal Control of Thin Liquid Films on Switchable Substrates

Submitted by:

JANIK SUER

September 23, 2022

First examiner:
PD DR. SVETLANA GUREVICH
Second examiner:
PROF. DR. UWE THIELE

University of Münster
Institute for Theoretical Physics

PUBLICATIONS

This thesis resulted in two publications. [2] includes a tutorial for the reproduction of the results presented in chapter 3. In addition to the tutorial the required software is provided. In [1] some of the results presented in section 4.2 will be published.

[1] Janik Suer, Moritz Stieneker, and Svetlana Gurevich. "Control of transversally invariant liquid ridges on prestructured switchable substrates." In preparation.

[2] Janik Suer, Moritz Stieneker, Svetlana Gurevich, and Simon Hartmann. "Implementation of the Thin-Film Equation on Prestructured, Switchable Substrates Using the oomph-lib Library." In: (Jan. 2022). DOI: 10.5281/zenodo.5821537. URL: https://doi.org/10.5281/zenodo.5821537.

CONTENTS

1 INTRODUCTION

Controlling and manipulating the dynamics of liquids is an essential prerequisite in many fabrication processes like inkjet printing [27] or wire coating [38]. Various methods exist to control the structure formation of a liquid. One of these methods consist of utilizing the naturally occurring Plateau-Rayleigh instability, a transversal instability of elongated liquid structures, to obtain the desired positioning of the liquid [33, 35, 36].
A second method employed to control liquid deposition are heterogeneous substrates. These are widely used in coating processes, where they are applied to induce a structured deposition of the molecules. Examples include experiments by Wang et al. using a silicon-oxide substrate with gold stripes [53, 54] as well as dip-coating using a chemically micropatterned substrate [7]. In addition to this, Berbezier et al. studied the dewetting of thin silicon films on a substrate prepatterned by electron lithography. Also in the fabrication process of quantum dots, the application of heterogeneous substrates was investigated [26]. Early experimental investigations of a heterogeneous inclined substrate were performed in [6], where a wettability gradient was employed to induce an uphill movement of a liquid droplet.
Various numerical investigations of liquid dynamics on heterogeneous substrates were performed. Ref. [29] studies nanodroplets placed near a chemicals step pattern. The step corresponds to a heterogeneous wettability of the substrate, resulting in a motion of the liquid. The dynamics of a droplet on a one-dimensional substrate are modelled in [51] by using a long-wave extension of the Stokes equation with a finite slip length. The dynamics of transversally invariant liquid ridges on prestructured substrates were studied in [25] using the minimization of a macroscopic interface free energy, as well as by bifurcation analysis in [5, 48], where mesoscopic free energies were applied.
While the previously mentioned examples only consider one-dimensional patterned substrates or one-dimensional simplifications of two-dimensional substrates, direct numerical simulations of two-dimensional prepatterned substrates were performed in [1, 48], where the latter considers the depinning of liquid structures on heterogeneous inclined substrates. Here Beltrame et al. also encountered the previously mentioned Plateau-Rayleigh instability. The dynamics of liquid droplets on heterogeneous, inclined substrates are studied in [13]. Engelnkemper et al. also considered the dynamics and bifurcations exhibited by sliding droplets on an inclined homogeneous substrate in [14] and here encountered the so-called Pearling instability. Another

way to control the liquid's behaviour is the application of prestructured, switchable substrates. These allow the control of the substrate's wettability using different kinds of stimuli, such as illumination with light of a given wavelength, a change of temperature or applying an electrical potential [56]. Prominent examples include inorganic materials such as TiO2 or ZnO, that allow a significant change of the contact angle between the hydrophilic and the hydrophobic case [16, 44, 52]. Significantly faster switching processes are found in self-assembled monolayers (SAM) consisting of molecules with azobenzene or other photo-responsive moieties [24, 37, 57]. An example of a direct application of switchable substrates is [22], where the movement of a droplet was guided reversibly through asymmetrical irradiation of the surface with light, i. e., by changing the wettability close to the droplet.

In addition to the various experimental considerations of liquid films on prestructured switchable substrates, diverse numerical investigations were made. These include the research by Grawitter and Stark, who employed the boundary element method to solve the Stokes equation. They investigated a liquid droplet on a discretely switched substrate and a droplet advected by a moving wettability step, equivalent to a continuously switched substrate [18]. Grawitter and Stark also studied the dynamics of a droplet on a periodically switched substrate [17]. A comparison of the results obtained from numerical simulations of the mesoscopic thin-film equation with the results of molecular dynamics simulations was performed by Stieneker et al. They investigated a droplet experiencing a single instantaneous switch of the substrate's wettability [41] and the behaviour of a droplet on a periodically switched substrate [49]. A combination of experimental and numerical investigations were performed by Honnigfort et al. using arylazopyrazole phosphonic acids as photoswitchable molecules on an oxide substrate and numerical investigations employing molecular dynamics simulations [21].

Within this thesis, switchable, prestrucuted substrates will be investigated as a control mechanism for the dynamics of liquid structures. All investigations are performed employing direct numerical simulations of the mesoscopic thin-film equation [20, 46]. The simulations are performed using the finite element method implemented by the open-source library OOMPH-LIB [19].
The outline of this thesis is as follows. Chapter 2 lays the theoretical groundwork onto which all further investigations are based. For this section 2.1 introduces the thin-film equation and section 2.2 explains the employed numerical methods. The first part of the results section, i. e., chapter 3 and chapter 4, considers horizontal substrates. In chapter 3, a one-dimensional heterogeneous substrate is investigated. A moving wettability profile is employed to advect a liquid droplet. For the moving one-dimensional droplet, the maximum advection velocity and its dependence on the wettability parameters are determined.

From chapter 4 onward the considered system is extended into a second dimension. In section 4.1 an attempt is made to extend the results obtained for the one-dimensional moving wettability profile to the two-dimensional case, leading to a good agreement for the appropriate two-dimensional extension of the 1D system. Within section 4.2 the Plateau-Rayleigh instability is investigated. To understand the dynamics of the liquid during the Plateau-Rayleigh instability, numerical simulations of liquid ridges undergoing this kind of instability are performed in section 4.2.1. Here, the Plateau-Rayleigh instability could be observed and the meta-stable states, used in the later sections, extracted. Additionally, in section 4.2.2 the applications of switchable substrates on a liquid exhibiting a Plateau-Rayleigh instability are being investigated in an attempt to obtain stable versions of the meta-stable states observed in section 4.2.1. Section 4.2.3 examines the interaction of two liquid ridges in close proximity which both display a Plateau-Rayleigh instability.
In chapter 5 an inclination angle of the substrate will be introduced, resulting in a driving force down the incline. On this inclined substrate, the Pearling instability can be observed, which will be discussed in section 5.1. Section 5.2 considers multiple control mechanisms for the liquid dynamics on an incline. In section 5.2.1 a time-dependent inclination angle will be employed and applied to prevent the Pearling instability discussed in section 5.1. Section 5.2.2 investigates the pinning of droplets on a substrate with a temporally constant wettability profile. Including periodic switches of the wettability pattern, periodically pinned droplets can be obtained, which will be discussed in section 5.2.3. Moving wettability profiles will be considered again for an inclined substrate in section 5.2.3. Here, they will be employed to alter the sliding velocity of droplets flowing down the incline, which will be investigated as a method to prevent and induce the Pearling instability. Finally, a summary of the obtained results and an outlook will be given in chapter 6.

2 THEORETICAL BACKGROUND

This chapter is dedicated to the discussion of the theoretical basis on which the performed examinations are based. First, the employed thin-film model describing the height of a liquid film on a solid substrate will be introduced, after which the numerical tools applied to analyse this non-linear partial differential equation are explained.

2.1 THIN-FILM EQUATION

Within this work, a viscous Newtonian fluid on a solid substrate will be considered. The dynamics of incompressible viscous Newtonian fluids can be described by a set of differential equations called Navier-Stokes equations. The Navier-Stokes equations need to be accompanied by suitable boundary conditions in order to model the considered free-surface liquid film on a solid substrate. These boundary conditions include no-slip and no-penetration boundary conditions at the liquid-solid interface, as well as normal and tangential stress conditions and a kinematic condition at the liquid-gas interface [50]. An illustration of a one-dimensional liquid film on an inclined substrate is shown in fig. 2.1. Here, additionally, the liquid-solid and liquid-gas interface regions are marked by a dashed green and red lines, respectively. The assumption of thin liquid films, i. e., a small extension of the liquid orthogonal to the substrate relative to its extension parallel to the substrate, simplifies the Navier-Stokes equations. This approximation is called long-wave or lubrication approximation [30] and results in the thin-film equation, which reads:

$$\partial_t h(\mathbf{x}, t) = \nabla \left\{ Q(h) \left[\nabla P(h, \mathbf{x}, t) + G\boldsymbol{\alpha} \right] \right\}. \tag{2.1}$$

Here $h(\mathbf{x}, t)$ is the local film height at position $\mathbf{x}$ and time t. Note that bold variables are used to denote vectors. Within this thesis, either a one- or a two-dimensional thin-film equation will be considered. For the one-dimensional case $\mathbf{x}$ corresponds to $x \in \mathcal{D}_1 \subset \mathbb{R}$ whereas for the two-dimensional case $\mathbf{x} = (x, y)^T \in \mathcal{D}_2 \subset \mathbb{R}^2$. In the following $\mathcal{D}$ will be used to denote the general domain without specification of the dimensionality. Further, $Q(h)$ given by

$$Q(h) = \frac{h^3}{3\eta}, \tag{2.2}$$

is the mobility coefficient for a fluid with the dynamic viscosity η. It stems from the employed no-slip boundary conditions, which correspond to a vanishing liquid velocity parallel to the substrate at the

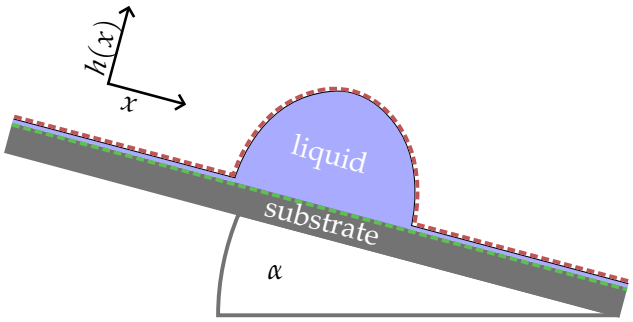

Figure 2.1: A sketch of a droplet on a substrate inclined by the inclination angle α. The liquid and substrate are marked with blue and grey colours, respectively, while the liquid-gas and liquid-solid interfaces are painted with dotted green and red lines, respectively. The coordinate system is defined such that the x-axis is oriented parallel to the substrate, and the height is defined orthogonal to it.

liquid-solid interface. There are other possible boundary conditions at the liquid substrate interface which lead to different mobilities, e. g. the Navier slip condition, which assumes the existence of a finite slip length such that the velocity of the fluid parallel to the substrate at the liquid-solid interface does not vanish [30]. This boundary condition results in a mobility quadratic in h [20].
The term $G\boldsymbol{\alpha}$ describes the driving force down the incline, where G is the gravitation number, and $\boldsymbol{\alpha}$ is a vector describing the inclination along each spatial dimension. In the one-dimensional case it corresponds to the scalar inclination angle $\boldsymbol{\alpha} = \alpha$, whereas for the two-dimensional case it is given by $\boldsymbol{\alpha} = (\alpha_x, \alpha_y)^T$. In the following only inclinations along the x-axis will be considered, i. e., $\boldsymbol{\alpha} = (\alpha_x, 0)^T = (\alpha, 0)^T$.
The remaining part of the thin-film equation 2.1 is the generalized pressure $P(\mathbf{x}, t)$, given by

$$P(h, \mathbf{x}, t) = -\gamma \Delta h(\mathbf{x}, t) - \Pi(h, \mathbf{x}, t). \tag{2.3}$$

Here the first term, including the surface tension γ, is the so-called Laplace pressure, which is a result of the surface tension at the gas-liquid interface. The second term in eq. (2.3) is the disjoining (or Derjaguin) pressure $\Pi(h, \mathbf{x}, t)$, that describes the interaction of the liquid and the substrate [8, 9, 39]. It is given by

$$\Pi(h, \mathbf{x}, t) = \left(\frac{B}{h^6} - \frac{A}{h^3} \right) [1 + \omega(\mathbf{x}, t)], \tag{2.4}$$

and combines long-range attractive van der Waals and short-range repulsive interactions with the corresponding long- and short-range Hamaker-type constants A and B, respectively [46]. Other forms of the disjoining pressure can also be applied, see, e. g. [48]. The disjoining pressure includes a modulation term $1 + \omega(\mathbf{x}, t)$, where $\omega(\mathbf{x}, t)$

corresponds to the spatio-temporal wettability of the substrate. The employed form of the wettability determines the equilibrium structure of a liquid placed on the substrate. In particular, on highly wettable substrates, the liquid will assume an equilibrium position where it is more spread out, i. e., it covers a larger area of the substrate relative to a liquid on a less wettable substrate. Hence, for *increasing* wettability values the substrate becomes *less* wettable. Note that a wettability value of $\omega(\mathbf{x}, t) = -1$ corresponds to the so-called complete wetting case, i. e., due to a vanishing disjoining pressure (cf. eq. (2.4)) the dynamics are entirely determined by the Laplace pressure such that the liquid minimises its curvature and forms a homogeneous film covering the entire substrate.
Note that the thin-film equation (2.1) corresponds to a conservation law and can also be written in a gradient dynamics form [28, 47] as

$$\partial_t h = \nabla \left\{ Q(h) \left[\nabla \frac{\delta \mathcal{F}[h]}{\delta h} \right] + G\boldsymbol{\alpha} \right\}, \tag{2.5}$$

using the free energy functional $\mathcal{F}[h]$, sometimes referred to as the interface Hamiltonian [11]. The generalized pressure, given by eq. (2.3), therefore, corresponds to the variation of the free energy functional with respect to the film height

$$P(h, \mathbf{x}, t) = \frac{\delta \mathcal{F}[h]}{\delta h}. \tag{2.6}$$

For systems dominated by capillarity and wettability, the free energy functional in the lubrication approximation is given by

$$\mathcal{F}[h] = \int_{\mathcal{D}} \left[\frac{1}{2} \gamma \left(\nabla h \right)^2 + f(h, \mathbf{x}, t) \right] d\mathbf{x}. \tag{2.7}$$

Here the first term corresponds to the Laplace pressure in eq. (2.3) while the second term, called the wetting potential, is related to the disjoining pressure through

$$\Pi(h, \mathbf{x}, t) = \partial_h f(h, \mathbf{x}, t). \tag{2.8}$$

As it can be seen in fig. 2.2, the wetting potential exhibits a minimum at a finite film height $h = (B/A)^{1/3} = h_p$. Due to eq. (2.8) the disjoining pressure vanishes for $h = h_p$, which, similar to the complete wetting case, leads to the formation of a thin liquid film of height h_p, called the precursor film [3, 8, 31], covering the entire substrate. This thin liquid layer is also displayed in fig. 2.1.

A relevant macroscopical parameter which will be mentioned frequently in the following sections is the so-called contact angle θ. It is the angle spanned between substrate and the tangent of the height profile at the contact line, i. e., the point at which all three phases meet. Due to the presence of the precursor film and the resulting smooth

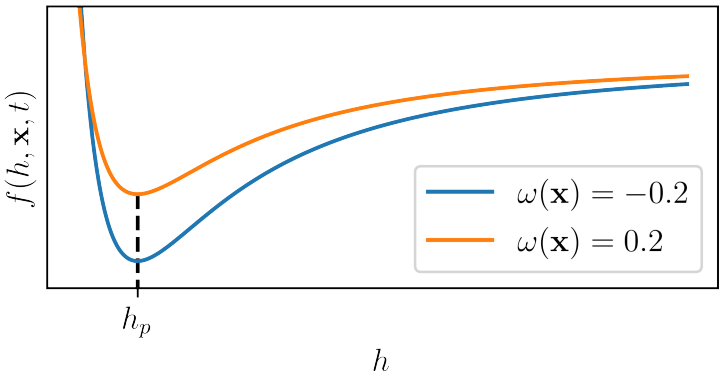

Figure 2.2: Wetting potential $f(h, \mathbf{x}, t)$ for different constant wettability values $\omega(\mathbf{x}, t) = \omega = \text{const.}$ shown as a function of the film height h. The precursor film height h_p for which the wetting potential exhibits a local minimum is marked.

transition between the droplet and the precursor film, a concrete definition of the contact line is difficult. However, since the contact angle will not be measured within this work, only a phenomenological definition is required.

2.2 NUMERICAL DETAILS

To numerically integrate the previously discussed thin-film equation, the open-source library OOMPH-LIB [19] is being employed. It implements the finite element method and includes various helpful tools for the numerical integration, e. g. an adaptive mesh and adaptive time-stepping. In the following, the finite element method will be discussed. Additionally, the residuals and Jacobian necessary for the numerical integration of the thin-film equation (2.1) will be derived. For a more mathematically rigorous discussion, see, e. g. [4, 55].

2.2.1 *Weak Solution*

In order to integrate the thin-film equation (2.1) using the finite element method, it has to be turned into a system of second-order partial differential equations. This can be achieved by introducing the new variable $u = P(h, \mathbf{x}, t)$ such that:

$$u = P(h, \mathbf{x}, t) = -\Delta h - \Pi(h, \mathbf{x}, t), \tag{2.9}$$

$$\partial_t h = \nabla \left\{ Q(h) \left[\nabla u + G\boldsymbol{\alpha} \right] \right\}. \tag{2.10}$$

Rewriting this problem in the residual form one obtains:

$$\mathcal{R}_u(h, \mathbf{x}, t) = -u - \Delta h - \Pi(h, \mathbf{x}, t) = 0, \tag{2.11}$$

$$\mathcal{R}_h(h, \mathbf{x}, t) = \partial_t h - \nabla \left\{ Q(h) \left[\nabla u + G\alpha \right] \right\} = 0. \tag{2.12}$$

The classical (or strong) solution to this problem fulfils these residuals for each point within the considered domain $\mathcal{D}$, i. e., $\mathcal{R}_u(h, \mathbf{x}, t) = \mathcal{R}_h(h, \mathbf{x}, t) = 0$, $\forall\, \mathbf{x} \in \mathcal{D}$ as well as the imposed boundary conditions. During this section Neumann boundary conditions are employed, i. e., no flux through the boundary of the domain $\nabla_\perp h(\mathbf{x}) = 0\, \forall\, \mathbf{x} \in \partial\mathcal{D}$, where $\nabla_\perp$ denotes the projection of the gradient onto the vector normal to the boundary of the domain $\partial\mathcal{D}$.
Since we are using the finite element method, a specification of the Galerkin method, we are interested in the weak formulation of the problem. The benefit of using the weak formulation is that it loosens the differentiability conditions for the solution [4]. The weak solution constitutes a solution that satisfies the imposed boundary conditions as well as the so-called weighted residuals, which in the considered case are given by

$$r_u = \int_{\mathcal{D}} \mathcal{R}_u(h, \mathbf{x}, t)\psi^{\text{test}}(\mathbf{x})d\mathbf{x}, \tag{2.13}$$

$$r_h = \int_{\mathcal{D}} \mathcal{R}_h(h, \mathbf{x}, t)\psi^{\text{test}}(\mathbf{x})d\mathbf{x}, \tag{2.14}$$

for any test function $\psi^{\text{test}}(\mathbf{x})$ that satisfy the homogeneous boundary conditions [15]

$$\psi^{\text{test}}(\mathbf{x}) = 0,\ \forall\, \mathbf{x} \in \partial\mathcal{D}. \tag{2.15}$$

The condition that the weak solution must fulfil the weighted residual for *any* test function results in an equality between the weak and strong solution [45]. Therefore, it is sufficient to determine the weak solution of the problem.
Equation (2.15) can be utilised to eliminate the second-order derivatives from the weighted residuals. For this, one first has to integrate by parts and apply the divergence theorem. For r_u this procedure results in

$$\begin{aligned} r_u = &\int_{\mathcal{D}} \left[-u - \Pi(h, \mathbf{x}, t)\right] \psi^{\text{test}} + (\nabla h)\nabla\psi^{\text{test}} d\mathbf{x} \\ &- \int_{\partial\mathcal{D}} (\mathbf{n}\nabla h)\, \psi^{\text{test}} ds. \end{aligned} \tag{2.16}$$

Here $\mathbf{n}$ is the normal vector to the domain boundary $\partial\mathcal{D}$ while ds is a line element on the boundary. Since due to eq. (2.15) the test functions vanish at the boundary of the domain, the last integral is equal to zero, and the weighted residual reduces to

$$r_u = \int_{\mathcal{D}} \left[-u - \Pi(h, \mathbf{x}, t)\right] \psi^{\text{test}} + (\nabla h)\, \nabla\psi^{\text{test}} d\mathbf{x}. \tag{2.17}$$

Using the same method one is able to shift the spatial derivative from $\nabla\left\{Q(h)\left[\nabla u + G\alpha\right]\right\}$ to the test function in the weighted residual r_h resulting in

$$\begin{aligned} r_h = &\int_{\mathcal{D}} \partial_t h\psi^{\text{test}} - Q(h)\left[\nabla u + G\alpha\right] \nabla\psi^{\text{test}} d\mathbf{x} \\ &- \int_{\partial\mathcal{D}} Q(h)\vec{n}\nabla\left[\nabla u + G\alpha\right] \psi^{\text{test}} ds \end{aligned} \tag{2.18}$$

Where the last integral again vanishes due to eq. (2.15) leading to the weighted residual

$$r_h = \int_{\mathcal{D}} \partial_t h \psi^{\text{test}} - Q(h) \left[\nabla u + G\alpha\right] \nabla \psi^{\text{test}} d\mathbf{x}. \tag{2.19}$$

2.2.2 *Galerkin Method*

In this section, the Galerkin method is used to obtain a discretised version of the continuous problem. The ansatz functions for $h(\mathbf{x}, t)$ and $u(\mathbf{x}, t)$ can be expanded in terms of an infinite set of basis functions

$$\phi_i(\mathbf{x}), \text{ for } i = 1, ..., \infty, \tag{2.20}$$

leading to

$$h(\mathbf{x}, t) = \sum_{i=1}^{\infty} H_i(t)\phi_i(\mathbf{x}), \;\; u(\mathbf{x}, t) = \sum_{i=1}^{\infty} U_i(t)\phi_i(\mathbf{x}). \tag{2.21}$$

The time-dependent functions $H_i(t)$ and $U_i(t)$ are the expansion coefficients of the height profile $h(\mathbf{x}, t)$ and the helper function $u(\mathbf{x}, t)$, respectively. The expansions given in eq. (2.21) are exact, however, in practice, the sum is truncated after a finite number of terms, i. e., only M basis functions and expansion coefficients are being used, with $M \in \mathbb{N}$. The solution of this system leads to an approximate solution $\tilde{h}(\mathbf{x}, t)$ which for $M \to \infty$ converges to the exact solution $\tilde{h}(\mathbf{x}, t) \to h(\mathbf{x}, t)$. Note that only the approximate solution will be considered in the following, the tilde will, therefore, be dropped.
The Galerkin approach itself consists of expanding the test function in the same basis functions as the height profile $h(\mathbf{x}, t)$ and helper function $u(\mathbf{x}, t)$

$$\psi^{\text{test}}(\mathbf{x}, t) = \sum_{i=1}^{M} \Psi_i(t)\phi_i(\mathbf{x}), \tag{2.22}$$

with $\Psi_i(t)$ being the time-dependent expansion coefficients of the test function. Note that the time dependence of all expansion coefficients will be dropped in the following to allow for a more compact notation. Due to the performed expansion, the condition of vanishing residuals for all test functions $\psi^{\text{test}}(\mathbf{x}, t)$ translates to vanishing residuals for all expansion coefficients $\Psi_i(t)$. Employing the expansion of the test functions, the residual r_h has the form

$$\begin{aligned} r_h &= \sum_{i=1}^{M} \int_{\mathcal{D}} \partial_t h \Psi_i \phi_i(\mathbf{x}) - Q(h) \left[\nabla u + G\alpha\right] \nabla \Psi_i \phi_i(\mathbf{x}) d\mathbf{x} \\ &= \sum_{i=1}^{M} \Psi_i r_{h,i} = 0, \end{aligned} \tag{2.23}$$

where the expansion coefficients of the test function Ψ_i have been moved out of the integral, while the corresponding basis function remains in the residual

$$r_{h,i} = \int_{\mathcal{D}} \partial_t h \phi_i(\mathbf{x}) - Q(h) \nabla u \nabla \phi_i(\mathbf{x}) d\mathbf{x}. \tag{2.24}$$

Here i is the index of the basis function. The condition that eq. (2.23) needs to be fulfilled for all expansion coefficients Ψ_i leads to M equations of the form

$$r_{h,i} = 0 \tag{2.25}$$

by exploiting the condition that eq. (2.23) must hold for any set of expansion coefficients Ψ_i, i. e., setting all expansion coefficients except one equal to zero.
Analogously one can arrive at a system of M equations starting with the residuals of the helper function u. In total, the system, therefore, includes $2M$ equations with $2M$ unknowns and can thus be solved numerically using, e. g. a newton solver [10].

2.2.3 *Jacobian*

Using the discretised residuals $r_{u,i}$, $r_{h,i}$, where i is again the index of the test function, to calculate the Jacobian analytically, one is able to avoid the computationally complex numerical assembly of the Jacobian. Including the expansion coefficients of the test functions in the integral (c.f. eq. (2.24)) and using the abbreviation $\psi_i^{\text{test}} = \Psi_i(t)\phi_i(x)$ one obtains for the residual $\tilde{r}_{h,i} = \Psi_i(t) r_{h,i}$ (cf. eq. (2.23))

$$\tilde{r}_{h,i} = \int_{\mathcal{D}} \partial_t h \psi_l^{\text{test}} - Q(h) \nabla u \nabla \psi_l^{\text{test}} d\mathbf{x}. \tag{2.26}$$

The entries of the Jacobian of the system are given as the partial derivatives of the residuals with respect to the expansion coefficients $H_i(t)$ and $U_i(t)$ of $h(\mathbf{x}, t)$ and $u(\mathbf{x}, t)$, respectively. One, therefore, obtains the following entries

$$\begin{aligned}
J_{h;l,H;m} = \frac{\partial r_{h,l}}{\partial H_m} &= \int_{\mathcal{D}} -\partial_{H;m} \partial_t H_m \phi_m \\
&\qquad + \partial_h Q(h) \phi_m \left(\partial_x u + G\boldsymbol{\alpha}\right) \nabla \psi_l^{\text{test}}, \\
J_{h;l,U;m} = \frac{\partial r_{h,l}}{\partial U_m} &= \int_{\mathcal{D}} Q(h) \partial_x \phi_m \partial_x \psi_l^{\text{test}} d\mathbf{x}, \\
J_{u;l,H;m} = \frac{\partial r_{u,l}}{\partial H_m} &= \int_{\mathcal{D}} -\partial_h \Pi(h, \mathbf{x}, t) \phi_m \psi_l^{\text{test}} d\mathbf{x}, \\
J_{u;l,U;m} = \frac{\partial r_{u,l}}{\partial U_m} &= \int_{\mathcal{D}} -\phi_m \psi_l^{\text{test}} d\mathbf{x}.
\end{aligned} \tag{2.27}$$

2.2.4 *Finite Element Method*

The finite element method is an implementation of the Galerkin method. It employs the method discussed in sec. 2.2.2 to determine

the solution over the entire domain numerically. To apply the Galerkin method, the domain must first be discretised into *finite elements*. At the edges of these elements, nodes are introduced such that for a one-dimensional domain N elements, i. e., line segments in the one-dimensional case lead to N nodes. In addition to the mesh itself, the basis functions denoted as $\Psi_i(\mathbf{x})$ must be defined. For the finite element method, the basis functions are chosen to have only a finite support, i. e., they only deviate from zero in a small number of elements. The simplest form of a one-dimensional domain of size L, i. e., $\mathbf{x} = x \in \mathcal{D}_1 = [0, L]$ with equally spaced nodes is portrayed in fig. 2.3 a). Here continuous piece-wise linear basis (or shape) functions $\Psi_i(x)$ given by eq. (2.28), where X_i denotes the x-coordinate of the x-th node, are also depicted. In fig. 2.3 b), the approximations of a parabolic droplet, used later on as the initial condition, are displayed for $N = 7$ and $N = 20$. One can see that the increased number of nodes greatly increases the smoothness of the approximation.

$$\Psi_i(x) = \begin{cases} 0 & \text{for } x < X_{i-1}, \\ \frac{x - X_{i-1}}{X_i - X_{i-1}} & \text{for } X_{i-1} < x < X_i, \\ \frac{X_{i+1} - x}{X_{i-1} - X_i} & \text{for } X_i < x < X_{i+1}, \\ 0 & \text{for } x > X_{i+1}. \end{cases} \tag{2.28}$$

Due to the finite support of the shape functions, i. e., they vanish everywhere but in the neighbourhood of their assigned nodes, the Jacobian constructed using eq. (2.27) is tridiagonal. Other possible shape functions include, e. g. higher-order polynomials.
For two-dimensional problems, the domain can no longer be separated into line segments. Therefore, different element shapes need to be employed. Common choices include triangles, or rectangles [4]. For the two-dimensional simulations performed later, rectangular elements will be employed.

2.2.5 *Time Stepping*

For the numerical time stepping, a two-step backward differentiation formula (BDF2) will be used. Backward differentiation formula (BDF) are a family of implicit linear multistep methods especially well suited for stiff boundary value problems [43]. Different BDF methods exist, which vary in the number of steps $k \in \mathbb{N}$ being used. For the solution of an initial value problem given by

$$\partial_t y = f(t, y),\ y(t_0) = y_0, \tag{2.29}$$

their general form can be expressed as

$$\sum_{i=0}^{k} \alpha_i y_{n+i} = dt \beta_k f_{n+k}. \tag{2.30}$$

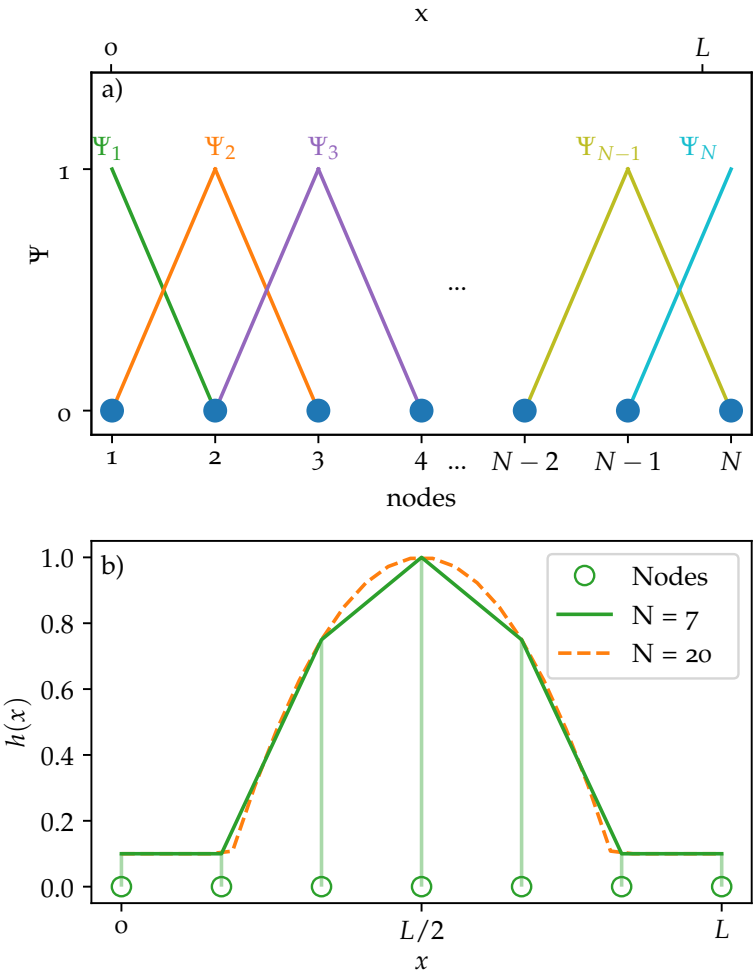

Figure 2.3: a) A schematic of a discretised domain with linear shape functions labelled according to their associated nodes, i. e., the nodes at which their maximum lies. Note that at the left (right) boundary of the domain, the shape function include only the part with a negative (positive) slope. The definition of the shape functions is given by eq. (2.28). b) displays two approximations of a parabolic droplet using $N = 7$ and $N = 20$ base function/nodes marked in green and orange, respectively. Additionally, the positions of the seven nodes are marked by green circles.

Here dt denotes the step size $\alpha_0, ..., \alpha_k$ and β_k are real constants which vary for the different methods, y_{n+i} and f_{n+k} are the value of the function which is to be integrated and the right hand side of the differential equation at time step $n+i$ and $n+k$, respectively. The one-step BDF, therefore, corresponds to the backwards (or implicit) Euler method [23]. Note that only methods with $k < 7$ may be applied as for $k > 6$, the methods become zero-unstable.
For the employed second order or two-step BDF method, the parameters are given as

$$\alpha_0 = 1,\ \alpha_1 = -4,\ \alpha_2 = 3,\ \beta_2 = 2. \tag{2.31}$$

3

1D HORIZONTAL SUBSTRATE

In the following section, a spatially and temporally modulated wettability pattern will be employed as a method to control liquid dynamics on a one-dimensional horizontal substrate. As discussed in section 2.1 the wettability $\omega(\mathbf{x}, t)$ enters the thin-film equation 2.1 as a modulation term of the disjoining pressure (c.f. eq. (2.4)). The wettability will now be considered as time and space dependent, with the employed function being discussed in section 3.1. Initial considerations of the dynamics exhibited by liquid droplets on substrates with a spatio-temporal wettability pattern are performed in section 3.2. Section 3.3 studies the advection of a liquid droplet placed at different initial positions on a moving wettability profile. Section 3.4 considers the maximum droplet speed obtainable by the advection with a moving wettability profile and the influence of the employed wettability parameters on this velocity.

3.1 WETTABILITY PROFILE

A variety of different wettability patterns may be applied to control the liquid dynamics, examples include a logistic step function like in [18], or a moving version of the stripe pattern used in [20, 41, 46], where the latter will be employed in the following.
The used well-like pattern, later also called stripe pattern since the two-dimensional extension corresponds to a highly wettable stripe, consists of an area with high wettability, given by ρ_{HW} and one with low wettability, given by ρ_{LW} with a continuous transition between them. An illustration of the wettability profile is displayed in fig. 3.1. The pattern can be described by

$$\omega(x) = \rho_0 + C_\rho \tanh\left[\frac{x + x_A - c}{ls}\right] \tanh\left[\frac{x - x_A - c}{ls}\right]. \tag{3.1}$$

Where c denotes the centre of the highly wettable part of the profile while x_A corresponds to the distance between the centre and the point of steepest slope, thus, the distance between the two steepest points is given by $2x_A$, as shown in fig. 3.1. The parameter ls determines the steepness of the transition and is equal to ± 1 times the inverse of the slope at $x = c \pm x_A$. In eq. (3.1) and fig. 3.1 the abbreviations ρ_0 and C_ρ are being used, which are defined as

$$\rho_0 = \frac{\rho_{\mathrm{LW}} + \rho_{\mathrm{HW}}}{2}, \quad C_\rho = \frac{\rho_{\mathrm{LW}} - \rho_{\mathrm{HW}}}{2}. \tag{3.2}$$

Here ρ_0 is defined as the mean wettability value, i. e., the wettability value at the points of steepest slope (at $x = c \pm x_A$), while C_ρ is equal

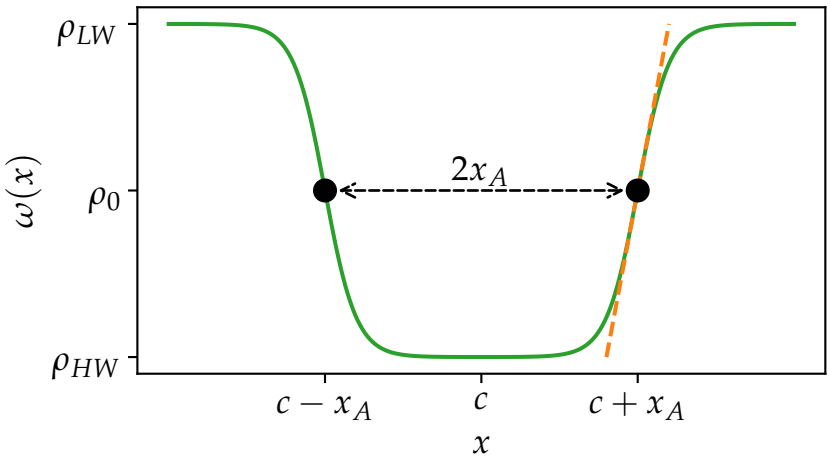

Figure 3.1: The solid lines is equal to the stationary wettability pattern given by eq. (3.1). Displayed as a dotted orange line is the tangent to the wettability profile at $x = x_A$, whose slope is given by the inverse of the parameter ls. The parameters of the wettability pattern relative to the employed domain size are given as $x_A/L = 0.25$, $ls/L = 0.05$.

to the amplitude, i. e., $\rho_{\mathrm{HW}} = \rho_0 - C_\rho$, $\rho_{\mathrm{LW}} = \rho_0 + C_\rho$.
In the following a moving wettability pattern will be considered. To obtain such a pattern a transformation of the x-coordinate is introduced:

$$\tilde{x}(t) = x - v \cdot t, \tag{3.3}$$

which propagates the pattern towards larger (smaller) x-values for positive (negative) velocities v. Since periodic boundary conditions are being applied, it is reasonable to have the wettability pattern obey them. The transformation, therefore, changes to:

$$\tilde{x}(t) = -\frac{L}{2} + \mathrm{mod}\left[\left(\frac{L}{2} + x - c - v \cdot t\right), L\right]. \tag{3.4}$$

Here mod(A, B) with $A, B \in \mathbb{R}$ denotes the modulo function. The transformation additionally has to include the centre position c of the wettability spot. Otherwise, $c \neq 0$ results in discontinuities of the wettability profile.
Plugging eq. (3.4) into eq. (3.1) leads to the following wettability profile:

$$\omega(x,t) = \rho_0 + C_\rho \tanh\left(\frac{\tilde{x}(t) + x_A}{ls}\right) \tanh\left(\frac{\tilde{x}(t) - x_A}{ls}\right). \tag{3.5}$$

3.2 DYNAMICS

As mentioned in sec. 2.1 the open source library OOMPH-LIB will be employed for the numerical simulations. For an in-depth introduction into the employed numerical tools, see [42], which includes a manual for the simulation of liquid droplets on spatio-temporal wettability patterns. For the numerical simulations, the domain size L, the wettability profile parameters, and the initial condition, i. e., the initial height profile $h(x, t = 0)$ need to be specified. To minimise the time required for the equilibration of the liquid to the underlying substrate, it is sensible to choose an initial condition similar to the equilibrium form of the liquid. For the simple stationary wettability profile given by eq. (3.1) a reasonable initial condition, therefore, is a droplet of parabolic shape at the centre of the wettability profile

$$h(x, t = 0) = -a(x - x_0)^2 + h_0. \tag{3.6}$$

Here h_0 is the maximum of the initial film height and x_0 is the initial position of the maximum, i. e., $h(x_0, t = 0) = h_0$. The parameter a determines the form of the droplet and can be calculated by fixing the contact angle to an arbitrary value θ_0. An illustration to visualise the calculation of the parameter a from the contact angle θ_0 is displayed in fig. 3.2, which shows the height profile near the contact point. From eq. (3.6) one obtains the position of the contact point by solving $h(x, t = 0) = 0$[1] for x, leading to

$$x = \pm\sqrt{\frac{h_0}{a}}. \tag{3.7}$$

With eq. (3.6) the slope at the contact line can be determined as

$$\partial_x h \left(x = \pm\sqrt{\frac{h_0}{a}}, t = 0 \right) = \mp\sqrt{4h_0 \cdot a}. \tag{3.8}$$

Using the trigonometric relations for the grey triangle in fig. 3.2 one finds that the slope at the contact line is equal to

$$\left.\frac{dh}{dx}\right|_{x=-\sqrt{h_0/a}} = \tan(\theta_0). \tag{3.9}$$

Where dh and dx denote the side lengths of the triangle marked accordingly in fig. 3.2.
With eqs. (3.8) and (3.9) the parameter a can be determined resulting in the initial condition:

$$h(x, t = 0) = -\frac{1}{4h_0}\tan^2(\theta_o)x^2 + h_0. \tag{3.10}$$

1 One could use the intersection point with the precursor film $h(x, t = 0) = \chi$ but since χ is small, including it does not lead to a significant change.

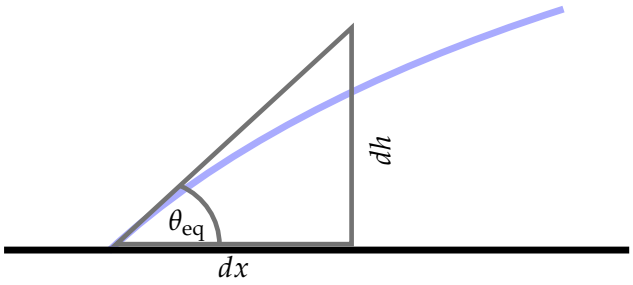

Figure 3.2: Illustration of the height profile close to the contact point of a liquid droplet used to indicate the relation between the steepness of the height profile at the contact line and the contact angle at the contact line. The height profile is marked in blue, while the substrate is displayed as a solid black line. The hypotenuse of the grey triangle corresponds to the tangent of the height profile at the contact line. The other sides of the triangle are marked as dx and dh as their ratio equals the steepness of the height profile at the contact line.

As discussed in section 2.1, the employed form of the disjoining pressure results in the formation of a so-called precursor film covering the entire substrate. The precursor film has to be incorporated into the employed initial condition; otherwise, numerical instabilities arise due to the rapid liquid dynamics. The height of the precursor film is given by the parameter h_p, which is equal to χ due to the parameters employed in the process of nondimensionalisation (c.f. appendix A). In the following, χ will be used to denote the height of the precursor film. Since the minimum film height is equal to the precursor film height, $h(x, t = 0)$ can be written as:

$$h(x, t = 0) = \max\left[-\frac{1}{4h_0}\tan^2(\theta_o)x^2 + h_0,\, \chi\right]. \tag{3.11}$$

Here $\max[A,\, B]$ with $A,\, B \in \mathbb{R}$ denotes the maximum of A and B.
In the following, the initial contact angle $\theta_0 \approx 0.779$ is employed, which, according to eq. (A.11), corresponds to a wettability value of $\omega(x) \approx -0.6$. Since the investigated wettability values lie mainly within the interval $[-1,\, 1]$ and the droplet is exposed to the highly wettable region in most cases, $\theta_0 \approx 0.779$ may be used as a good approximation for all investigations.
If an initial droplet given by eq. (3.10) is placed on the center of a wide enough well, i. e., x_A and ls are chosen such that the base of the droplet in its equilibrium position fits entirely onto the area of high wettability $\omega(x) \approx \rho_{HW}$. It will adapt its form such that the contact angle θ is equal to the equilibrium contact angle θ_{eq} for the wettability value at the droplets position (c.f. eq. (A.11)). The initial and final height profile of such a simulation are shown in fig. 3.3. Here a domain with $L = 30$ and a wettability pattern given by eq. (3.1) using $\rho_{\text{HW}} = -0.9$ and $\rho_{\text{LW}} = 1.0$ are being employed, while all other

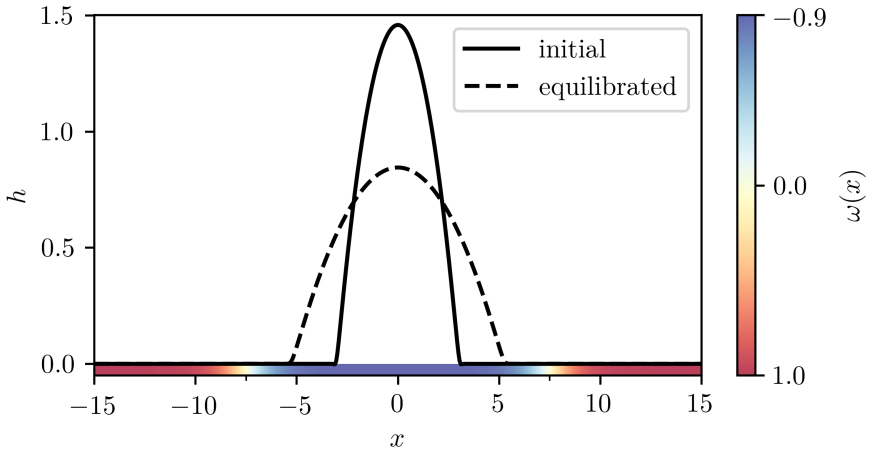

Figure 3.3: Initial and equilibrated state of a droplet placed on a wettability well. The parameters of the profile are chosen analogous to fig. 3.1 with $\rho_{HW} = -0.9$, $\rho_{LW} = 1$, $h_0 = 1.5$ and $L = 30$.

parameters of the wettability profile are chosen analogous to fig. 3.1. It can be seen that the initial droplet, given by eq. (3.10) with $h_0 = 1.5$, which is shown as a solid black line, spreads out significantly once it is exposed to the substrate. The resulting equilibrated droplet portrayed as a dotted black line covers nearly the entire highly wettable patch and exhibits a maximum film height of $h_{max} \approx 0.89$. Decreasing the parameter x_A will result in the droplet experiencing a wettability gradient at the edges of the highly wettable spot once x_A is chosen small enough. Since the disjoining pressure has an increased influence in this area, due to the increasing value of $\omega(x,t)$ it is energetically more favourable for the droplet to decrease the covered area by increasing the curvature of the film, which in turn results in an increased Laplace pressure. If x_A is increased further, the influence of the Laplace pressure will grow, outweighing the disjoining pressure and leading to the droplet covering an increasing amount of the substrate where $\omega(\mathbf{x},t) \neq \rho_{HW}$.

This behavior occurs for all values of ρ_{HW} and ρ_{LW} if $\rho_{HW} < \rho_{LW}$. Since the wettability function $\omega(x)$ modulates the disjoining pressure, the chosen values for ρ_{HW} and ρ_{LW} determine to what extent it is favourable for the droplet to cover only the highly wettable patch. For a decreased contrast between the wettability values, i. e., a decreased C_ρ, the advantage of covering the substrate with $\omega(x) = \rho_{HW}$ over the substrate with $\omega(x) = \rho_{LW}$ also decreases. The droplet will, thus, cross the wettability gradient more easily, i. e., for larger x_A values in case of the previous discussion.

Introducing a propagating wettability profile given by eq. (3.5) results in more involved dynamics. The droplet no longer experiences a constant wettability value but will inevitably be exposed to a wettability gradient once the profile has progressed such that the droplet is near

the transition region at $x = c - x_A - v_{\text{inhom}}t$. Once the droplet is exposed to the wettability gradient, it will not contract, as was the case in the discussion concerning a stationary wettability value. Since it is only exposed to the wettability gradient at one side, i. e., on the left for positive v_{inhom} and $x_0 = 0 = c$, while on the other side, a region of high wettability is still uncovered by the liquid, it will move away from the region of low and towards the region of high wettability, thus, following the motion of the wettability pattern. For long-time simulations of a wettability pattern moving at the constant speed v_{inhom}, the droplet will either end up in a state of equilibrium distance to the wettability pattern or cross the wettability gradient in the transition region, after which it is only exposed to the region of low wettability and ,thus, ceases to move. These two cases are displayed in fig. 3.4, where snapshots of explicit time simulations using a moving inhomogeneity profile given by eq. (3.5) with $x_A = 6$ and $v_{\text{inhom}} = 0.2$ as well as $v_{\text{inhom}} = 0.02$ are portrayed. Both simulations were performed until the centre of the wettability well has reached $x = 12.5$. Thus, both portrayed droplets are exposed to the displayed wettability pattern. For $v_{\text{inhom}} = 0.2$ the droplet is not able to follow the wettability pattern. It crosses the wettability gradient and ceases to move, only being exposed to the low wettability region as displayed in the recorded snapshot. Since the used wettability pattern also obeys the applied periodic boundary conditions, the droplet will be advected periodically each time crossing the wettability gradient and being left behind. For the lower speed of the inhomogeneity, i. e., $v_{\text{inhom}} = 0.02$ the droplet can follow the wettability profile and, after an initial adaption to the substrate, assumes the equilibrium form displayed in fig. 3.4. It moves with the same velocity as the inhomogeneity itself and, therefore, remains at a constant distance to the wettability pattern. Note that the form exhibited by the droplet is not symmetrical but shows an increased steepness at the side exposed to the wettability gradient, as well as the formation of a slight cusp on the opposing side. This structure is due to the increased influence of the disjoining pressure at the left side of the droplet, leading to an increased curvature while the right side spreads out over the highly wettable region.

3.3 DROPLET LEAD

A parameter suitable to describe whether or not a droplet can keep up with the inhomogeneity profile is the droplet lead s, which is defined as the distance between the left point of maximum steepness of the wettability profile, initially at $x = c - x_A$ and the position of maximum height $x_{\max}(t)$ of the film

$$s(t) = x_{\max}(t) - \left[\operatorname{mod}\left(\frac{L}{2} + c - x_A + v_{\text{inhom}}t,\, L\right) - \frac{L}{2}\right]. \quad (3.12)$$

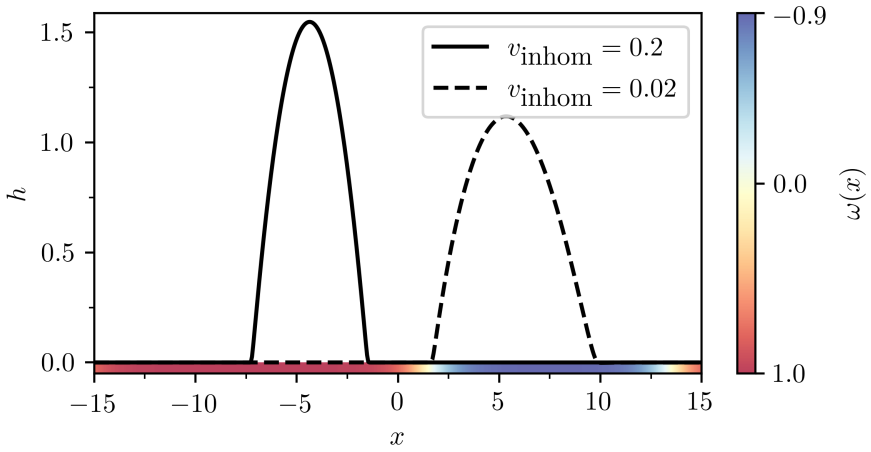

Figure 3.4: Snapshots of two explicit time simulations of a liquid droplet with the initial film height $h_0 = 1.5$ being exposed to a moving wettability profile with two different velocities v_{inhom}. The other parameters are the same as in fig. 3.3 except for $x_A = 5$.

The definition is chosen like this since for positive v_{inhom} the droplet is advected by the wettability gradient at the left point of steepest slope. Thus, it also assumes its equilibrium position relative to this point.
For the case of droplets being able to follow the wettability profile, i. e., the liquid assumes an equilibrium distance to the moving wettability pattern, the droplet lead remains constant, whereas for too large values of v_{inhom} it will decrease[2].
In the following, the influence of the step speed v_{inhom} and the initial lead $s_0 = s(t = 0)$ on the droplet's ability to keep up with the wettability profile will be investigated. For this, the inhomogeneity profile given by eq. (3.5) is being employed, and the position of the initial step c as well as the speed of the inhomogeneity v_{inhom} is being varied. From this, for each parameter set, it is determined whether or not the droplet lead $s(t)$ has increased or decreased over the course of the simulation. Note that in order to exclude the effects of boundary conditions, the integration time was restricted to $T = 0.95L/(2v_{\text{inhom}})$ since for the limiting case of a droplet not being moved by the wettability pattern at all, the droplet lead will be equal to s_0 once the profile has moved a distance of $L/2$, i. e., $s(t = L/(2v_{\text{inhom}})) = s_0$. Using the factor 0.95 results in a decrease of the droplet lead $s(t = 0.95L/(2v_{\text{inhom}})) < s_0$ between the initial and final states and, therefore, circumvents the problems arising from the wettability profile obeying the applied periodic boundary conditions.
The obtained results are displayed in fig. 3.5. The green colour indicates an increasing droplet lead, where the data points, i. e., the simulated parameter values, are indicated by upwards pointing trian-

2 Due to the periodic boundary conditions employed the distance can only increase for $L/(2v_{\text{inhom}})$ since the minimum distance is $L/2$.

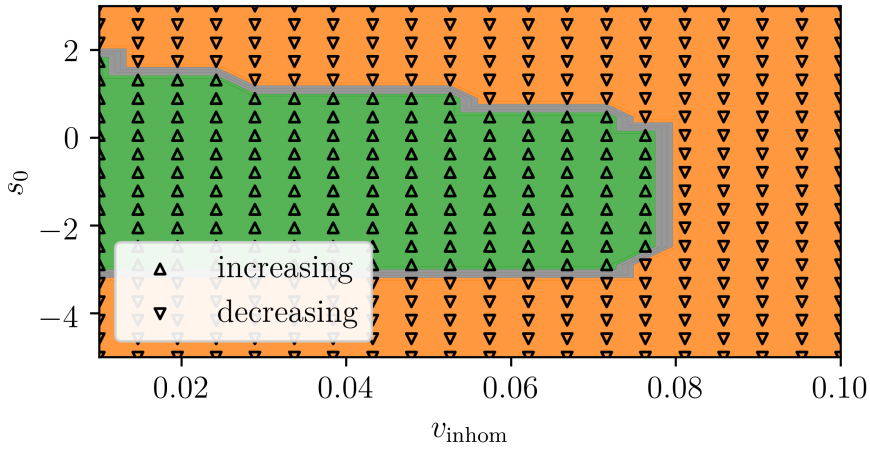

Figure 3.5: Behavior of the droplet lead s given by eq. (3.12) for different initial droplet leads s_0 and step speeds v_{inhom}. The direction of the triangles and the background colour indicate whether the droplet lead is increasing (upwards pointing triangles and green background colour) or decreasing (downwards pointing triangles and orange background colour) over time.

gles. A decrease of the droplet lead is marked by orange background colour and downwards pointing triangles. Starting at an arbitrary point, the droplet lead $s(t)$ over time follows the direction the triangles indicate. Therefore, points at which two triangle heads meet constitute a point of stable droplet lead, analogous to the droplet displayed for $v_{\text{inhom}} = 0.02$ in fig. 3.4. Here the initial droplet lead s_0 is equal to the droplets equilibrium distance to the wettability profile. Points at which the rear of two arrows meet correspond to unstable states of constant droplet lead, where arbitrary small distortions lead either to an increase of droplet lead until again a stable state is obtained or a decrease of droplet lead leading to the droplet crossing the wettability gradient. For the five largest inhomogeneity velocities, no stable states were obtained. In this parameter region the wettability profile, therefore, is too fast for the droplet to keep up independent of the initial lead.
While the general behaviour will remain the same for different parameters of the wettability profile, the exact form of fig. 3.5 will not be replicated. The following section will perform a thorough investigation of the influence of the various wettability profile parameters on the exhibited droplet dynamics.

3.4 MAXIMUM DROPLET VELOCITY

As previously discussed, the parameters of the employed wettability profile significantly impact the dynamics exhibited by the liquid. In order to understand the influence of these parameters on the droplet dynamics, the speed of the liquid v_{drop} will be investigated for differ-

ent wettability parameters.
The parameter with the most significant impact on the droplet velocity is the speed of the inhomogeneity v_{inhom}. In section 3.3 it was shown that a droplet exposed to a moving wettability pattern will either assume an equilibrium distance to the step profile, i. e., move at the constant velocity $v_{\text{drop}} = v_{\text{inhom}}$ or it will cross the wettability gradient and cease to move since it is no longer exposed to a wettability gradient. To characterise this behaviour, it is useful to introduce the average droplet velocity $\bar{v}_{\text{drop}}$ given by

$$\bar{v}_{\text{drop}} = \frac{x_{\max}(t = T_{\text{int}}) - x_0}{T_{\text{int}}}, \tag{3.13}$$

where $x_{\max}(t)$ is the position of the point of maximum height while T_{int} is equal to the time at the end of the integration. During infinite time simulations, the average droplet velocity $\bar{v}_{\text{drop}}$ would either be equal to the inhomogeneity speed v_{inhom}, if the droplet assumes its equilibrium position relative to the pattern or equal to zero if the droplet is not able to keep up with the profile.
The average droplet velocity was determined for simulations of liquid droplets with an initial height $h_0 = 1$ using a moving wettability pattern given by eq. (3.5) with different step speeds. A domain size of $L = 210$ was used such that a large integration time could be chosen without the liquid droplet experiencing the profile multiple times due to the employed periodic boundary conditions[3]. The remaining parameters are given in the caption of fig. 3.6. For each employed parameter set, the average droplet speed was calculated using eq. (3.13). Note that the periodic boundary condition have to be considered during the calculation of the nominator in eq. (3.13). The obtained results are displayed in fig. 3.6. The previously discussed dynamics can be observed in this display. For increasing inhomogeneity velocities v_{inhom} the average droplet velocity $\bar{v}_{\text{drop}}$ increases linearly, corresponding to the droplet being able to keep up with the profile with $\bar{v}_{\text{drop}} = v_{\text{inhom}}$. As a threshold value of $v_{\text{inhom}}^{\text{th}} \approx 0.047$ is reached, the maximum average droplet velocity $\bar{v}_{\text{drop}}^{\max}$ is obtained, after which $\bar{v}_{\text{drop}}$ suddenly decreases. For even larger v_{inhom} the average droplet velocity is reduced further to $\bar{v}_{\text{drop}} \approx 0$. The region where $\bar{v}_{\text{drop}} \neq v_{\text{inhom}}$ corresponds to the droplet being left behind by the wettability pattern and ceasing to move. The deviations from $\bar{v}_{\text{drop}} = 0$ are a result of the finite simulation times since at the beginning of the simulation, the droplet is moved by the wettability step regardless of the inhomogeneity speed. Therefore the speed at the beginning deviates from zero, such that for v_{inhom} larger than the threshold value, the average droplet speed will not be equal to zero if one considers all time steps of the simulation.

3 Since the used profile is periodic, after an integration time $T = \frac{L}{v_{\text{inhom}}}$ the profile will again be at its initial position. Thus, a left-behind droplet will experience the inhomogeneity profile again, which leads to distortions of the measured average droplet speed.

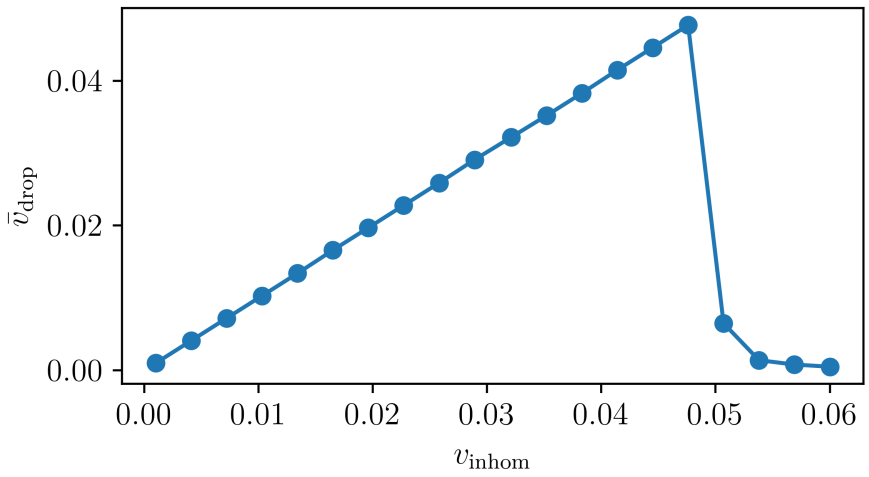

Figure 3.6: Average droplet speed $\bar{v}_{\mathrm{drop}}$ shown for different inhomogeneity speeds v_{inhom} for a moving ridge inhomogeneity given by eq. (3.5). The parameters are $h_0 = 1$, $\rho_{\mathrm{HW}} = -0.8$, $\rho_{\mathrm{LW}} = 0.5$, $x_A = 3$, $ls = 0.15$ $L = 210$.

To reduce this effect the initial 90% of of the performed time-steps for each simulation were discarded for fig. 3.6.
In the following the influence of the other parameters contained in the wettability pattern (3.5) on the maximum possible droplet velocity $\bar{v}^{\mathrm{max}}_{\mathrm{drop}}$, i. e., the velocity corresponding to the critical inhomogeneity speed $v^{\mathrm{th}}_{\mathrm{inhom}}$, will be investigated.

3.4.0.1 *The Influence of ρ_{HW}*

Since the observed droplet movement is a results of the wettability gradient it is experiencing, its strength has a major influence on the dynamics of the droplets. If the strength of the wettability gradient results in $\bar{v}_{\mathrm{drop}} < v_{\mathrm{inhom}}$, the droplet will lag behind the profile and is left behind. The strength of the wettability gradient is mainly determined by the employed wettability contrast C_ρ given by eq. (3.2). Both parameters ρ_{HW} and ρ_{LW} determining the contrast can be varied independently during the simulations. Within this section, the influence of the parameter determining the wettability of the highly wettable patch ρ_{HW} is being investigated while the region of low wettability remains at a constant value with $\rho_{\mathrm{LW}} = 1.0$.
In order to determine the maximum possible droplet velocity for each value of ρ_{HW} simulations, analogous to the one used for fig. 3.6 need to be performed. The results of these simulations are shown in fig. 3.7, where the average droplet velocity $\bar{v}_{\mathrm{drop}}$ is displayed against the speed of the inhomogeneity v_{inhom} for three values of ρ_{HW}. For each value of ρ_{HW} the presented curve corresponds to the curve displayed in fig. 3.6 with a shifted threshold value. As it can be seen in fig. 3.7, choosing smaller values for ρ_{HW}, i. e., increasing the contrast C_ρ, which

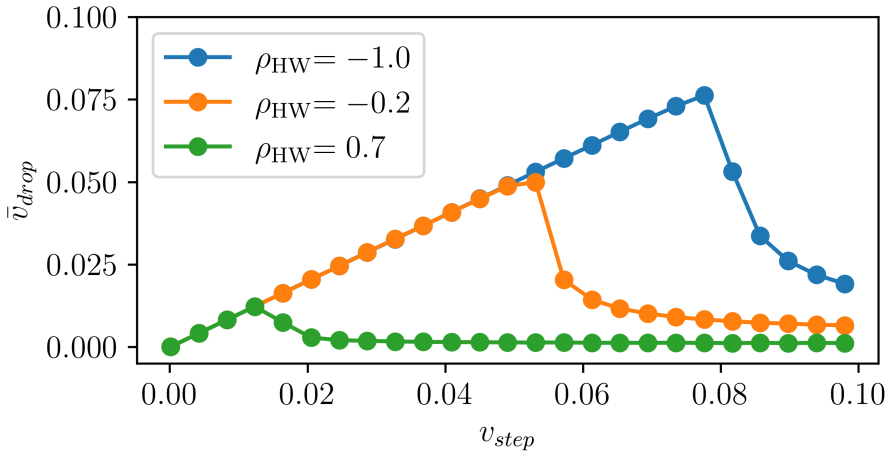

Figure 3.7: Average droplet speed v_{drop} plotted against the used inhomogeneity speeds v_{inhom} for different ρ_{HW} values of a moving ridge inhomogeneity given by eq. (3.5). The remaining parameters are $\rho_{\text{LW}} = 1$, $x_A = 3$, $ls = 1$, $L = 80$, $h_0 = 1$.

corresponds to a steeper wettability gradient at the boundary of the wettability well, results in an increase of $\bar{v}_{\text{drop}}^{\text{max}}$. Note that, compared to fig. 3.6, the finite size effects have an increased impact on the average droplet speed $\bar{v}_{\text{drop}}$ for step speeds beyond the critical value. This is due to the decreased domain size of $L = 80$ for fig. 3.7 compared to $L = 210$ for fig. 3.6 and, thus, the decreased integration times.
For each of these curves, the maximum average droplet velocity can be determined. Note that the step size when varying v_{step} has been chosen smaller than displayed in fig. 3.7, where only twenty data points were used, compared to a total of fifty recorded points for each value of ρ_{HW}. All of the recorded data points were used to determine the maximum droplet velocity. The obtained results are displayed in fig. 3.8. Here, a non-linear decrease of the maximum droplet velocity for increasing ρ_{HW} values can be observed. A data point for $\rho_{\text{HW}} = 1$ is not included as here the maximum droplet velocity will be equal to $\bar{v}_{\text{drop}}^{\text{max}} = 0$ since $\rho_{\text{HW}} = \rho_{\text{LW}}$ corresponds to a homogeneous substrate, i. e., no wettability gradient and, thus, no droplet movement.
Using the Cox-Voinov law, one can obtain an expression for the maximum average droplet velocity [18]

$$\bar{v}_{\text{drop}}^{\text{max}} = a \left[\left(\theta_{\text{eq}}^{\text{max}} \right)^3 - \left(\theta_{\text{eq}}^{\text{min}} \right)^3 \right]. \tag{3.14}$$

Here $\theta_{\text{eq}}^{\text{max}}$ is the maximum equilibrium contact angle of a droplet, i. e., the contact angle of a droplet placed on a homogeneous substrate with the wettability $\omega(x,t) = \rho_{\text{LW}}$. Analogously $\theta_{\text{eq}}^{\text{min}}$ corresponds to the contact angle of a droplet on a substrate with the wettability $\omega(x,t) = \rho_{\text{HW}}$. a is a proportionality constant, defined by the physical properties of the used materials and includes a finite slip length. Note that the model employed here *does not* include a finite slip length but

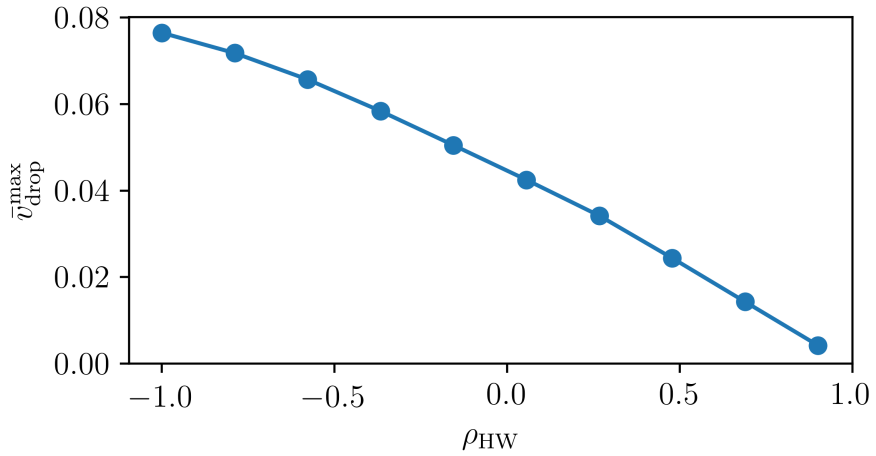

Figure 3.8: Maximum average droplet speed $\bar{v}_{\text{drop}}$ plotted for different ρ_{HW} values of a moving ridge inhomogeneity given by eq. (3.5). The remaining parameters are $\rho_{\text{LW}} = 1$, $x_A = 3$, $ls = 1$, $L = 80$, $h_0 = 1$.

rather applies no-slip boundary conditions at the liquid-solid interface (cf. sec. 2.1), the parameter a can therefore not be calculated. However, the proportionality of $v_{\text{drop}}^{\text{max}}$ to $\left(\theta_{\text{eq}}^{\text{max}}\right)^3 - \left(\theta_{\text{eq}}^{\text{min}}\right)^3$ can be verified by a fit in the form of eq. (3.14) using a as the fit parameter.
From the employed wettability values the corresponding equilibrium contact angles can be calculated with eq. (A.11), such that the x-axis of fig. 3.8 can be transformed to the contact angle contrast $\Delta\Theta = \theta_{\text{eq}}^{\text{max}} - \theta_{\text{eq}}^{\text{min}}$. This was done for fig. 3.9, where the maximum average droplet velocities are displayed against the contact angle contrast. The data points were fitted with eq. (3.14) which resulted in $a = (3.07 \pm 0.03) \cdot 10^{-7}$. The parameter a is proportional to $-\frac{1}{\ln(\lambda)}$, where λ is the slip length [18]. Since the employed model does not include a finite slip length, but rather no-slip boundary conditions, one would expect the parameter to be small since $\lim_{\lambda \to 0} \frac{-1}{\ln(\lambda)} = 0$. The actual value of a supports this estimation. Note that the data points deviate from the applied fit for large inclination angle contrasts, i. e., $\Delta\Theta \approx 60°$. This data point corresponds to $\rho_{\text{HW}} = -1$ and, therefore, to the complete wetting case. The deviations between the data and the fit could be caused by the transition from a partially wetting case ($\Delta\Theta < 60°$) to the complete wetting case.
Even though the employed model does not include a finite slip length, the proportionality given by eq. (3.14) still holds. Thus, using the determined value of a, one is able to estimate the maximum possible droplet velocity from the ρ_{HW} and ρ_{LW} values of the wettability profile. Figure 3.9 also shows that the maximum droplet velocity remains roughly constant for large wettability contrasts, i. e., contact angle contrasts $\Delta\theta > 40°$. The gain obtained from increasing the wettability contrast beyond this value is rather small, such that for most applica-

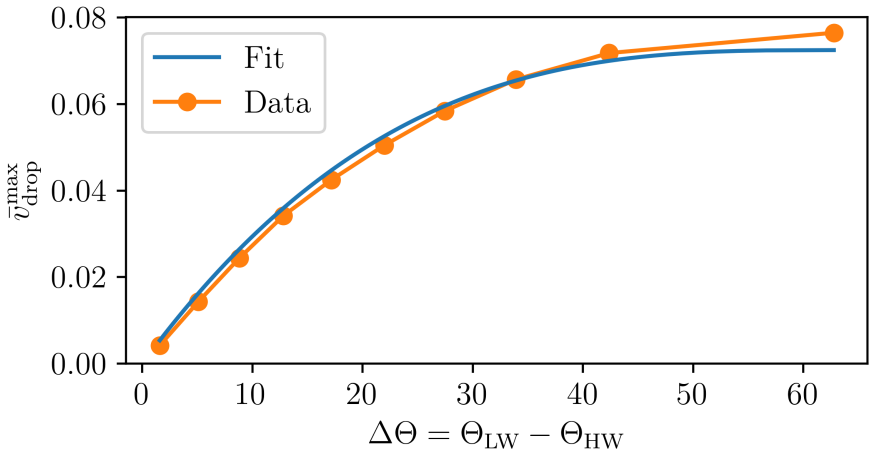

Figure 3.9: Maximum average droplet velocity $v_{\text{drop}}^{\text{max}}$ for different contact angle contrasts $\Delta\Theta$ extracted from fig. 3.7. Here $\rho_{\text{LW}} = 1$ was employed and ρ_{HW} varied. The data points were fitted with eq. (3.14) using a as the fitting parameter. The fit converged with $a = (3.07 \pm 0.03) \cdot 10^{-7}$.

tions, a relatively small contrast would suffice.
Analogously the influence of ρ_{LW} instead of ρ_{HW} can be investigated. Corresponding results can be found in fig. 3.10. The resulting value for a in this case is $a = (3.23 \pm 0.02) \cdot 10^{-7}$. While this value does not exactly match the value obtained by varying ρ_{HW}, it still lies in the same order of magnitude. However, the discrepancy of the obtained values for a should be considered when using it to approximate the maximum droplet velocity.

3.4.1 *Influence of ls*

Another parameter that influences the wettability gradient strength and, thus, the possible droplet speed is ls. Since it is equal to ± 1 times the inverse of the steepness at the point $x = c \pm x_A$ (c.f. section 3.1), an increased value of ls corresponds to a decrease of the gradient strength.
In fig. 3.11 the maximum average droplet velocity $\bar{v}_{\text{drop}}^{\text{max}}$ is displayed for different values of the parameter ls. Again, these results were obtained by performing simulations, analogous to the one used for fig. 3.6, for each value of ls. Additionally, the wettability profiles for the smallest and largest employed value of ls are displayed, to illustrate the influence of ls on the shape of the profile. It can be observed in fig. 3.11 that $\bar{v}_{\text{drop}}^{\text{max}}$ decreases for increasing values of ls as to be expected by a decrease of the gradient strength. While the maximum average droplet speed undergoes only small changes for low values of ls ($ls \leq 0.75$), it decreases significantly for larger ls values. The steepness of the wettability, therefore, only has a minor impact on the

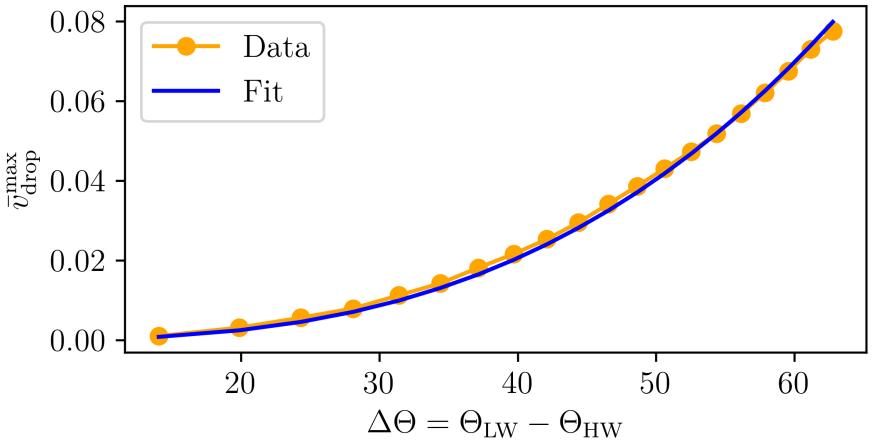

Figure 3.10: Maximum average droplet velocity $v_{\mathrm{drop}}^{\mathrm{max}}$ displayed for different contact angle contrasts $\Delta\Theta$. The maximum average droplet velocity was determined from simulations analogous to fig. 3.6 where the value of ρ_{LW} was varied and ρ_{HW} was kept constant at $\rho_{\mathrm{HW}} = -1.0$. All remaining parameters are the same as for fig. 3.9. The data points were fitted with eq. (3.14) using a as the fitting parameter. The fit converged with $a = (3.23 \pm 0.02) \cdot 10^{-7}$.

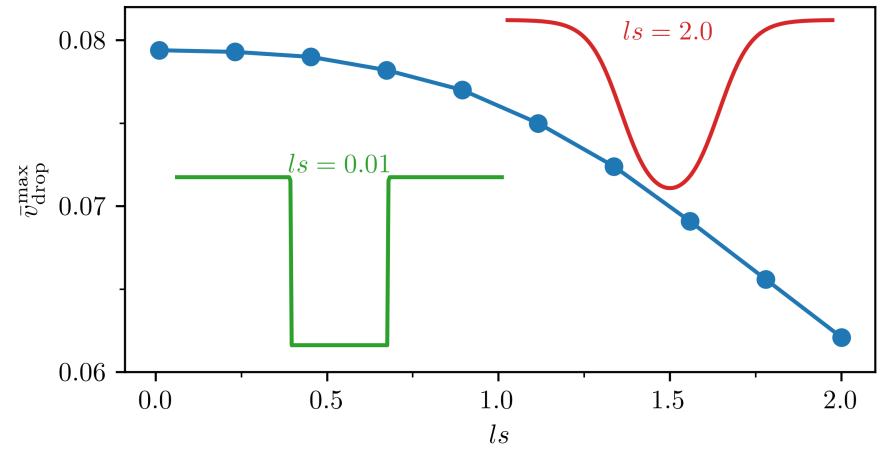

Figure 3.11: Maximum average droplet velocity $\bar{v}_{\mathrm{drop}}^{\mathrm{max}}$ for different values of the inhomogeneity profile parameter ls, while ls was varied for each data point, the other parameters remained constant at $\rho_{\mathrm{HW}} = -1.0$, $\rho_{\mathrm{LW}} = 1.0$, $x_A = 3.0$ and $L = 80$. Additionally, the wettability profiles corresponding to $ls = 0.01$ and $ls = 2.0$ are displayed to illustrate the influence of the parameter ls.

obtainable droplet speed, if it is chosen sufficiently small. Additionally, the impact of ls on the maximum average droplet speed is less significant than the impact of the wettability contrast (c.f. section 3.4.0.1), for the considered parameter regions. For experiments that aim to obtain a high droplet speed, the focus should, thus, lie on creating a strong wettability contrast rather than a steep transition between the wettability values.

3.4.2 *Influence of h_0*

Another parameter influencing the possible droplet speed, which, in contrast to the ones considered previously, is not a parameter of the inhomogeneity profile, is the initial droplet height h_0. The used initial condition given by eq. (3.10) is entirely determined by the chosen value of h_0 since the value of $\theta_0 \approx 0.779$ is kept constant (c.f. sec. 3.2). Thus, the volume of the droplet is defined by the initial height. A dependence of the droplet's velocity on h_0, therefore, corresponds to a dependence on the volume of the liquid. In fig. 3.12 the maximum average droplet velocity is displayed for various initial droplet heights h_0. The graph shows that the obtainable speed increases for decreasing initial droplet heights. This corresponds to the expected behaviour since for an increasing film height, the absolute value of the disjoining pressure decreases, leading to a decreased impact of the wettability profile on the exhibited liquid dynamics. The behaviour of the disjoining pressure for different film heights can be extracted from the displayed wetting potential in fig. 2.2 and the relation between the disjoining pressure and the wetting potential given by eq. (2.8). Since for $h > h_p$ the steepness of the wetting potential $\partial_h f(h, x, t)$ is positive but decreases for increasing film heights (c.f. fig. 2.2), $\Pi(h, x, t)$ also decreases, leading to a less significant impact of the disjoining pressure and, thus, the wettability profile, on the exhibited dynamics.

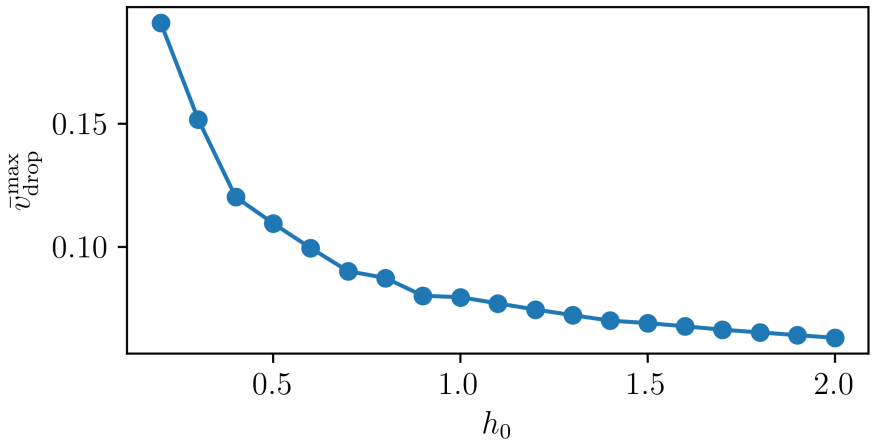

Figure 3.12: Maximum average droplet velocity $\bar{v}_{\text{drop}}^{\text{max}}$ for various initial droplet height h_0. While the other parameters are equal to the ones used in fig. 3.6.

4

2D HORIZONTAL SUBSTRATE

This chapter considers a two-dimensional horizontal substrate, such that $\mathbf{x}$ in eq. (2.1) corresponds to a two dimensional vector $\mathbf{x} = (x, y)^T$. The size of the domain in x- and y-direction is given by L_x and L_y, respectively. The domain is defined such that its center lies at $x = y = 0$, i. e., $x \in [-L_x/2, L_x/2]$, $y \in [-L_y/2, L_y/2]$.
For the boundaries of the two-dimensional domain at $x = \pm L_x$ and $y = \pm L_y/2$ periodic boundary conditions (PBC) will be employed. Other possible choices are Neumann (no-flux) boundary conditions, as well as a combination of both. Due to the employed PBCs, the domain corresponds to an infinitely extended substrate, i. e., a periodical extension of the simulated domain in both directions. These boundary conditions are, therefore, especially valuable if one aims to investigate periodic patterns as it was done experimentally in [53].

4.1 MOVING WETTABILITY PROFILE

The two-dimensional extension of the previously (c.f. chapter 3) employed wettability profile given by eq. (3.5) will be used in the following. Using eq. (3.5) for the two-dimensional substrate results in a highly wettable stripe with $\omega(\mathbf{x}, t) = \rho_{\mathrm{HW}}$, surrounded by a region of low wettability, where $\omega(\mathbf{x}, t) = \rho_{\mathrm{LW}}$. As eq. (3.5) only depends on the x-coordinate, the profile is translation invariant along the y-axis. A cross-section of the wettability profile along the x-direction, therefore, corresponds to the one-dimensional profile displayed in fig. 3.1.
If an analogous direct extension of the initial condition given by eq. (3.10) is performed, a two-dimensional liquid ridge is obtained, which, analogous to the striped wettability pattern is translational invariant in the y-direction.
To approximate a two-dimensional droplet as the initial condition, a paraboloid shape given by

$$h(x, y, t = 0) = -\frac{1}{4h_0} \tan^2(\theta_0) \cdot \left[(x - x_0)^2 + (y - y_0)^2\right] + h_0, \quad (4.1)$$

is being employed. Compared to eq. (3.10) the term $(x - x_0)^2$ is replaced by $\left[(x - x_0)^2 + (y - y_0)^2\right]$, where x_0 and y_0 correspond to the position of maximum height in the x- and y-direction, respectively. All other parameters have the same meaning as in eq. (3.10). Thus, a cross-section through the centre of the droplet, i. e., through $x = x_0$ and $y = y_0$ has the same form as a one-dimensional droplet. An illustration

of the employed initial droplet with $h_0 = 1$, $x_0 = 0$, $y_0 = 0$, $\theta_0 = 0.779$ on a substrate with $L_x = 16$ and $L_y = 6$ is displayed in fig. 4.1. Additionally, cross-sections along $x = 0$ and $y = 0$ are displayed to demonstrate the relation to the one-dimensional droplet.
Since the attempt of this section is to extend the one-dimensional results obtained in chapter 3 to the two-dimensional case, the height of the initial droplet is chosen such that its volume is equal to the volume of a two-dimensional ridge[1] with $h_0 = 1$. The volume of a paraboloid can be calculated by exploiting its rotational symmetry. The paraboloid described by eq. (4.1) can be obtained by a rotation of

$$x(h) = a\sqrt{h}, \tag{4.2}$$

around the h-axis. A positive a is employed here to simplify the calculation. The described parabola, therefore, corresponds to an inverted initial droplet. The value of $x(h = 0)$ corresponds to 0 while $x(h = h_0)$ is equal to the position of the contact line along the x-direction (c.f. eq. (3.8)). Using the values obtained for the contact line in chapter 3, the parameter a can be computed

$$x(h = h_0) = \sqrt{\frac{4h_0^2}{\tan^2\theta_0}} = a\sqrt{h_0} \Rightarrow a = \frac{2\sqrt{h_0}}{\tan\theta_0}. \tag{4.3}$$

The volume of the paraboloid, thus, can be determined using the disk method

$$V_{2DD} = \pi \int_0^{h_0} x(h)^2 dh = \frac{4\pi h_0}{\tan^2\theta_0}\left[\frac{h^2}{2}\right]_0^{h_0} = \frac{2\pi h_0^3}{\tan^2\theta_0}. \tag{4.4}$$

The volume of the initial one-dimensional droplet can be calculated by integrating the initial condition, given in eq. (3.10), from the left to the right contact point (c.f. eq. (3.8))

$$V_{1DD} = \int_{-\sqrt{h_0/a}}^{\sqrt{h_0/a}} -ax^2 + h_0 dx = \frac{8}{3\tan\theta_0} h_0^2. \tag{4.5}$$

The volume of the two dimensional ridge, therefore, is equal to $V_{2DR} = L_y V_{1DD}$. Using both the volume of the two-dimensional droplet and the ridge volume, one can compute the appropriate initial height h_0 for the droplet such that both volumes are equal.
Placing these different initial conditions on a moving wettability pattern, one can determine the maximum average droplet velocity from the displacement of the maximum film height analogous to the investigations in chapter 3. Varying the inhomogeneity's speed while measuring the droplet's speed leads to the results displayed in fig. 4.2. Here the average droplet velocity for both applied initial conditions and the droplet velocity for a one-dimensional droplet using the

1 The two-dimensional ridge corresponds to the direct extension of the one-dimensional droplet.

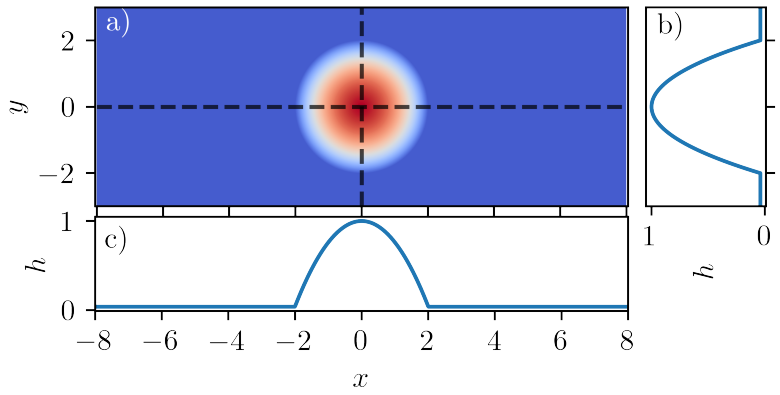

Figure 4.1: a) Height profile of the initial two-dimensional droplet given by eq. (4.1) with $h_0 = 1$ and $\theta_0 = 0.779$, on a substrate of the size $L_x \times L_y = 16 \times 6$. Dotted horizontal and vertical lines indicate the axes along which the cross-section portrayed in c) and b) were determined. Both cross sections are equivalent to the initial one-dimensional droplet given by eq. (3.10) using the same parameters as for the two-dimensional droplet.

same wettability parameters and the same value of h_0 as for the two-dimensional ridge are portrayed. The behaviour observable for the two-dimensional simulations is analogous to the one-dimensional case. After a certain threshold value of v_{inhom} is reached, the liquid can no longer follow the inhomogeneity profile, leading to a steep decrease of the average droplet velocity $\bar{v}_{\text{drop}}$. For infinitely long simulations, the droplet velocity decreases to zero for v_{inhom} larger than the threshold velocity. Since finite simulation times were considered here, the average droplet velocity assumes non-vanishing values, which decline for increasing inhomogeneity speeds. These effects again correspond to finite-size effects (c.f. chapter 3). Compared to the one-dimensional consideration, these finite-size effects are more pronounced here. This is due to the simulations being performed on smaller domains to reduce the computation time.

While the behaviour of the different initial conditions is phenomenological the same, the threshold value differs for the two-dimensional liquid structures. The results obtained for the two-dimensional ridge match well with the results of the one-dimensional droplet. Here both threshold values agree with each other, thus, the maximum obtainable droplet (or rather ridge) speed matches the one-dimensional case. Equation (3.14) should, therefore, also be applicable for estimating the maximum liquid velocity for two-dimensional ridges. The matching between the one-dimensional droplet and the two-dimensional ridge should be investigated with a higher accuracy before employing eq. (3.14) as a estimation, since the resolution in fig. 4.2 is relatively low.

The results obtained for the two-dimensional droplet, on the other

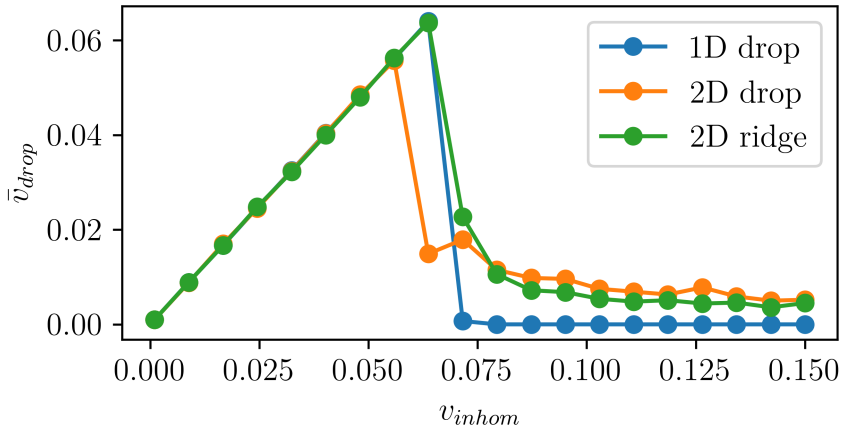

Figure 4.2: Average velocity of a one- and two-dimensional droplet as well as of a two-dimensional ridge plotted for different inhomogeneity speeds. The volume of the two-dimensional droplet is chosen equal to the volume of the two-dimensional ridge. The height of the two-dimensional ridge is the same as for the one-dimensional droplet $h_0 = 1$, such that the results can be compared to the one-dimensional case. The employed wettability profile parameters are $ls = 0.15$, $x_A = 3$, $c = -20$ $\rho_{\mathrm{HW}} = -0.8$, $\rho_{\mathrm{LW}} = 0.5$.

hand, do not match those obtained for the one-dimensional droplet. This discrepancy can be attributed to the additional curvature of the droplet's contact line compared to the contact line of the liquid ridge, which corresponds to a straight line. Due to the increased curvature, the Laplace pressure in eq. (2.4) has an increased impact on the exhibited dynamics. Thus, the droplet can cross the wettability gradient for smaller v_{inhom} leading to a decrease of the maximum average droplet velocity (c.f. section 3.4).

4.2 PLATEAU-RAYLEIGH INSTABILITY

This section will investigate the Plateau-Rayleigh instability exhibited by a liquid ridge on a horizontal substrate. This phenomenon occurs for elongated liquid structures, e. g. ridges and liquid streams, and results in a break-up of the structure into several smaller structures. Here, liquid ridges placed on a wettability stripe pattern will be considered. These structures will exhibit a transversal instability and naturally break up into several smaller droplets.

4.2.1 *Undisturbed Plateau-Rayleigh Instability*

Before considering controlling mechanisms for the liquid dynamics during the Plateau-Rayleigh instability, first, the evolution of a homogeneous liquid film with the initial height profile $h(\mathbf{x}, t = 0) = h_{\mathrm{hom}}$ placed on a prestructured substrate without temporal switching will

be discussed here. The parameters employed during the simulations within this section are chosen to ensure the occurrence of a Plateau-Rayleigh instability (c.f. [20]).
A simulation was performed on a two-dimensional substrate with the size $L_x \times L_y = 4 \times 12$, where periodic boundary conditions are employed in both directions. The employed wettability profile is again given by eq. (3.1) with $ls = 0.06$, $x_A = 0.4$, $c = 0$, $\rho_{\mathrm{HW}} = -0.5$ and $\rho_{\mathrm{LW}} = 0.5$. The initial height of the homogeneous film was set to $h_{\mathrm{hom}} = 0.076$. Snapshots obtained during This direct numerical simulation are displayed in fig. 4.3. Here, the points of maximum steepness, i. e., $x = c \pm x_A$ are marked by dashed black lines. After the initial homogeneous film, shown in fig. 4.3 a), is placed on the substrate, the liquid starts to retract from the regions with lower wettability. During this relaxation process, the liquid exhibits various structures until a ridge forms on the more wettable stripe forms which is displayed in fig. 4.3 b). The ridge state remains present for some time until it exhibits a transversal instability and breaks up into two bulges, displayed in fig. 4.3 c). Both bulges are located along $x = 0$, with one at the boundary $y = L_y/2$ while the other one forms at $y = 0$. The two bulges state remains present for a longer time than the ridge state until it starts to deform. The bulge at the centre of the domain gradually absorbs the mass of the outer bulge such that in the end, the one bulge state shown in fig. 4.3 d) prevails.
The system's free energy given by eq. (2.7) was measured during the simulation. In the following, a shifted version of the free energy will be considered

$$\tilde{F} = F - F_{\mathrm{hom}}. \tag{4.6}$$

Here F is the system's free energy determined by eq. (2.7) while F_{hom} is the free energy of a homogeneous film with the same volume on an equivalent substrate as the considered state. The shifted free energy $\tilde{F}$ of a homogeneous film is, therefore, equal to zero. If not explicitly mentioned, F, as well as references to the free energy, will be used to denote the shifted free energy given by eq. (4.6) instead of the free energy given by eq. (2.7).
The free energy during the relaxation of the homogeneous film is shown in fig. 4.4. Here the free energies of the plateau states, i. e., the meta-stable ridge and two droplet states, as well as the globally stable one droplet state, are indicated by colour-coding. The corresponding handles in the legend refer to the states displayed in fig. 4.3 b), c) and d). The meta-stable states are present for relatively long times with only minor changes to the liquid profile, i. e., the free energy remains roughly constant for some time which corresponds to a plateau in fig. 4.4.
The time scales t_{stable} for which the states are present and their respective free energies are given in table 4.1. To determine t_{stable} the

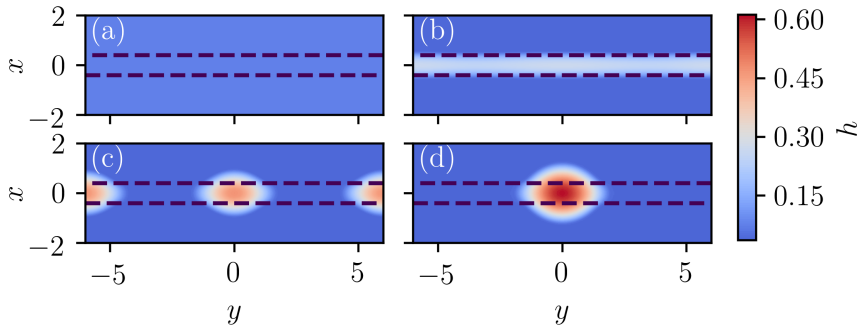

Figure 4.3: Snapshots obtained during the relaxation of a homogeneous film with $h_{\text{hom}} = 0.076$ on a heterogeneous substrate of the size $L_x \times L_y = 4 \times 12$ with a wettability pattern given by eq. (3.1) using the parameters $ls = 0.06$, $x_A = 0.4$, $c = 0$, $\rho_{\text{HW}} = -0.5$, $\rho_{\text{LW}} = 0.5$. The points of steepest slope are indicated by dotted black lines. a) displays the initial homogeneous film which relaxes into the liquid ridge displayed in b). The ridge undergoes a Plateau-Rayleigh instability resulting in the formation of two bulges shown in c). The bulges evolve into a single bulge displayed in d).

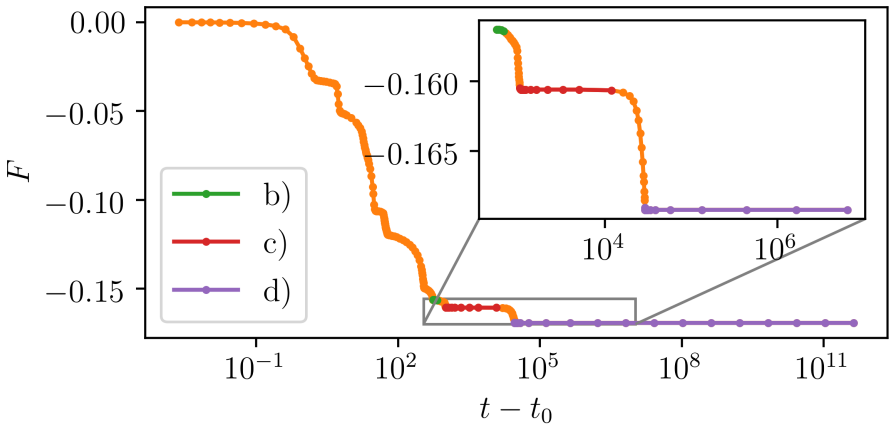

Figure 4.4: Free energy during the relaxation of the homogeneous film on a wettability stripe pattern. The parameters are the same as the ones given in the caption of fig. 4.3. The handles in the legend correspond to the states displayed in fig. 4.3. The inset shows a close-up of the relaxation process starting from the ridge (green) to the one bulge state (purple).

Table 4.1: Free energies and times for which the meta-stable states and the globally stable state (c.f. fig. 4.3 b) c) and d)) were present, determined using the free energy displayed in fig. 4.4.

State	F	t_{stable}
ridge	-0.1563	$1.1 \cdot 10^2$
two bulge	-0.1605	$1.1 \cdot 10^4$
one bulge	-0.1607	∞

initial and final states need to be determined. For this, a series of at least five consecutive states was determined for which the free energy of all states varies by less than 0.01% with respect to the free energy of the first state. The stability time t_{stable} can then be calculated as the time difference between the first and final state within the series. The free energy of the first state in the series is associated with the corresponding meta-stable state. Table 4.1 shows that the times the states remain stable vary significantly, with the two bulge state being stable for two orders of magnitude longer.

One can observe distinct liquid dynamics using different heights of the initially employed homogeneous film. In addition to the previously considered $h_{\text{hom}} = 0.076$ also $h_{\text{hom}} = 0.0464$ was simulated. The parameters of the wettability profile are the same as those used for fig. 4.3. The domain size, however, was changed to $L_x \times L_y = 2 \times 4$. Snapshots obtained during the direct numerical simulation are displayed in fig. 4.5. Analogous to fig. 4.3 the homogeneous film relaxes and forms a liquid ridge on the highly wettable stripe shown in b). This ridge exhibits a Plateau-Rayleigh instability and breaks up into three droplets as shown in fig. 4.5 c). After this the droplet at the boundary is absorbed by the other two droplets resulting in the globally stable two droplet state shown in fig. 4.5 d). The difference to $h_{\text{hom}} = 0.076$, therefore, lies in the states formed during the Plateau-Rayleigh instability as well as in the globally stable state.

The system's free energy during the relaxation process is portrayed in fig. 4.6. Here again, the plateau states are marked and labelled according to the panels in fig. 4.5. Note that compared to fig. 4.4 the absolute value of the free energy is one order of magnitude smaller due to the decreased liquid film height. The free energy of the meta-stable states and the times they were present during the simulation are given in table 4.2. The values were determined employing the same method as before. Comparing the stability times to table 4.1 one can see that these are as well one order of magnitude smaller than those obtained for $h_{\text{hom}} = 0.076$.

As a third initial film height $h_{\text{hom}} = 0.112$ was considered on a domain of size $L_x \times L_y = 2 \times 12$ with the same wettability parameters as before. The relevant states observed during the simulation are shown in fig. 4.7, where the homogeneous film is not displayed. As before,

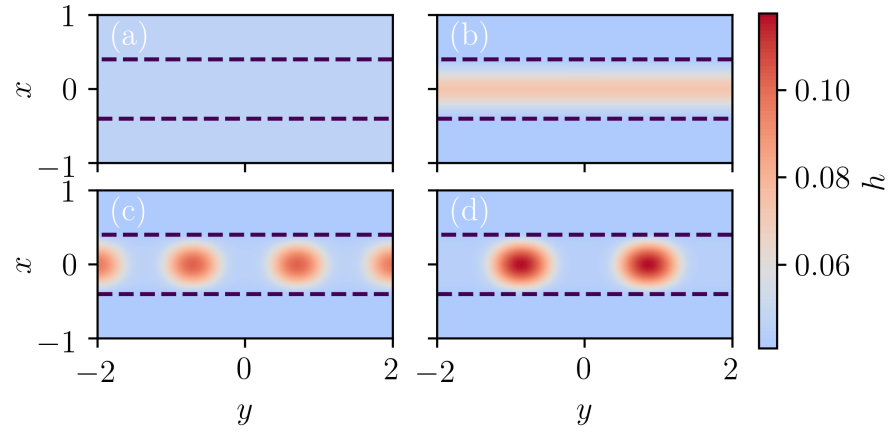

Figure 4.5: States obtained during the relaxation of a homogeneous liquid film of height $h_{\text{hom}} = 0.0464$ on a wettability stripe pattern with parameters equal to the ones given in the caption of fig. 4.3 except for the simulated domain size which here is equal to $L_x \times L_y = 2 \times 4$. The points of steepest slope are indicated by dotted black lines. a) corresponds to the initial homogeneous film while b) displays a ridge state. The ridge undergoes a Plateau-Rayleigh instability, first forming a three droplet c) and then a two droplet state d), where the first is meta- and the latter globally stable.

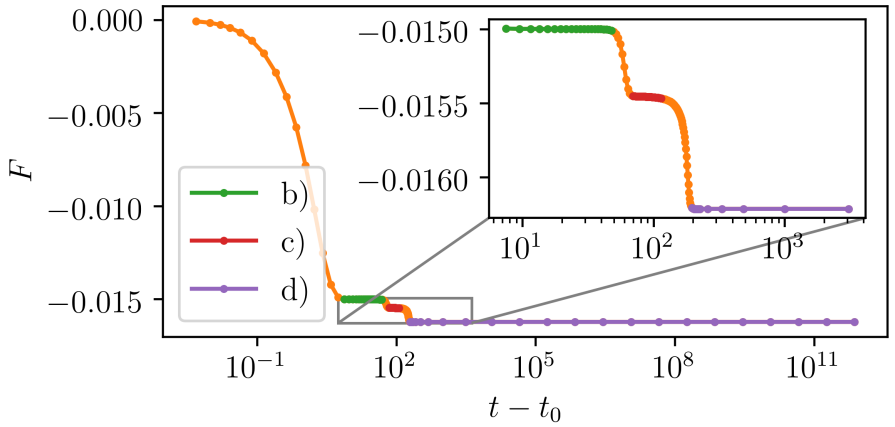

Figure 4.6: Free energy during the relaxation of the homogeneous film on a wettability stripe pattern. The parameters are given in the caption of fig. 4.5. The handles in the legend correspond to the states displayed in fig. 4.5. The inset shows a close-up of the relaxation process starting from the ridge (green) to the two droplets state (purple).

Table 4.2: Free energies and times for which the state was present during the simulation corresponding to fig. 4.6.

State	F	t_{stable}
ridge	−0.0158	40
three droplets	−0.0163	44
two droplets	−0.0171	∞

Table 4.3: Free energies and times for which the state was present during the simulation corresponding to fig. 4.8.

State	F	t_{stable}
ridge	-0.1215	$4.1 \cdot 10^2$
two bulges	-0.1299	$5.8 \cdot 10^3$
bulge and bridge	-0.1378	19
bridge	-0.1761	∞

the liquid starts forming a ridge on the more wettable stripe, shown in fig. 4.7 a). This ridge exhibits a transversal instability and analogously to fig. 4.3 b) breaks up into two bulges, as displayed fig. 4.7 b). Due to the proximity of the bulges to the domain boundary at $x = \pm L_x/2$, one of them can reach the boundary. Since periodic boundary conditions are applied, this state resembles a state where the liquid connects multiple adjacent wettability stripes by spreading over the less wettable area. This bulge and bridge state, which is shown in fig. 4.7 c) remains stable for a short time, after which the bridge accumulates the mass of the bulge such that only the bridge remains as the globally stable state, which is displayed in fig. 4.7 d).
The free energy diagram for this simulation is displayed in fig. 4.8. One can see that the ridge state is stable for longer times than in the previous simulations. Another distinguishing factor of this simulation is that the free energy shows a very steep decrease as the two bulges state relaxes to the bridge and bulge state. This steep decrease occurs as the droplet touches the boundary, thus making contact with its periodic counterparts. This contact corresponds to a sudden decrease of the curvature and, therefore, of the Laplace pressure. Due to the logarithmic scaling of the time axis, the plateau of the bulge and bridge state would be barely visible if it were not marked. It could, however, be recognised as the position at which the curve's steepness decreases significantly. The free energy of the meta-stable states and the time they were present in the simulation are given in table 4.3. It can be seen from these values that the bulge and bridge state remains present for a much shorter time than the other states.
While, on the one hand, the obtained results allowed insights into the dynamics exhibited by the liquid during the Rayleigh-Plateau instability, it also proves the functionality of the employed simulations as the results presented by Honisch et al. could be reproduced.

4.2.1.1 *Neumann Boundary Conditions*

Analogous to the previously considered system, one can investigate a domain where periodic boundary conditions are applied only along the y-direction, i. e., along the boundary located at $y = \pm L_y/2$ while

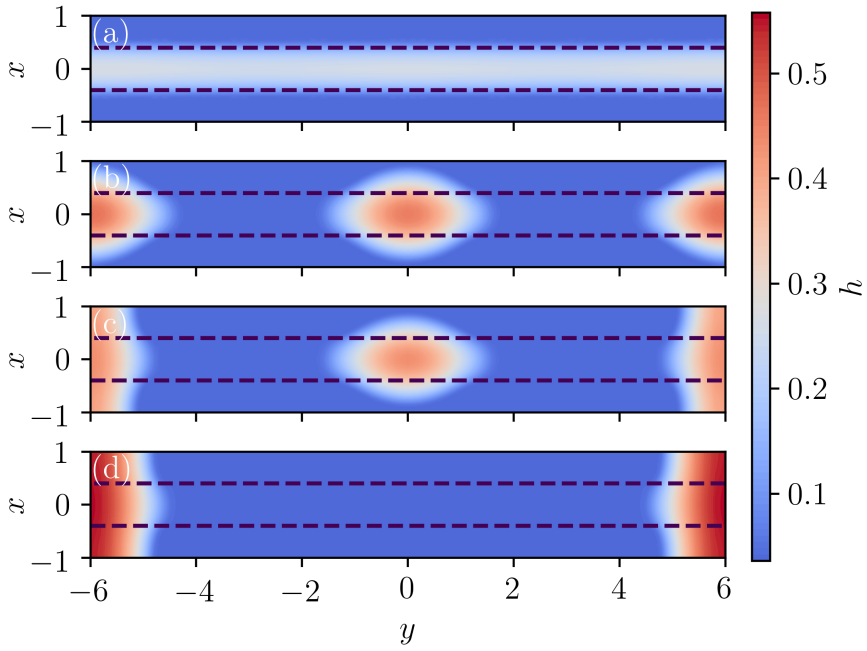

Figure 4.7: Snapshots obtained during the simulation of a homogeneous liquid film with $h_{\text{hom}} = 0.112$ on a heterogeneous substrate, with a wettability pattern given by eq. (3.1). The domain size was chosen as $L_x \times L_y = 2 \times 12$ while all other parameters are equal to the parameters given in the caption of fig. 4.3. a) and b) display a meta-stable ridge and two bulges states, respectively while c) shows a meta-stable bridge and bulge state. Panel d) displays the globally stable bridge state.

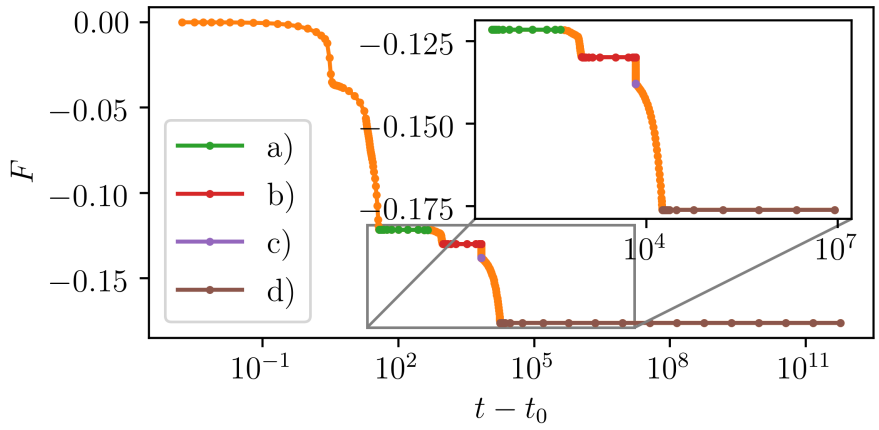

Figure 4.8: Free energy during the relaxation of a homogeneous film with $h_{\text{hom}} = 0.112$ on a heterogeneous substrate of size $L_x \times L_y = 2 \times 12$ where a wettability stripe pattern given by eq. (3.1) is employed. The wettability parameters are given in the caption of fig. 4.3. The handles in the legend correspond to the states displayed in fig. 4.7. The inset shows a close-up of the relaxation process starting from the meta-stable ridge (green) to the globally stable bridge state (brown).

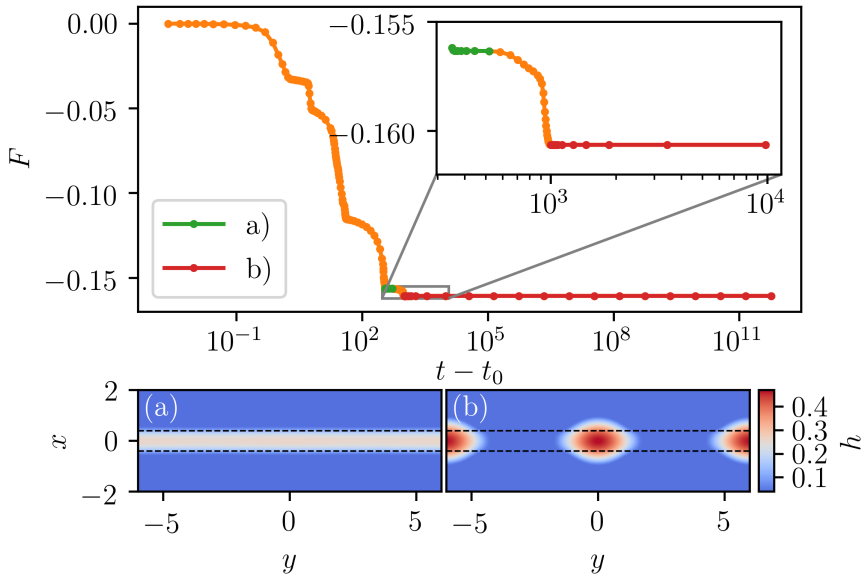

Figure 4.9: The upper panel displays the temporal evolution of the systems free energy during the relaxation of a homogeneous film analogous to fig. 4.4, where the only distinction lies in the here employed Neumann boundary conditions in x-direction. The meta-stable ridge and stable two bulges state are marked and their height profile portrayed in panel a) and b), respectively.

Neumann boundary conditions are applied at $x = \pm L_x/2$. The Neumann boundary conditions are the natural boundary conditions of the finite element method since they correspond to a vanishing boundary term [4]). These boundary conditions are, therefore, directly implemented into the employed residuals and Jacobian (c.f. section 2.2) without any need to apply them within the simulation code .
For the simulations performed here, all parameters remain the same as for fig. 4.3 such that differences in the liquid dynamics can solely be attributed to the change of boundary conditions. The lower panels of fig. 4.9 show snapshots obtained during the relaxation process of a homogeneous film as it was done in fig. 4.3. The upper panel displays the free energy during this relaxation process, where the free energies corresponding to the states displayed in a) and b) are marked. It is apparent, that the boundary conditions along the y-axis remain the same, since in fig. 4.9 b) droplets centered at the boundary, i. e., at $y = \pm L_y/2$ form. A result of the applied Neumann boundary conditions is the absence of the one bulge state, as the two bulges state does not relax further. The dynamics, therefore, only include a single meta-stable state. The applied boundary conditions, thus, have a significant impact on the exhibited Plateau-Rayleigh instability, as the simulation with Neumann boundary conditions results in different liquid dynamics with a decreased number of meta-stable states.

Table 4.4: Employed wettability patterns with the corresponding parameters ρ_{LW}, ρ_{HW}. The remaining parameters of the wettability profile are given as $ls = 0.06$, $x_A = 0.4$ and $c = 0$.

Name	ρ_{HW}	ρ_{LW}
S1	-0.5	0.5
S2	-1.0	1.0
S3	-1.0	-1.0

4.2.2 *Application of Switchable Substrates*

Within this section, switchable substrates, which were already used to induce a controlled movement of the liquid within chapter 3 and section 4.1, will be employed to manipulate and try to control the liquid dynamics during a Plateau-Rayleigh instability. The Plateau-Rayleigh instability was already investigated on a temporally constant wettability profile in section 4.2.1. While most of the parameters and boundary conditions used for fig. 4.3 will be retained, additionally, a switchable substrate will be applied. The switching process consist of changing the values for ρ_{HW} and/or ρ_{LW} at discrete times. The general shape of the wettability profile is conserved, whereas the wettability values change during the switching processes. Three different sets of wettability parameters will be used in the following. The respective values of ρ_{HW} and ρ_{LW} as well as the names associated with them are given in table 4.4. While all of these patterns *can* be described by eq. (3.1), S3 can be more easily defined as a homogeneous wettability profile with $\omega(\mathbf{x}, t) = -1$, i. e., the complete wetting case (c.f. section 2.1). A liquid exposed to S3 thus spreads out until it ultimately assumes its globally stable state of a homogeneous liquid film.
S1 corresponds to the wettability profile used in section 4.2.1. The dynamics can, therefore, be extracted from the previously performed simulation. S2 is equivalent to a version of S1 with an increased wettability contrast C_ρ, such that the highly wettable region corresponds to a completely wettable stripe. The equilibrium state, i. e., the state with the lowest free energy, of the S2 substrate is a homogeneous ridge on top of the highly wettable stripe resembling the state in fig. 4.3 b). In contrast to the ridge state obtained with S1, the ridge state on S2 is truly homogeneous, i. e., translation invariant along the y-axis. A cross-section of both ridge states along $x = 0$ is shown in fig. 4.10. Note that only the region close to the liquid-gas interface is displayed such that the difference between both ridge states appears larger than it is. The maximum deviation of the ridge on S1 relative to the translation invariant ridge on S2 is approximately equal to 7%. Further, it is important to note that the homogeneous ridge on S2 can only be obtained if the volume of the used liquid is small enough; otherwise,

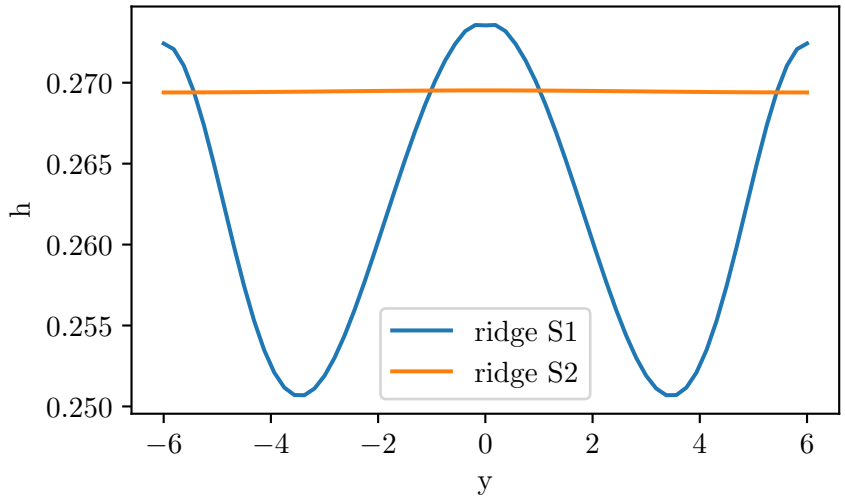

Figure 4.10: Cross-sections along $x = 0$ of the meta-stable ridge state on S1 (denoted as ridge S1) as well as the translation invariant globally stable ridge state on S2 (denoted as ridge S2).

also parts of the substrate with low wettability will be covered.

4.2.2.1 *Stabilisation of the two bulge state*

The two bulge state displayed in fig. 4.3 c) occurs only for a finite time, after which one of the bulges accumulates the mass of the other, resulting in the formation of a single bulge containing the entire liquid within the domain. In the following, an attempt will be made to stabilise this two bulges state, i. e., prevent the formation of a one bulge state.
The employed switching process includes three parts, where the first part consists of the relaxation of the homogeneous film on S1, analogous to fig. 4.3. In the end, the globally stable one bulge state displayed in fig. 4.3 d) is obtained. Once the one bulge state has formed, the second part of the switching process starts and the substrate's wettability profile is switched to S2. As previously mentioned, the globally stable state on S2 is equal to a completely homogeneous ridge. The one droplet state, therefore, relaxes until it has formed the translation invariant ridge on top of the highly wettable stripe. This relaxation process takes about $dt \approx 9000$. After the homogeneous ridge is obtained, the third and last part of the switching process starts, and the substrate is switched back to S1. Here the ridge again exhibits a transversal (Plateau-Rayleigh) instability analogous to section 4.2.1 and breaks up into two bulges. In contrast to the two bulges state shown in fig. 4.3 c), this state persists and no one bulge state forms.
A visualization of this switching process is displayed in fig. 4.11. Here

a rescaled version of the free energy $\tilde{F}$ for the different states occurring during the switching process is portrayed on the y-axis. The x-axis distinguishes the two employed wettability patterns, S1 and S2, where heatmaps of the wettability patterns are displayed underneath the corresponding labels.
$\tilde{F}$ is the free energy of the system shifted such that all values are positive, and the free energy of the equilibrium state for each respective substrate has a free energy of zero. This scaling is described by

$$\tilde{F} = \frac{F}{|F^{Si}_{\min}|} - \operatorname{sgn}(F). \tag{4.7}$$

Here $F^{Si}_{\min}$, $i = 1, 2$ is the free energy of the globally stable state for the substrates S1/S2. For S1 and S2, this corresponds to the free energy of the one bulge and homogeneous ridge state, respectively. $\operatorname{sgn}(F)$ denotes the sign function of the free energy.
Within fig. 4.11 the relaxation processes, which occur naturally, are marked as dotted arrows, whereas the artificially, i. e., via switching induced transitions, are marked as continuous arrows. States with nearly identical free energies, such that they would overlap if they were portrayed as the other states, are shown as two neighbouring lines. The linestyles distinguish between the substrates on which this state will occur naturally. For S1 continuous and for S2 dotted lines are being used. An example is the homogeneous ridge state *ridge S2* which occurs naturally on S2 and is thus represented by a dotted line. For S1, the ridge S2 state is displayed as a line of half the length of the ridge S2 state on S2 since, here, its free energy lies very close to the free energy of the ridge S1 state. This is also the case for the resulting stable two bulges state, which has a free energy close to the unstable two bulges state. The small deviations between the respective free energies demonstrate the similarity between the meta-stable states, naturally occurring during the Plateau-Rayleigh instability and the artificially created states, as well as their proximity in the free energy landscape.

To investigate the stability of the two bulges solution, obtained through the discussed switching process, the corresponding eigenvalues and eigenfunctions were calculated numerically. The imaginary parts of all calculated eigenvalues were equal to zero, as is expected by the gradient dynamics formulation of the used model[2]
The eigenfunction corresponding to the eigenvalue with the largest real part is displayed in fig. 4.12[3]. The corresponding eigenvalue λ is $\lambda = 1.3 \cdot 10^{-4}$. Since this value is larger than zero, one would expect the state to be unstable. Direct numerical simulations showed that the state does not exhibit any instability but remains stable even for

2 Since this a gradient dynamics formulation can not include oscillations in the exhibited dynamics whereas a eigenvalue with a non-vanishing imaginary part would correspond to oscillations.

3 Various other eigenmodes of the obtained two droplet state are shown in appendix B.1.

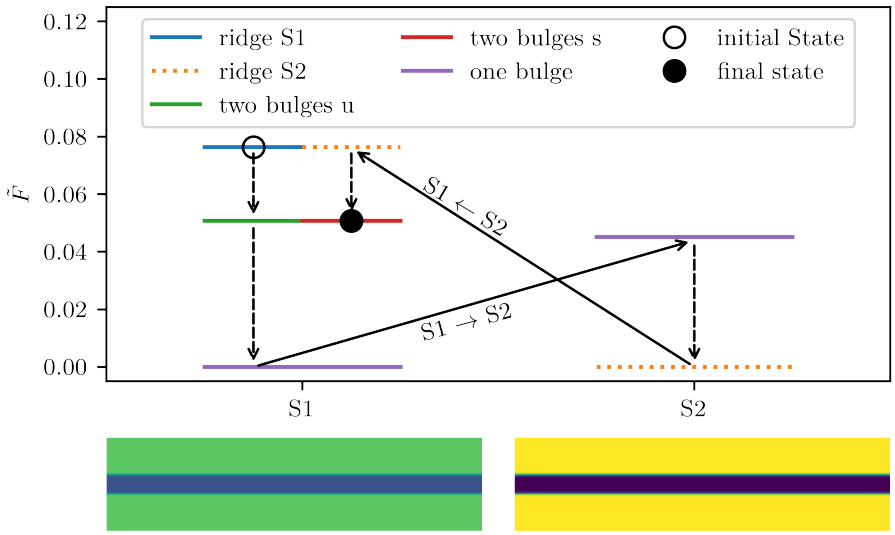

Figure 4.11: Visualisation of the switching pattern used for obtaining a locally stable two bulges state. A shifted version of the free energy (given by eq. (4.7)) for all states relevant during the switching process is displayed. The states denoted as *two bulges u* and *two bulges s* are the unstable and stable two bulges states, respectively. Dotted and continuous arrows, respectively, mark relaxations and switching processes. The two panels at the bottom portray the employed wettability profiles S1 and S2.

large integration times , i. e., $t = \mathcal{O}(10^{13})$. In order to test the stability with respect to distortions proportional to the determined eigenmode displayed in fig. 4.12, the height profile of the two bulge state $h_{\text{2bulge}}(x)$ distorted by the eigenmode $h_{\text{eigen}}(x)$ was used as an initial condition

$$h(x, t = 0) = h_{\text{2droplet}}(x) + \epsilon h_{\text{eigen}}(x). \tag{4.8}$$

Here ϵ is a parameter describing the strength of the distortion. If the two bulge state is unstable, as the determined eigenvalue suggests, the distortions should grow over time for an arbitrarily small value of ϵ. Numerical simulations using this initial condition for various values of ϵ showed that the distortions do not grow over time as long as $\epsilon \leq 0.06$ holds. It is important to note here that the eigenvectors were normalized to the interval $[-1, +1]$, such that the parameter $\epsilon = 0.06$ corresponds to a distortion of 15% relative to the maximum film height h_{max} of the two bulge state which is $h_{\text{max}} \approx 0.47$.
To rule out numerical pinning as a reason for the stability of the two bulges solution, the domain size was increased by 1% while maintaining the same liquid volume[4]. Using this slightly altered domain size, the switching pattern still resulted in the formation of the desired two bulges state. The two bulges state, therefore, is, contrary to the determined eigenvalue, a linearly stable state.

4 Excluding the precursor film volume.

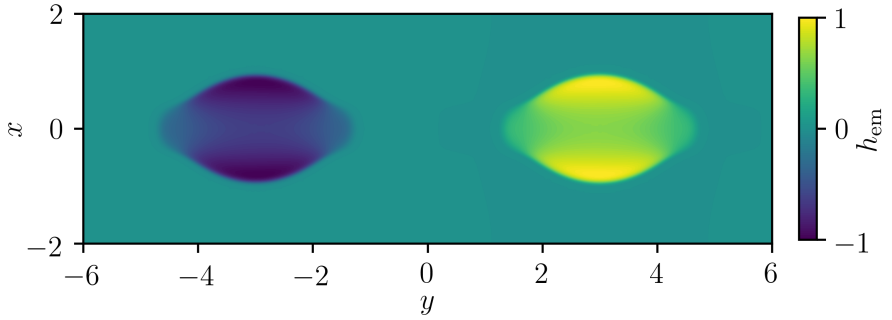

Figure 4.12: Eigenmode corresponding to the largest eigenvalue $\lambda = 1.3 \cdot 10^{-4}$ of the locally stable two bulges state. The values were normalised to the interval $[-1, 1]$.

4.2.2.2 *Stabilization of the ridge state*

Analogous to the preceding section in the following, a switching protocol to obtain a stabilised version of the meta-stable ridge state displayed in fig. 4.3 b) will be developed.
The switching scheme required to obtain a stabilised version of the ridge state is slightly more complex than the scheme for the two bulges state since it involves all three wettability profiles described in table 4.4.
A visualisation of the switching scheme analogous to fig. 4.11 is displayed in fig. 4.13, where the rescaled free energies of the relevant states, as well as the transitions between these states, are shown for the three employed wettability patterns. The initial state of the liquid film is again chosen as the ridge state on the substrate S1. The liquid relaxes until the one bulge state is obtained. The substrate is switched to S2, where the liquid takes on the form of the transversal invariant ridge on S2. Once the liquid has equilibrated on S2, the substrate is switched to S3, i. e., the homogeneous, completely wettable substrate. Here, the liquid ridge spreads out as it reduces its curvature. A cross-section along $y = 0$ of this broadened ridge in comparison to the S2 ridge is displayed in fig. 4.14. The portrayed state denoted as *broadened ridge* was obtained $dt = 1$ after the substrate was switched from S2 to S3. Comparing both displayed states, the broadening of the ridge is obvious. Additionally, due to the fast dynamics, the film height at the edge of the ridge, i. e., in the contact region, is slightly below the height of the precursor film.
After the broadened ridge portrayed in fig. 4.14 has formed, i. e., $dt = 1$ after the switch from S2 to S3 the substrate is switched back to the original wettability pattern S1. Here the liquid ridge contracts again as it is exposed to the stripe-like wettability pattern and assumes a form similar to the S1 ridge, which remains present for large integration times, i. e., $t = \mathcal{O}\left(10^{13}\right)$. Cross sections of this artificially created ridge state (denoted as *stable ridge*) and the naturally occurring meta-stable

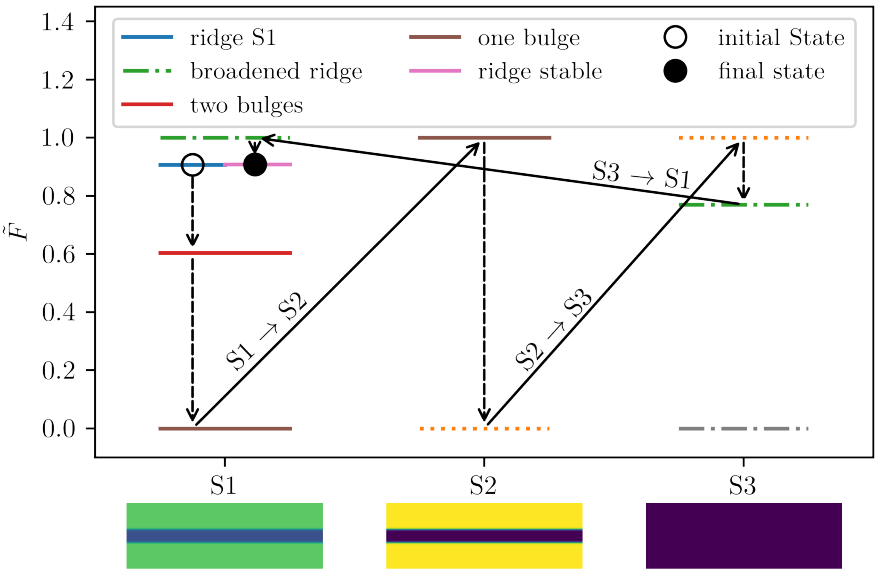

Figure 4.13: Visualisation of the switching pattern used for obtaining a locally stable ridge state. A shifted version of the free energy (given by eq. (4.7)) for all states relevant during the switching process is shown. Relaxations (dotted arrows) and switching processes (continuous arrows) are displayed. The three panels at the bottom portray the used wettability profiles S1, *S*2 and *S*3 from left to right.

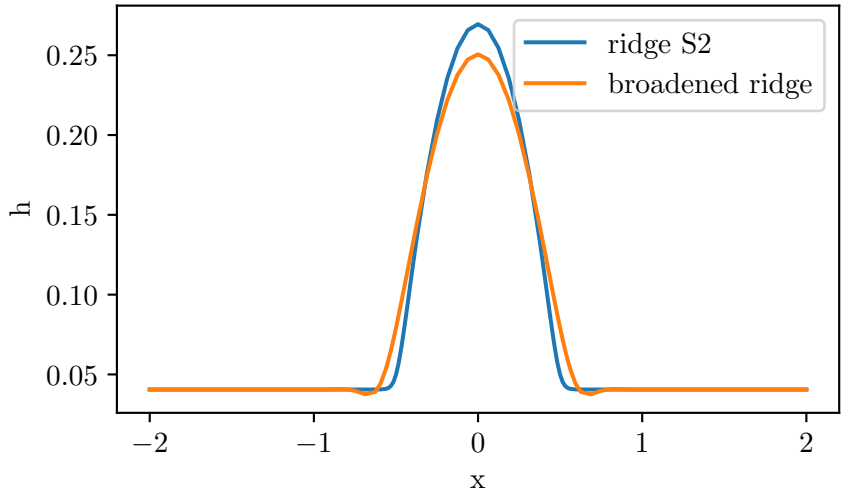

Figure 4.14: Cross sections along $y = 0$ of the stable ridge state on *S*2 (denoted as ridge *S*2) and the broadened ridge state on *S*3 (denoted as broadened ridge) obtained $dt = 1$ after the substrate was switched to *S*3.

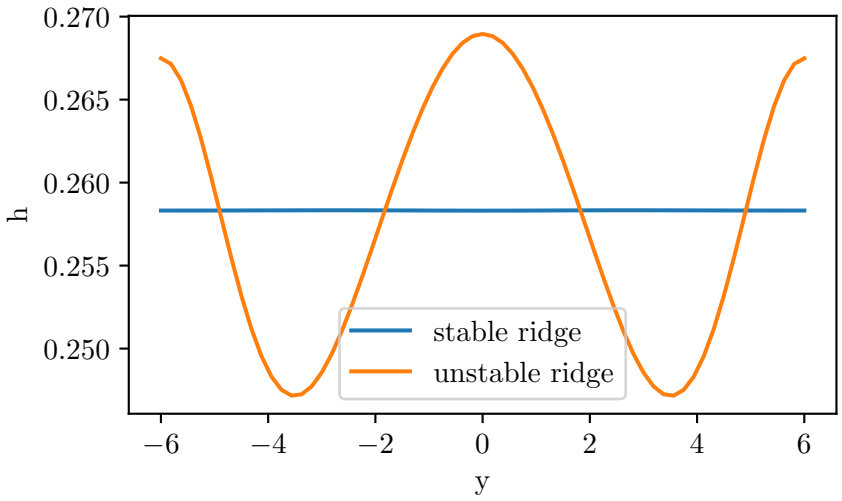

Figure 4.15: Cross sections along $x = 0$ of the stable ridge state on S1 (denoted as stable ridge) and the unstable ridge state on S1 (denoted as unstable ridge) obtained for the undisturbed Plateau-Rayleigh instability in section 4.2.1.

ridge state on S1 (denoted as *unstable ridge*) are displayed in fig. 4.15. The stable ridge is translation invariant along the y-direction. This feature is obtained due to the switching back to $S2$ where the ridge S2 state has formed, which is translation invariant (c.f. fig. 4.10) as well. In contrast to the previously considered switching pattern S1→S2→S1 the translation invariance is retained after switching to S1 in the case of the switching pattern considered here, such that the ridge does not exhibit any transversal instability.

Analogous to the stabilised two bulges state, the eigenvalues and eigenfunctions were numerically determined for the artificially obtained ridge state. Again all eigenvalues had a vanishing imaginary part. The eigenfunction corresponding to the eigenvalue with the largest real part $\lambda = 0.011$ is displayed in fig. 4.16. This eigenmode corresponds to the formation of the two bulge state (c.f. fig. 4.3 c)) obtained during the undisturbed Plateau-Rayleigh instability, i. e., two equidistant bulges positioned at the centre and boundary of the domain. Additional eigenfunctions are portrayed in appendix B.1. Since the eigenvalue belonging to fig. 4.16 is again larger than zero, the stability was analysed analogous to the two bulges state, i. e., the ridge state was perturbed proportional to the eigenmode displayed in fig. 4.16 using eq. (4.8). Here, $h_{\text{2droplet}}(x)$ needs to replaced with the artificial stable ridge state $h_{\text{ridge}}(x)$ and the eigenmode shown in fig. 4.16 needs to be used for $h_{em}(x, y)$.

Direct numerical simulations showed that the distortions did not grow over time if ϵ was chosen smaller than $1.9 \cdot 10^{-5}$. The obtained ridge state, therefore, is indeed stable. The switching scheme presented

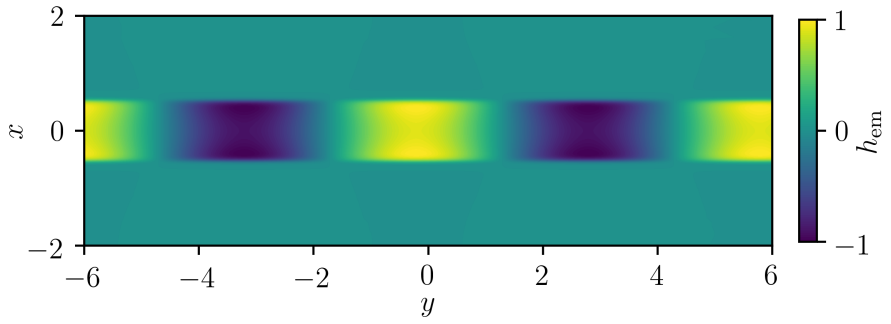

Figure 4.16: Eigenmode corresponding to the largest eigenvalue of the locally stable ridge state. The values were normalised to the interval $[-1, 1]$.

here can, thus, be used to obtain a stabilised version of the otherwise meta-stable liquid ridge state.
It is interesting to compare the strengths of the perturbations leading to an instability for the two artificial states. The minimum value of ϵ leading to an instability for the two bulges state is two orders of magnitudes larger than the value for the ridge state. Comparing this difference to the times the states were present at the corresponding plateaus in the case without switching (c.f. fig. 4.4 and table 4.1), one can see that the time the ridge state exists is also two orders of magnitude smaller than the time the two bulge state is present.

4.2.3 *Two Interacting Stripes*

Due to the employed periodic boundary conditions, the interaction between the liquid on neighbouring wettability stripes is already included in the simulations. However, the periodic boundary conditions only simulate neighbouring stripes of equal liquid configurations. The interaction of two stripes should also include the formation of different configurations on neighbouring stripes, e. g. checkerboard patterns of two bulges states.
To better understand the interaction of neighbouring stripes, this section focuses on the explicit simulation of two wettability stripes. For this, the previously simulated domains were extended in the x direction by L_x, i. e., the domain considered in the following was chosen to include two of the previously simulated domains on top of each other. The domain size is, therefore, equal to $L_x \times L_y = 8 \times 12$. In order to also obtain the appropriate stripe pattern $c_1 = -\frac{L_x}{2}$, $c_2 = \frac{L_x}{2}$ need to be employed, while all other wettability parameters remain unchanged. The simulations now include two stripes located at $x = \pm L_x/2$, such that the interactions with the liquid on these stripes can be directly simulated, and the configurations of the liquid on the stripes do not need to be identical.

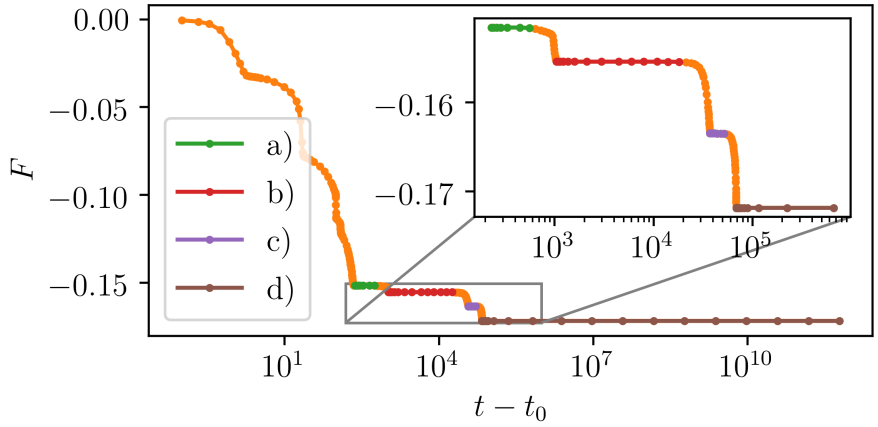

Figure 4.17: Time series of of the free energy F during a direct numerical simulation of the thin-film equation with $h_{\text{hom}} = 0.076$ on a pre-patterned substrate with two neighbouring wettability stripes given by eq. (3.1). The free energy plateaus are portrayed in different colours, while their corresponding states are shown in fig. 4.18. The parameters of the simulation are $L_x = 8$, $L_y = 12$, $c_1 = -2$, $c_2 = 2$ all other parameters as well as the initial condition are equal to the ones given in the caption of fig. 4.4.

In the following, the simulations performed in section 4.2.1 will be referred to as simulations of a single domain, while the simulations of the extended domain with two wettability stripes will be denoted as simulations of two domains.
Corresponding to fig. 4.3 a homogeneous film with the height $h_{\text{hom}} = 0.076$ was employed as the initial condition. The meta-stable states obtained during the simulation are displayed in 4.18. Those shown in fig. 4.18 a), b) and c) correspond to an extension of the states obtained for the simulation of a single stripe, i. e., the states displayed in fig. 4.3 b), c) and d), respectively, to two stripes. In contrast to these direct extensions, the one bulge state shown in fig. 4.18 d) has no analogue in the simulation of a single wettability stripe since the symmetry between the liquid on the two stripes is broken, and all liquid within the domain has accumulated on a single stripe.
Due to the extended number of states possible, compared to the simulation of a single domain, the outcome of the switching patterns employed for obtaining stabilised versions of the ridge and two bulges states may be altered.
Due to symmetry breaking between the deposited liquid on the upper and lower stripe, the switching pattern can not be applied to the one bulge state. The switching, therefore, has to occur before the symmetry is broken[5]. If one applies the switching pattern discussed

5 The symmetry can also be restored by either using a completely wettable substrate which results in a homogeneous distribution of the liquid (equivalent to the initial condition) or more complex switching procedures resulting in an equal distribution of the liquid on both stripes.

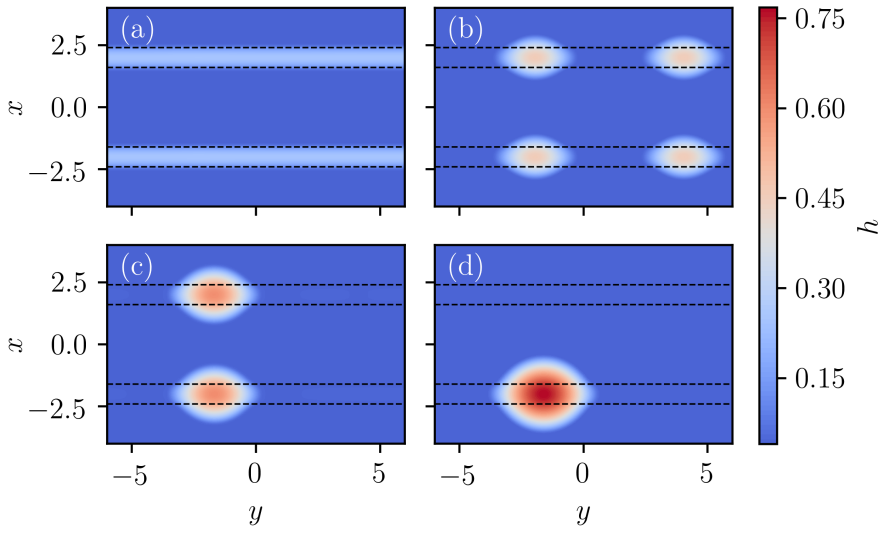

Figure 4.18: States obtained during the simulation of two interacting stripes positioned at $c_1 = -\frac{L_x}{2}$, $c_2 = \frac{L_x}{2}$. The domain size is $L_x \times L_y = 8 \times 12$. All other parameters of the wettability profile as well as the initial condition are the same as those given in the caption of fig. 4.3. The following states are shown a) two stripes, b) four bulges, c) two bulges, and c) one bulge.

in section 4.2.2.1 to the two bulges state (c.f. fig. 4.18 c)) the four bulges state, i. e., the extension of the two bulges state to two wettability stripes, is not obtained. Analogous to the previous case, the two bulges state will deform into a two ridge state after the substrate is switched to S2. After switching back to S1, the liquid will first take on the four bulges state portrayed in fig. 4.19 a). The symmetry of the liquid distribution on the two stripes is broken for this state. Both stripes, therefore, exhibit a Plateau-Rayleigh instability and break up into two bulges each. Caused by the interaction of the liquid on the neighbouring stripes, a checkerboard pattern of the bulges forms as they try to maximise their distance relative to each other, while remaining on the wettability stripes. After a short time, the bulges on the lower stripes start to accumulate the mass of the upper bulges, thus forming a two bulges state displayed in fig. 4.19 b) which, in contrast to the two bulges state displayed in fig. 4.18 c), features two bulges on the same stripe. This state remains present for large simulation times, i. e., $t = \mathcal{O}\left(10^{13}\right)$. The switching pattern, therefore, needs further adaptions to obtain the desired four bulges state. To obtain this state it is relevant to ensure an equal distribution of mass between the neighbouring stripes at the beginning of the switching pattern.
For different configurations of the wettability pattern, i. e., other distances $d = c_2 - c_1$ between the stripes or different $\rho_{\mathrm{HW}} / \rho_{\mathrm{LW}}$ values, diverse liquid dynamics can be observed. Decreasing the distance of the highly wettable stripes, for example, will increase the effect the two modelled stripes have on each other while, at the same time, the

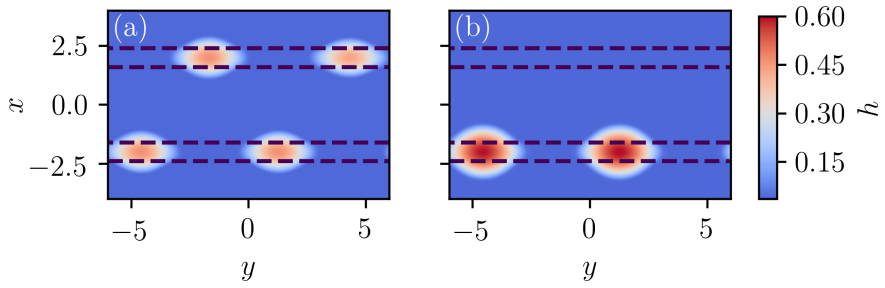

Figure 4.19: States obtained while simulating the switching pattern portrayed in fig. 4.11 on a domain containing two stripes. The simulation parameters are described in fig. 4.18. a) shows the shifted four bulges state (c.f. fig. 4.18 b)), which occurs shortly after switching back to S1 . Panel b) displays the stable two bulges on one stripe state.

effect the periodic counterparts of the stripes have on the modelled domain is reduced.

Figure 4.20 shows the time series of the free energy F during a simulation using the same parameters as for Fig. 4.17 except for a decreased stripe distance from $d = 4$ for fig. 4.17 to $d = 3$ for fig. 4.20. It is apparent that compared to fig. 4.17 one energy plateau is missing. Further, the existing plateaus have decreased in length. The states corresponding to the marked free energies are portrayed in fig. 4.21. Comparing these states to the previously considered periodic stripe pattern, it is apparent that the meta-stable states differ from each other. For the smaller stripe distance $d = 3$, the two ridge state (c.f. fig. 4.17 b)) did not form, since the ridges break up into four bulges, as shown in fig. 4.21 a), before they have accumulated all the liquid within the domain. The four bulges state deforms, as the mass of the bulge in the middle of the domain on the upper stripe is accumulated by the two bulges at the boundary of the domain. The mass is equally split between these two bulges while the third one at the centre of the domain on the bottom stripe remains at a constant volume. This state is displayed in fig. 4.21 b). After some time, the smaller bulge is absorbed by the larger one on the lower stripe. The resulting state is portrayed in fig. 4.21 c). Note that this state does not correspond to a meta-stable state and is only portrayed to allow for a better understanding of the liquid dynamics. Due to the uneven distribution of mass between the two bulges, the more massive one can accumulate all mass within the domain, thus leading to a stable one bulge state shown in fig. 4.21 d).

The impact of the periodic boundary conditions, i. e., the periodic stripe pattern, on the modelled two stripe domain can be investigated if the boundary conditions are switched to Neumann boundary conditions along the x-direction. Performing a direct numerical simulation using the same parameters as those used in fig. 4.17 results in analogous liquid dynamics. The differences to the results shown in Fig. 4.17

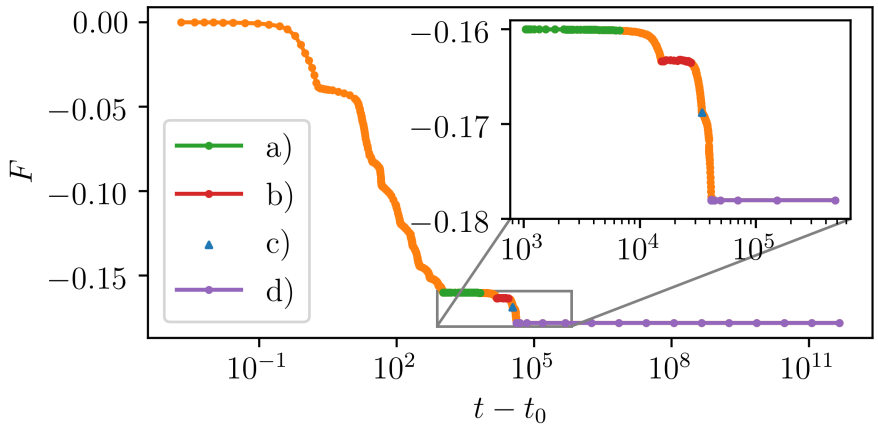

Figure 4.20: Time series of the free energy F during the relaxation of a homogeneous liquid film with $h_{hom} = 0.076$ on a pre-patterned substrate with two wettability stripes. All parameters are the same as those given in the caption of fig. 4.17 except for the positions of the stripes which are chosen as $c_1 = 1.5$ and $c_2 = -1.5$. The F plateaus are portrayed in different colours where the labels refer to the illustrations in fig. 4.21. In addition to the plateaus, a state relevant for understanding the liquid dynamics is marked as a blue triangle in the free energy diagram and additionally displayed in fig. 4.21 c).

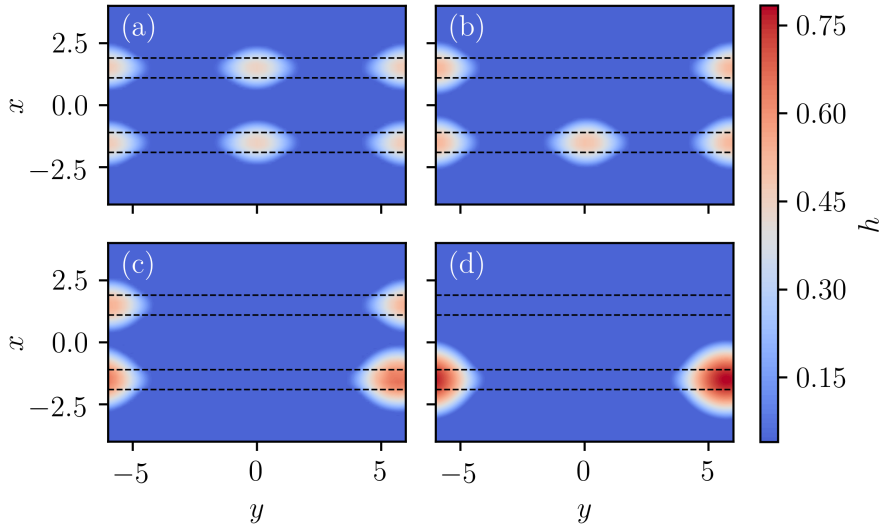

Figure 4.21: Snapshots of the liquid height profile corresponding to the marked states in fig. 4.20. While a) and b) correspond to metastable states and d) to a stable state, c) is displayed only to allow for a better visualisation of the liquid dynamics.

lie in slightly changed stability times, nevertheless, in general, the dynamics remained unchanged, and all expected meta-stable states could be observed. The boundary conditions, therefore, only have a small influence on the liquid dynamics for two wettability stripes compared to the influence on the liquid dynamics for a single simulated wettability stripe (c.f. section 4.2.1.1).

5 2D INCLINED SUBSTRATE

Within this chapter, an inclined substrate will be considered. Previously, the inclination angle α incorporated into the thin-film equation 2.1 was kept at $\alpha = 0$. Therefore, no driving forces acted on the droplet. In the following, however, a non-vanishing inclination angle will be employed, such that the substrate is inclined along the x-axis. A visualisation of the inclined one-dimensional substrate is displayed in fig. 5.1. For positive inclination angles, the driving force acts towards increasing x-values. In this chapter the x-coordinate will always be portrayed along the horizontal axis such that the driving force acts to the right. The inclination angle α will, despite the applied nondimensionalisation (c.f. appendix A), be given in degrees in the following to allow better readability.
This chapter will be structured as follows. While section 5.1 focuses on observing the naturally occurring pearling instability of a liquid droplet on an inclined substrate, section 5.2 considers various methods of controlling the dynamics of liquid droplets on inclined substrates. The employed methods include a spatially and temporally modulated wettability pattern in sections 5.2.2 and 5.2.3 as well as a time-dependent inclination angle in section 5.2.1. In particular, the application of these methods to liquid droplets exhibiting a pearling instability will be considered.

5.1 PEARLING INSTABILITY

Liquid droplets placed on an incline, i. e., experiencing a certain lateral driving force, can exhibit a so-called pearling instability. For a fixed

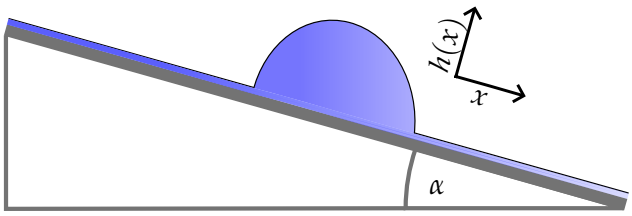

Figure 5.1: Illustration of a liquid droplet on an inclined substrate. The liquid, including the precursor film, is shown in blue, whereas the substrate is shown in gray. Additionally, the inclination angle α and the employed coordinate system are displayed.

liquid volume (lateral driving force), this requires a lateral driving force (liquid volume) beyond a certain critical value [14]. For a fixed volume V (fixed contact angle α) a critical inclination angle α_c (critical volume V_c) can be defined such that for $\alpha > \alpha_c$ ($V > V_c$) a pearling instability occurs. The instability results in the emission of satellite droplets in the direction of increasing substrate height opposite to the direction of movement [34]. The volume of the emitted satellites depends on the volume of the droplet they were emitted from and the inclination angle.

To illustrate the general dynamics of the pearling instability, snapshots obtained during the simulation of a droplet placed on an inclined substrate are shown in fig. 5.2. As the initial condition eq. (4.1) was chosen with $h_0 = 2.4$, $x_0 = 0$, $y_0 = 0$, such that the maximum is positioned at the centre of the domain. The simulated domain size is chosen as $L_x \times L_y = 30 \times 15$, while the inclination angle is set as $\alpha = 65°$. The employed value of α exceeds the critical inclination angle (c.f. [12]) such that the exhibition of a pearling instability is ensured.

Figure 5.2 a) shows the droplets initial form given by eq. (4.1). It has not yet started to deform such that the contact region between the substrate and the droplet is circular. With increasing times, the droplet starts to deform and elongates due to the driving force. This elongation process persists such that a tail starts to form. The corresponding state is portrayed in fig. 5.2 b). As an increasing amount of liquid accumulates at the end of the tail, the elongated droplet ultimately breaks up into two distinct droplets as shown in fig. 5.2 c). The volume of the emitted droplet is smaller than the critical volume ($V < V_c$) such that it does not exhibit a pearling instability but rather slides down the incline linearly stable. The main droplet, on the other hand, remains at a volume larger than the critical one and therefore continues to elongate, resulting in the emission of another satellite droplet shown in fig. 5.2 d). This process continues, and a third satellite droplet is emitted, shown in fig. 5.2 e). As mentioned before, the mass emitted from the droplet during the pearling instability depends on the volume of the droplet itself. Therefore, the volume of the satellite droplets can be ranked according to their order of emission. This relation between the satellite droplets can best be observed for the first two satellite droplets in fig. 5.2 d).

Since the velocity of the droplets is proportional to their mass [14], and periodic boundary conditions are applied, the more massive main droplet can catch up with the satellite droplets and absorb them after some time. A snapshot of the recombination is shown in Figure 5.2 f). Once the droplets connect, the base area drastically increases, allowing the liquid of the main droplet to quickly move to the front of the elongated droplet. This results in a further elongation and the emission of another satellite droplet.

Due to the periodic boundary conditions, the system exhibits a cyclic

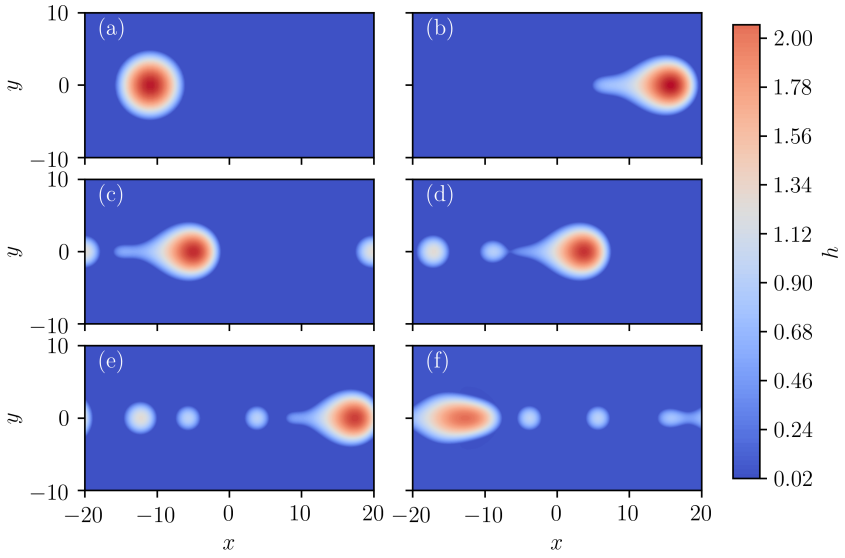

Figure 5.2: Snapshots of the liquid obtained during a direct numerical simulation of a droplet on an incline exhibiting a pearling instability. The initial condition eq. (4.1) was chosen with $h_0 = 2.4$, $x_0 = 0$, $y_0 = 0$. A domain of the size $L_x \times L_y = 30 \times 15$ was chosen and the inclination angle set to 65°. The time increases from a) to f) in irregular steps. a) displays the initial droplet, which elongates, resulting in the state shown in b). c) d) and e) display the main droplet with one, two and three emitted satellite droplets, respectively. The main droplet recombines with its satellite droplet in f). Due to the main droplet's elongated state at the recombination time, it emits another satellite droplet.

behaviour. The liquid dynamics during the pearling instability strongly depend on the chosen liquid volume, the inclination angle, and the considered domain size. For large inclination angles (volumes), the main droplet can emit more satellite droplets over the same distance, while for a larger domain size, it takes longer for the droplets to recombine, thus increasing the time available for the elongation and separation process. For the simulation shown in fig. 5.2 the volume (inclination angle) was chosen to be relatively large such that the main droplet exhibits multiple pearling instabilities. In general, different regimes of the pearling instability exist, and phenomena like period doubling and chaos can be observed when considering the volume of the emitted droplets for different inclination angles [14]. A variety of these regimes are being discussed in appendix B.2. Note that these periodic dynamics are a result of the employed periodic boundary conditions. They can not be observed during experimental considerations of single droplets on inclined substrates.
During the course of section 5.2.1, the initial condition used for fig. 5.2 will be employed such that the results obtained here can be used as a reference.

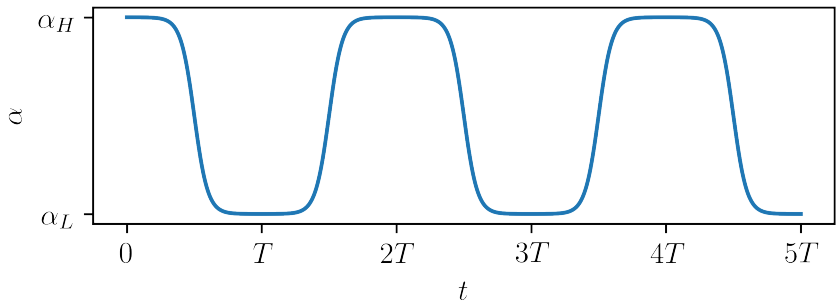

Figure 5.3: Visualisation of the employed inclination angle switching pattern.

5.2 CONTROLLING LIQUID DYNAMICS ON INCLINED SUBSTRATES

The results obtained for the application of horizontal switchable substrates to control liquid dynamics, discussed in chapter 3 and section 4.2 showed a multitude of possible methods for fluid manipulation. The applicability of these methods, including moving as well as stationary switchable wettability patterns, for liquid structures on inclined substrates will be investigated within this section. In addition to these methods, a time-dependent inclination angle $\alpha = \alpha(t)$ will be used as another control mechanism for the exhibited liquid dynamics. Emphasis is placed on applying these control methods in the context of the previously discussed pearling instability.

5.2.1 *Inclination Angle Switching*

In the following a time-dependent inclination angle $\alpha = \alpha(t)$ will be considered. The temporal behaviour of the inclination angle is chosen analogous to the spatial behaviour of the previously considered wettability pattern (c.f. eq. (3.1)) and is given by

$$\alpha(t) = \alpha_0 + K_\alpha \tanh\left(\frac{\tilde{t} - T/2}{ls_\alpha}\right) \tanh\left(\frac{\tilde{t} - 3T/2}{ls_\alpha}\right), \tag{5.1}$$

with the abbreviations

$$\tilde{t} = \mathrm{mod}\,(t, 2T)\,,\ \alpha_0 = \frac{\alpha_\mathrm{h} + \alpha_\mathrm{l}}{2},\ K_\alpha = \frac{\alpha_\mathrm{h} - \alpha_\mathrm{l}}{2}. \tag{5.2}$$

A visualisation of the α switching procedure is displayed in fig. 5.3. The inclination angle is switched smoothly between the values α_h and α_l. The smoothness of the transition is given by ls_α, i. e., the inverse of the inclination at the point of steepest slope. The modulo function included within the definition of $\tilde{t}$ maps the time to the interval $t \to \tilde{t} \in [0, 2T)$ such that the pattern repeats itself after $t = 2T$, i. e., the period is equal to $2T$. The terms $-T/2$ and $-3T/2$ determine the time at which the switches occur. Starting with α_h the inclination is switched to α_l at $t = T/2$ and back to α_h at $t = 3T/2$. Note that the switching times correspond to the times when the inclination angle

changes most rapidly, i. e., the points of steepest slope. Since the transition is chosen to be smooth, exact switching times can not be specified. A simulation was performed, where the initial configuration was chosen as a droplet given by eq. (3.10) with $h_0 = 2.4$. For the switching pattern of the inclination angle the parameters $\alpha_h = 65°$, $\alpha_l = 15°$, $T = 200$ and $ls_\alpha = 20$ are being employed. The domain size was chosen as $L_x \times L_y = 30 \times 15$. The upper panel of fig. 5.4 shows the relevant part of the employed α switching pattern. The times and α values at which the states shown in the panels a) - d) were obtained are marked by circles, accompanied by the corresponding letters. Figure 5.4 a) shows the droplet undergoing a pearling instability, while the substrate is inclined at $\alpha \approx \alpha_h$. The instability continues even though the inclination angle is reduced, resulting in the emission of a satellite droplet and the formation of a tail at the rear of the main droplet, as shown in fig. 5.4 b). Due to the reduction of the inclination angle, the droplets experience less driving force and, thus, assume a more spherical shape. While this effect is not apparent for the satellites due to their small volume, it can be observed for the main droplet comparing fig. 5.4 b) and c). At the time of switching the main droplet has already formed a second satellite droplet, which is still connected to the main droplet by a thin liquid layer in fig. 5.4 b). The contraction of the main droplet leads to a retraction of this liquid bridge (cf. fig. 5.4 c)) and thus a separation of the main droplet from its second satellite droplet fig. 5.4 d). Once all droplets have assumed their spherical-cap shapes, they slide down the incline at a constant shape. Due to the volume difference, the satellite droplets can be caught by the main droplet. Even after the main droplet has accumulated its initial mass it does not exhibit another pearling instability before the inclination angle α is switched back to $\alpha = \alpha_h$.

As it is the case for the cycles during the exhibition of a pearling instability on an inclined substrate with a constant inclination angle, the dynamics during one period of the switching pattern strongly depend on the previous dynamics as well. These result in different initial elongations of the droplet at the beginning of a new period, thus, leading to a change in the times required for the emission of satellite droplets. Figure 5.5 illustrates the influence of the previous dynamics. Here the upper panel again displays the inclination angle for various times while panels a) - d) show four snapshots of the height profile. These were obtained two switching periods later than those displayed in fig. 5.4. The states shown in fig. 5.4 a) and b) correspond to the same times as fig. 5.5 a) and b) relative to the switching times. Comparing these states, one can see that, due to the previous dynamics, the pearling instability in fig. 5.5 a) has not yet progressed as far as in fig. 5.4 a). While the instability nevertheless occurs, and a satellite is emitted, the tail of the main droplet, formed in advance of the second emission, is less pronounced when the contraction of the

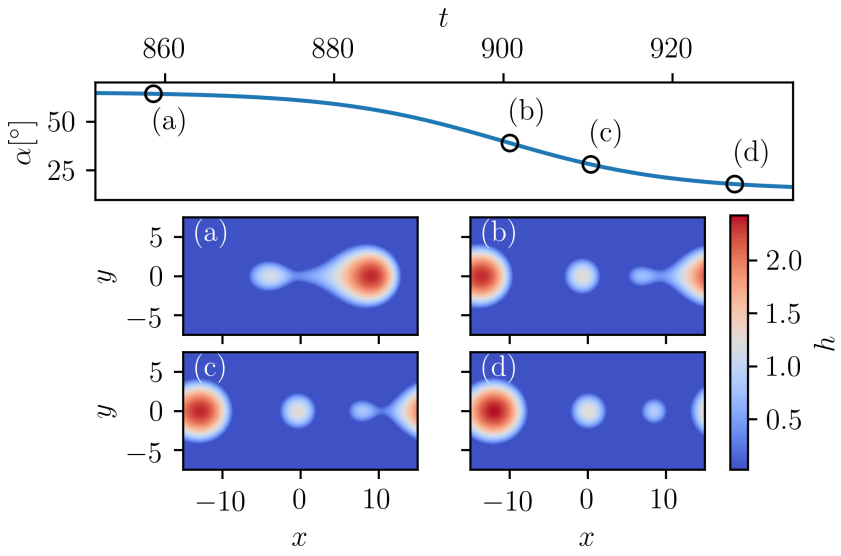

Figure 5.4: The upper panel displays the temporal evolution of the inclination angle $\alpha(t)$ during a simulation using the inclination angle switching pattern given by eq. (5.1), with $\alpha_h = 65°$, $\alpha_l = 15°$, $T = 200$ and $ls_\alpha = 20$. The size of the simulated domain was chosen as $L_x \times L_y = 30 \times 15$. The times and inclination angles corresponding to the snapshots of the height profile displayed within panels a) - d) are marked by circles and labelled accordingly.

droplet occurs (cf. fig. 5.5 b)). As a result of the contraction, the tail completely retracts back into the droplet, resulting in two spherical droplets shown in fig. 5.5 d) instead of three, as was the case for fig. 5.4. Due to the switching of the inclination angle the second emission was, therefore, prohibited.

Choosing the switching period small enough, such that the droplet cannot yet form a pronounced tail during $\alpha \approx \alpha_h$, one can prevent the pearling instability altogether. The necessary switching period can be determined by starting at a small period T and increasing it after each switch from α_h to α_l. Once the contraction of the liquid, induced by the inclination angle switching, leads to the emission of a satellite droplet, the necessary switching period has been surpassed.

Using the same initial condition and domain size as for figs. 5.4 and 5.5 a corresponding simulation was performed. Increasing the switching period by $dT = 10$ after each switch, the critical switching period was determined as $T = 150$.

A parameter that can be used to visualise the contraction behaviour of the liquid is the elongation E of the droplet. It corresponds to the maximum extension of the droplet along the x-direction. Since no forces act parallel to the y-direction, the maximum extension occurs along $y = 0$ for the employed initial condition. The elongation of the

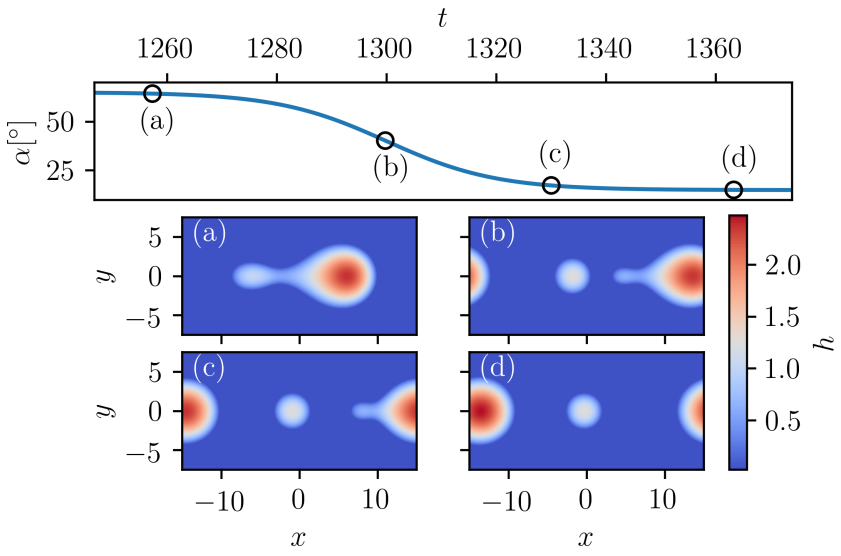

Figure 5.5: Visualisation of the liquid dynamics during an α switching process, analogous to fig. 5.4. The displayed results were obtained during the same simulation as those shown in fig. 5.4.

droplet can therefore be calculated by determining the interval $[x_l, x_r]$ such that

$$h(x, y = 0, t) > h_p, \forall\, x \in [x_l, x_r], \tag{5.3}$$
$$h(x, y = 0, t) <= h_p, \forall\, x \notin [x_l, x_r], \tag{5.4}$$

and calculating the difference $E = x_r - x_l$. Note that the periodic boundary conditions need to be considered during the calculation.
Snapshots of a direct numerical simulation using $T = 150$ are displayed in fig. 5.6 a) - d). The upper panel of fig. 5.6 shows the temporal evolution of the elongation E of the liquid droplet (blue) and the applied inclination angle (black) during the simulation.
As seen in the upper panel, the elongation exhibits a periodic behaviour, where the period is equal to the period of the employed switching pattern. These periodic dynamics show that the pearling instability can be prevented with the employed parameters. The elongation and time corresponding to the states depicted in panels a) - d) are marked and labelled accordingly. Since the dynamics are periodic, the portrayed states, obtained during multiple periods, all occur during a single elongation and contraction cycle.
The state displayed in fig. 5.6 a) corresponds to the equilibrium shape of the liquid on a substrate with $\alpha = \alpha_l$. Increasing the inclination angle leads to an increasing elongation (c.f. fig. 5.6 b)). The state of maximum elongation is displayed in fig. 5.6 c). One can observe in the upper panel that the state of maximum elongation corresponds to $\alpha = \alpha_{\mathrm{me}} < \alpha_h$. Therefore also inclination angles α, for which $\alpha_{\mathrm{me}} < \alpha < \alpha_h$ holds, lead to a further elongation of the liquid. Only

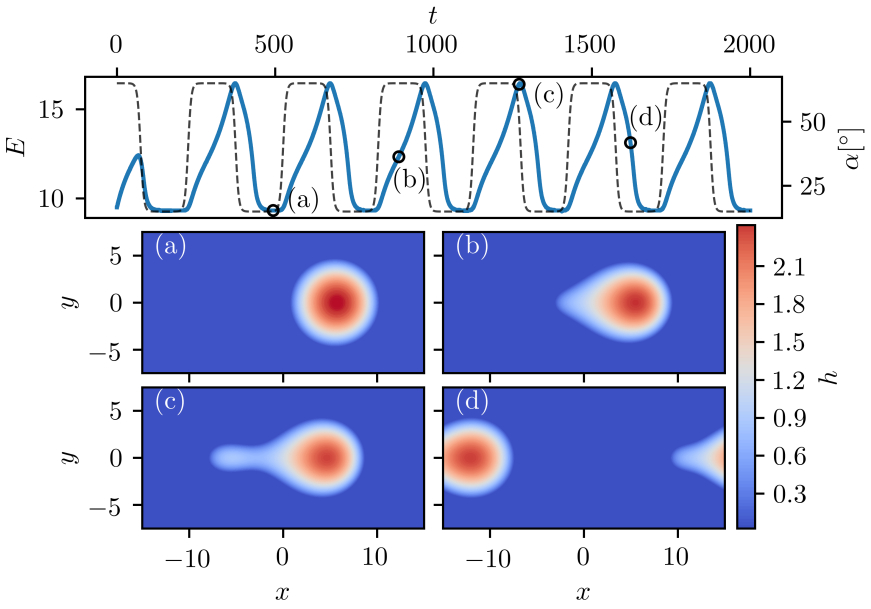

Figure 5.6: The upper panel displays the elongation E of the liquid droplet as well as the inclination angle α during the simulation of a droplet exhibiting a pearling instability while the emission of satellite droplets is being prohibited through periodic switches of the inclination angle, given by eq. (5.1) with $T = 150$, $\alpha_h = 65°$, $\alpha_l = 15°$. Circles indicate the time corresponding to the states shown in a), b), c), and d). The states were obtained during multiple switching periods but exhibit themselves during each switching period due to the periodic liquid behaviour. a) displays the state for $\alpha = \alpha_l$ with an almost spherical cap shape. The elongation increases with the inclination angle, where the droplet first forms a cusp as shown in b), which elongates further, resulting in a pronounced tail shown in c). Once the inclination angle is reduced below a certain critical value, the droplet contracts again, shown in d), after which the pattern and states repeat themselves.

once $\alpha \leq \alpha_{\text{me}}$ is applied, the contraction starts, leading first to a partly contracted droplet displayed in fig. 5.6 d) and then again to the fully contracted droplet with a spherical base area shown in fig. 5.6 a). Now the dynamics repeat themselves. The droplet, therefore, does not emit any satellite droplets but slides down the incline as a single connected liquid structure.

As an optimisation of this control mechanism, the time for which α_l is employed during each switching period may be reduced since most of the droplets contraction occurs quickly after switching to α_l. Additionally, one could investigate the influence of the value chosen for α_l. It is to be expected that relatively small differences in the employed values for α_h and α_l should result in a rapid contraction and thus allow the construction of a control mechanism, as long as $\alpha_l < \alpha_c$. Using this

method, one can prevent the occurrence of a pearling instability of the droplet while it flows down the incline. In general, droplets of arbitrary volumes can move down an incline linearly stable, as long as the inclination angle is chosen small enough. This, however, restricts the inclination angle and, thus, the possible droplet velocity. If the aim is to move down the incline as fast as possible, this method may be employed to ensure a stable droplet. Additionally, one can think about using appropriate switches to obtain a desired series of droplets. Since the domain is not periodic in experiments, the satellites can not be absorbed. Thus at the end of the incline, one obtains a series of droplets, whose number and volume depend on the inclination angle, the initial volume, and the length of the incline. Reducing the inclination angle below the critical one or using the discussed method of stabilising the flowing droplet one can create a variable number of droplets.

5.2.2 *Pinning*

This section will investigate the pinning of liquid droplets on an incline. Since droplets of arbitrary height placed on a homogeneous substrate with $\alpha > 0°$ will inevitable start to slide down the incline, an artificial method must be considered for pinning the droplets [13]. Here, an inhomogeneous circular wettability pattern given by

$$\omega(\mathbf{x}) = \rho_0 + C_\rho \tanh\left[\frac{x_A + s(\mathbf{x})}{ls}\right] \tanh\left[\frac{s(\mathbf{x}) - x_A}{ls}\right]. \tag{5.5}$$

similar to eq. (3.1) will be employed. ρ_0 and C_ρ also retain their definition given by eq. (3.2). The parameter $s(\mathbf{x})$ describes the distance from the centre of the wettability spot and is equal to

$$s(\mathbf{x}) = \sqrt{(x - c_x)^2 + (y - c_y)^2}. \tag{5.6}$$

The equation results in a circular spot of high wettability ρ_{HW} and a surrounding area of low wettability ρ_{LW}. The pattern is displayed in fig. 5.7. The parameters c_x and c_y determine the position of the circle's centre while x_A is equal to the radius of the circle, i. e., the shortest distance between the circles centre and the point of steepest slope of the wettability profile. The slope's absolute value at the steepest slope again equals $1/ls$. Due to the employed form of $s(\mathbf{x})$ a cross-section of the wettability profile along any axis through the point $x = c_x$, $y = c_y$, is equal to the one-dimensional wettability pattern shown in fig. 3.1 with the x-axis equal to the distance from the centre of the circle.

In chapter 3 and section 4.1 a droplet on a horizontal substrate experiencing a wettability gradient was considered. Since it is energetically favourable for the droplet to cover the highly wettable area, a movement towards this region is induced. While in chapter 3 and section 4.1 the wettability profile was used to induce movement, in the following,

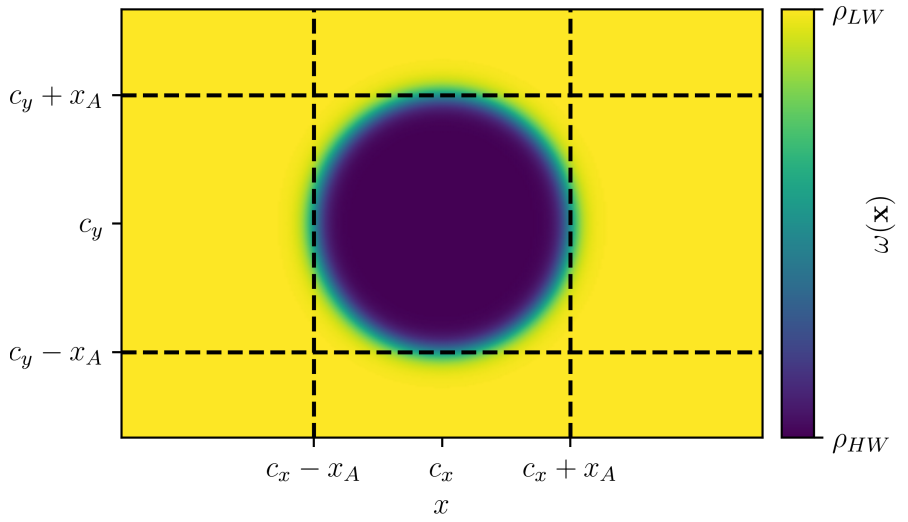

Figure 5.7: Visualisation of the employed wettability spot profile given by eq. (5.5). The center of the highly wettable circle is chosen to be equal to the center of the domain, while $x_A/L_x = 0.2$, $ls/L_x = 0.02$ and $L_x = 3/2L_y$.

it will be employed to prohibit the sliding movement of the droplet down the incline. To achieve this, the driving force down the incline has to be balanced by the appropriate wettability gradient strength.
A simulation was performed using the wettability profile given by eq. (5.5) with $\rho_{\text{HW}} = -1$, $\rho_{\text{LW}} = 1$, $ls = 0.1$, $x_A = 5$ and a domain with $\alpha = 65°$, $L_x \times L_y = 30 \times 15$. Snapshots of this simulation are displayed in fig. 5.8. The positions of the wettability profiles points of steepest slope, i. e., where $s(\mathbf{x}) = x_A$ are marked by a dotted black line. As the initial condition, the parabolic droplet given by eq. (3.10) with $h_0 = 1.6$, placed at the centre of the domain, was chosen. The initial state is displayed in fig. 5.8 a). Due to the high wettability at the centre of the wettability spot, the droplet spreads out while at the same time following the driving force down the incline. Once the droplet reaches the transition region at the right side of the wettability profile, it experiences the force resulting from the wettability gradient. Since the wettability in the transition region decreases for increasing values of x, the resulting force acts towards smaller x-values, i. e., opposite to the driving force. In the case presented in fig. 5.8 the driving force is smaller than the force resulting from the wettability gradient. Thus, the droplet remains within the highly wettable spot and assumes the equilibrium state portrayed in fig. 5.8 b). The droplet, therefore, is pinned by the applied wettability profile. One can observe a deformed droplet covering the right half of the highly wettable spot. While most mass is contained within the highly wettable area, a small fraction is spread beyond the marked transition region towards larger x values.
Increasing the droplets volume leads to an increased driving force (cf.

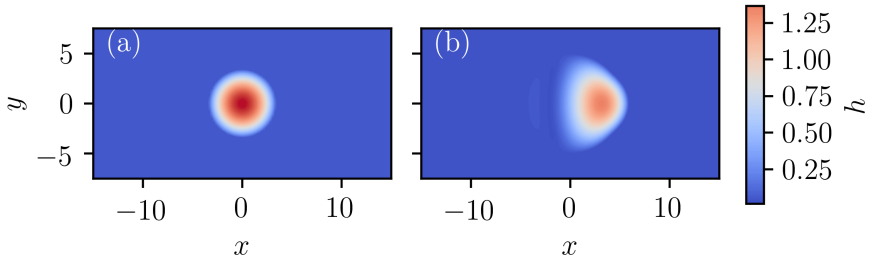

Figure 5.8: Snapshots obtained during the numerical simulation of a liquid droplet on a heterogeneous, inclined substrate. The initial droplet height is chosen to be $h_0 = 1.6$ and the inclination angle of the substrate as $\alpha = 65°$. The wettability profile applied is given by eq. (5.5) with $\rho_{HW} = -1$, $\rho_{LW} = 1$, $x_A = 5$, $ls = 0.1$. The points of steepest slope, i. e., $s(\mathbf{x}) = x_A$ are marked by a dotted black line. a) shows the initial state, whereas b) portrays the equilibrium state of a droplet pinned by the wettability spot.

eq. (2.1)). The force resulting from the wettability pattern undergoes only minor changes due to the altered droplet shape. Choosing a sufficiently large volume, therefore, leads to the depinning of the droplet.
Pictures of the height profile during the simulation of a droplet with the initial height $h_0 = 1.6825$ are shown in fig. 5.9. For the performed simulation, all parameters, except the initial droplet height, are chosen the same as for fig. 5.8. The initial state is portrayed in fig. 5.9 a). As the droplet has adapted to the inclination and high wettability of the spot, it assumes an asymmetrical shape and moves towards the border of the highly wettable spot. Once it has reached the border and experiences the wettability gradient, the dynamics slow down significantly. During this slow evolution the state shown in fig. 5.9 occurs, which is similar to the equilibrium state of a droplet with $h_0 = 1.6$, shown in fig. 5.8 b). For the film height employed here, however, the droplet does not assume its equilibrium shape but can gradually move over the wettability gradient, thus, forming a droplet outside the highly wettable spot. This state is displayed in fig. 5.9 c). After enough mass has accumulated outside of the spot, the droplet pinches off from the liquid, still contained by the wettability gradient. The driving force, therefore, exceeds the surface tension holding the liquid structure together. The depinned droplet and the small volume of remaining liquid are shown in fig. 5.9 d). Note that due to periodic boundary conditions being in place, the dynamics exhibited by the liquid show a cyclic behaviour. The depinned droplet can freely move down the incline until it reaches the highly wettable spot again. After it enters the spot, it spreads out and slows down once the right side of the wettability gradient has been reached. It deforms into the shape presented in fig. 5.9 b), and the dynamics repeat themselves.
A parameter useful for illustrating this repeating pattern is the position of the maximum film height x_{max}. Here only the position along

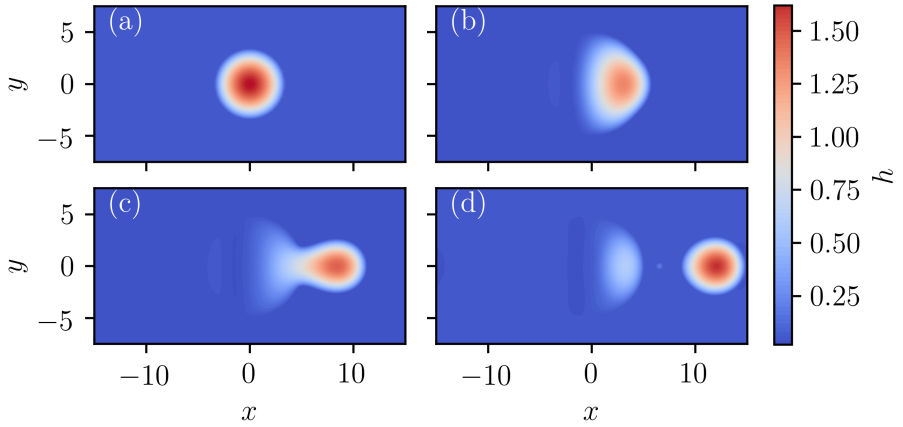

Figure 5.9: Snapshots obtained during the numerical simulation of a liquid droplet on an inhomogeneous inclined substrate. The initial droplet height was chosen as $h_0 = 1.6825$, while all other parameters are equal to those given in the caption of fig. 5.8. a) shows the initial state of a paraboloid droplet at the centre of a highly wettable spot. The droplet reaches the transition region in b). Most mass can penetrate the wettability gradient, which leads to the formation of a droplet outside the highly wettable area while some of the liquid remains within. c) and d) show the liquid's height profile before and after the droplet has disconnected from the liquid within the spot, respectively.

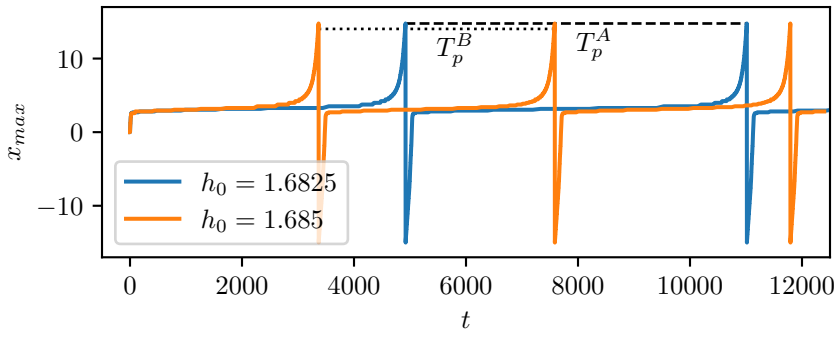

Figure 5.10: Position of the liquid film heights maximum along the x-direction $x_{\max}$, displayed as a function of the simulation time t. The displayed results were obtained during the simulation shown in fig. 5.9 as well as during an analogous simulation using a droplet with the initial height $h_0 = 1.685$. Dashed and dotted lines illustrate the periods denoted as T_p^A and T_p^B for $h_0 = 1.6825$ and $h_0 = 1.685$, respectively. They are obtained by measuring the distance between the local maxima of $x_{\max}$. These local maxima correspond to the droplets reaching the right domain boundary.

the x-axis is relevant since, due to the lack of forces acting parallel to the y-axis, the maximum does not move along the y-direction.
Figure 5.10 shows the temporal evolution of $x_{\max}$ for the droplet displayed in fig. 5.9, i. e., $h_0 = 1.6825$ as well as for a droplet with $h_0 = 1.685$. During the initial times, the behaviour of both droplets is identical, as in both cases the initially placed droplet needs to adapt to the inclined and heterogeneous substrate. As discussed for $h_0 = 1.6825$ the droplets spread out on the highly wettable area and move down the incline until they encounter the wettability gradient, resulting in a slowed-down movement (cf. fig. 5.9 b)). One can observe these periods of slow movement in fig. 5.10 as almost horizontal lines, which significantly differ in length for the two used initial heights. After some time, the liquid slowly crosses the gradient and the velocity increases, leading to an increase of $x_{\max}$. Due to the increasing mass of the droplet outside of the wettability spot (cf. fig. 5.9 c)) the velocity increases, leading to a non-linear increase of $x_{\max}$ until the droplet has completely depinned, after which a linear behaviour can be observed. Due to the periodic boundary conditions, the position of maximum liquid height jumps from $x_{\max} = L_x/2$ to $x_{\max} = -L_x/2$, and keeps increasing linearly. Once the droplet again experiences the wettability gradient, the velocity slightly increases until the right boundary of the spot has been reached. Now the dynamics slow down again, and the behaviour repeats itself.
From the times at which $x_{\max} = L_x/2$ holds, the periods T_p for the different heights can be determined. For the droplet with $h_0 = 1.6825$ this results in $T_p^A = 5684$ while for the slightly larger droplet, with an initial height roughly 0.15% larger, one obtains $T_p^B = 4212$. The large difference in the periods is caused by the proximity of the initial film height to the critical value. For an initial film height of $h_0 = 1.68$, a stable pinned droplet is obtained. Thus, the forces acting on the droplet at the boundary of the wettability spot are almost balanced, resulting in slow dynamics.
Until now, the employed inclination angle was kept at $\alpha = 65°$. In order to get a better understanding of the inclination angle's influence as well as the interaction with the initial film height, i. e., the volume, a parameter scan of the initial film height h_0 and the inclination angle α was performed. For each parameter set a simulation analogous to figs. 5.8 and 5.9 was carried out. In order to efficiently determine whether or not the wettability profile pins the droplet, a maximum of 300 timesteps were performed. During the simulations, the adaptively chosen time-stepping size dt was monitored. Once it crossed the threshold value of $dt = 10^5$, the simulation was terminated since it can be assumed that such time steps only occur for stable states, i. e., pinned droplets. If all 300 timesteps are performed without the simulation's termination, the parameter set is assumed to result in a depinned droplet.

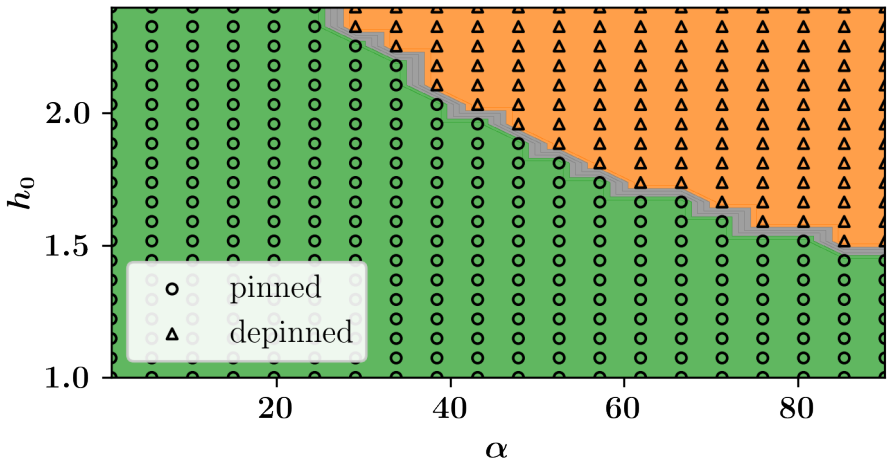

Figure 5.11: Investigation of droplet pinning using an α and h_0 parameter scan for a wettability profile given by eq. (5.5) with $\rho_{HW} = -1$, $\rho_{LW} = 1$, $ls = 0.1$, $x_A = 5$. The domain size was chosen as $L_x \times L_y = 30 \times 15$ and a paraboloid droplet given by eq. (4.1) was chosen as the initial condition. Each marker corresponds to an investigated parameter set. The circular markers and green background indicate a stable pinned droplet, while the triangles and orange background mark a depinned droplet sliding down the incline. The grey area is used to mark the area where the lack of simulations does not allow conclusions about the stability of the droplet.

An illustration of the obtained results for the wettability pattern used in figs. 5.8 and 5.9 is displayed in fig. 5.11. The background colours as well as the symbols indicate whether a pinned droplet (cf. fig. 5.8), marked in green with circles or a depinned droplet (cf. fig. 5.9), indicated by the orange background and triangles, is obtained. The transition region is marked as a grey background. Note that due to the resolution of the employed parameter scan, no conclusion about the equilibrium position of the droplets within this region can be made.
One can see that both the initial film height, as well as the inclination angle have a significant influence on the depinning of the droplets. For small inclination angles (initial film heights), no initial film height (inclination angle) could be determined for which a depinning occurs. The form of the critical region suggests that this behaviour continues beyond the investigated parameter region. Especially for small film heights in the order of $h_0 \approx 1$, the stable pinned droplet region extends further towards large inclination angles.
An analogous investigation using a more shallow wettability profile, i. e., with $\rho_{HW} = -0.5$ and $\rho_{LW} = 0.5$ was performed to obtain the results shown in fig. 5.12. The investigated parameters were varied in the same range as it was done for fig. 5.11. However, since a smaller wettability gradient was employed, the area of a stable/pinned droplet is greatly reduced. The general form of the plot nevertheless remains

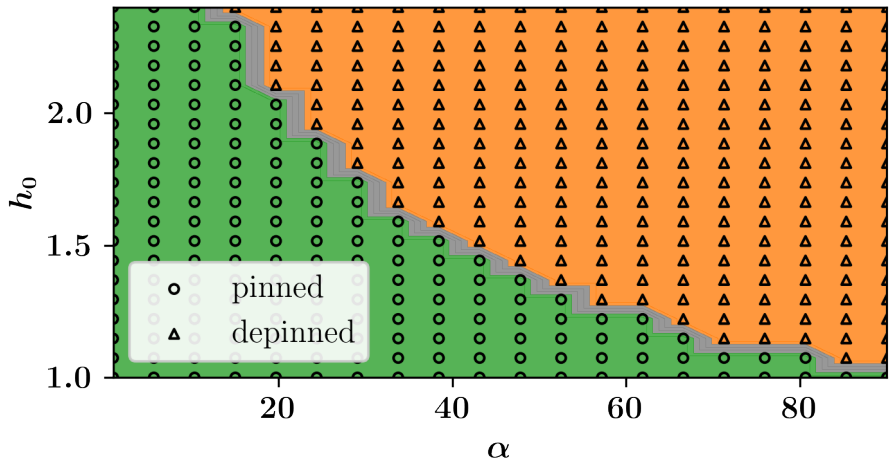

Figure 5.12: Results of a droplet pinning investigation using an α and h_0 parameter scan equivalent to fig. 5.11 except for the employed wettability parameters $\rho_{HW} = -0.5$, $\rho_{LW} = 0.5$. All displayed attributes retain their meaning from fig. 5.11.

the same. For small inclination angles, i. e., $\alpha < 15°$, the area of stability still extends beyond the considered parameter region for the initial height h_0, whereas for small initial film heights h_0, the area of stability only extends beyond the maximum inclination angle for $h_0 = 1$ while all other values lead to unstable droplets.

5.2.3 *Switchable Wettability Profile*

While a temporally constant wettability pattern was employed in section 5.2.2, this section will include an additional time dependence. In section 5.2.3.1 instantaneous switches of the wettability parameters ρ_{HW} and ρ_{LW} will be considered, as it was done in section 4.2. Section 5.2.3.2 will consider a moving wettability profile analogous to chapter 3 and section 4.1.

5.2.3.1 *Stationary Switchable Wettability Profile*

The employed wettability profile remains the same as in section 5.2.2, as does the domain size. The used wettability value sets are $\rho_{HW} = -1$, $\rho_{LW} = 1$, denoted in the following as S1 and $\rho_{HW} = \rho_{LW} = 1$, i. e., a homogeneous substrate with $\omega(\mathbf{x}, t) = 1$, denoted as S2. While for S1 pinning *can* occur depending on the inclination angle and initial height of the droplet (c.f. fig. 5.11), the homogeneous substrate S2 will inevitably lead to a sliding droplet as soon as $\alpha \neq 0$ [13].
In the following, the switching of the wettability parameters will be investigated as a method to induce periodic pinning (depinning). For this, h_0 will be chosen such that the resulting droplet is pinned by

S1. A switch to S2 will result in a sliding movement of the droplet down the incline. Switching back to S1 before the droplet has left the region of the wettability gradient can induce an uphill movement of the droplet and result again in a pinned state. For this behaviour to occur, the switching times must be chosen short enough for the droplet to experience the wettability gradient once S2 is switched to S1. Simultaneously the wettability gradient must be chosen strong enough to outweigh the driving force down the incline. During the following investigations only the influence of the switching times will be considered.

To investigate the periodic pinning of droplets, a paraboloid droplet with $h_0 = 1.6$ is placed at the center of a substrate equivalent to the one used for fig. 5.8. The initial height is chosen to ensure the existence of a stable, pinned state on S1 (c.f. fig. 5.11). After the droplet has adapted to the substrate fig. 5.13 a) is obtained. Here the droplet has assumed its equilibrium pinned shape, equal to the state shown in fig. 5.8 b). After the equilibrium state is assumed, the substrate is switched to S2, resulting in the state shown in fig. 5.13 c). Here the droplet has not yet adapted to the newly employed S2. Due to the homogeneous substrate, the droplet starts to slide down the incline and assumes an almost spherical cap shape. Before the substrate is switched back to S1 the state displayed in fig. 5.13 d) is obtained, while the state shortly after the switch is shown in fig. 5.13 e). At the time of switching, the droplet's left part is inside the wettability spot and starts to spread out due to the highly wettable substrate. The right part, on the other hand, continues to move down the incline. Over time more liquid accumulates outside of the wettability spot. This leads to a formation of a droplet outside of the spot, connected to the liquid within through a thin liquid bridge shown in fig. 5.13 e). The formed droplet continues moving down the incline, leading to a pinch off. Thus, the droplet can freely move down the incline with an almost spherical cap shape. Additionally, a small amount of liquid is left behind within the wettability spot, similar to the depinning process observed in fig. 5.9. The corresponding state is displayed in fig. 5.13 f).

Increasing the switching time further leads to an increased distance between the droplet's position at the time of switching from S2 to S1 and the centre of the wettability profile. For switching times that lead to the droplet still experiencing the wettability gradient at the time of switching S2$\rightarrow$ S1, the time it takes for the pinch-off to take place decreases. For even larger switching times, the droplet does not experience the heterogeneity and thus continuous moving down the incline uninhibited by the switch.

If the switching time is decreased, a more significant fraction of the liquid's volume is present within the highly wettable spot once the substrate is switched back to S1. Since less liquid has crossed the

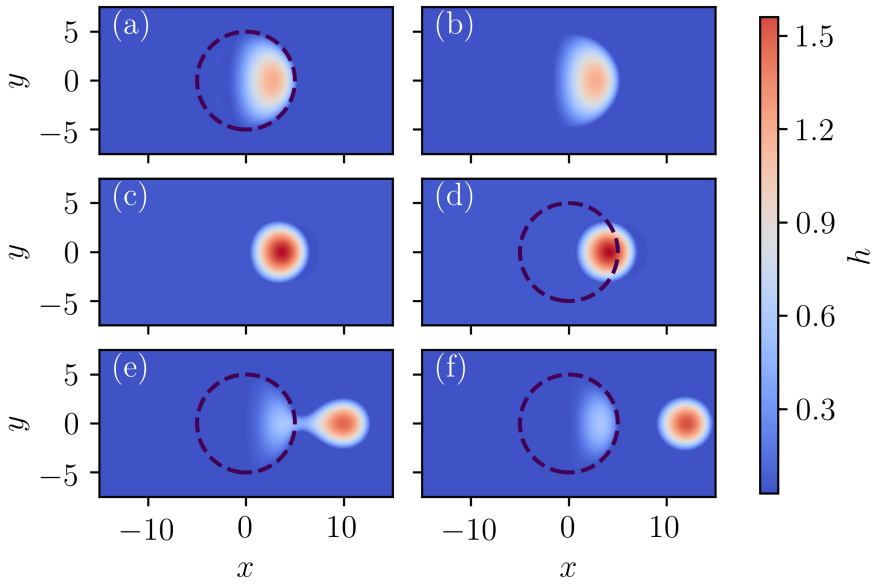

Figure 5.13: Snapshots obtained during the S1→ S2→ S1 switching. The time for which S2 was applied was chosen as $T_{S_2} = 17.9$. a) shows the pinned state of a droplet with $h_0 = 1.6$ on S1, i. e., a heterogeneous substrate with the wettability pattern equal to the one employed for fig. 5.8. Shortly after S2, i. e., the homogeneous substrate with $\omega(\mathbf{x}, t) = 1$, was employed, the state displayed in b) was obtained. Here the droplet has not yet adapted to the substrate. c) shows the droplet shortly before switching the wettability pattern back to S1. It has moved down the incline and exhibits an almost spherical cap shape. d) shows the state shortly after the pattern is switched back to S1. The left part of the droplet is starting to move back into the wettability spot while the right part remains outside. In e), most of the liquid has left the wettability spot and accumulated in a droplet connected to the liquid remaining in the spot through a narrow liquid bridge. In f), the droplet has pinched off and moves down in a shape analogous to c) while a small part of the liquid remains within the highly wettable spot.

wettability gradient, no droplet forms outside the spot and all of the liquid retracts back into the spot, leading again to a pinned state.
Decreasing the switching time to $T_{S_2} = 17$ results in the droplet being able to move back up into the highly wettable spot and assume the pinned state again. Once the droplet has reached the pinned state, the switching can be repeated with an identical outcome. One can, therefore, induce a periodic behaviour of the liquid if the time T_{S_1}, for which S1 is employed, is chosen correctly. For $T_{S_1} = 383$ and $T_{S_2} = 17$ one is able to obtain this kind of periodic behavior. The switching pattern for ρ_{HW} during a simulation, employing these switching times, is shown in the upper panel of fig. 5.14. Since $\rho_{LW} = 1$ is employed during the entire simulation, $\rho_{HW} = 1$ corresponds to a homogeneous and $\rho_{HW} = -1$ to a heterogeneous substrate, where the heterogeneity is equivalent to the one used in fig. 5.13. Within the upper panel of fig. 5.14, the states shortly after the switch S1→S2 and S2 → S1 are indicated with orange and green dots, respectively. Due to the periodicity of the switching pattern, all states marked are identical to their equally coloured counterparts. One of the states after the S1→ S2 switch is displayed in fig. 5.14 a). The droplet has not yet adapted to the homogeneous substrate and, thus, still has the form induced by the highly wettable spot. On the homogeneous substrate, the droplet assumes an almost spherical cap shape as it slides down the incline. At the time of switching from S2 to S1, most of the liquid is still present within the spot (c.f. fig. 5.14 b)). Comparing the state shortly after the S2→S1 switch, to the corresponding state for $T_{S_2} = 17.9$, displayed in fig. 5.13 d), a slight difference is visible. Due to the shorter switching time of $T_{S_2} = 17$, the droplet in fig. 5.14 b) has not yet progressed as far down the incline as it is the case for $T_{S_2} = 17.9$. The liquid will, therefore, not form a droplet outside of the domain, as it occurred in fig. 5.13 e), but rather completely move up the incline into the highly wettable spot. After $T_{S_1} = 383$, the droplet has again assumed the pinned state (c.f. fig. 5.13 a)). Once the pinned state is obtained, the switching pattern is repeated, leading to identical states.
As shown in the upper panel of fig. 5.14 T_{S_1} was chosen larger than T_{S_2}. This was done to ensure the droplet's return to the pinned state before the next switch to S2. If T_{S_1} is decreased, the droplet may not have returned to the pinned state and, therefore, be positioned further down the incline once the substrate is switched to S2, resulting in a behaviour analogous to fig. 5.13. The droplet cannot return to the pinned state but rather separates into a small part of liquid contained by the highly wettable spot and a droplet moving down the homogeneous region of the substrate.
In order to determine the correct value for T_{S_1} one may perform a single switching period, i. e., a S1→S2→S1 switch for a chosen value of T_{S_2}. The simulation is continued until the pinned droplet is obtained. From the simulation results, the necessary switching time T_{S_1} can be

determined as the time after the S2→S1 switch required for the point of maximum height to return to the value corresponding to a pinned droplet.
For different droplet heights, both switching times T_{S_1} and T_{S_2} have to be adapted since, e. g. an increase of the initial height results in an increased droplet speed and, thus, a faster movement away from the wettability gradient. At the same time, however, the increased film height results in a larger base area of the droplet. Thus, the droplet can move down the incline further while still experiencing the wettability spot after the S2→S1 switch. The switching time T_1 was determined for $h_0 = 1.6$ as well as for $h_0 = 1.55$, using the method described in the beginning of this section. For the larger liquid volume, the switching time $T_{S_2} = 17.6$ was obtained, whereas the investigation of the smaller droplet resulted in $T_{S_2} = 25.8$. For the considered liquid heights, the switching time T_{S_2} increases with decreasing initial film height. Thus the increase of the velocity outweighs the increased base area. However, a more thorough investigation should be performed to determine the behaviour for a larger range of film heights.
To determine the appropriate switching times for various initial film heights h_0, one can start with a large initial film height and determine the critical switching time, as described at the beginning of this section. Since the switching times increase for decreasing film heights, investigating the initial film height in decreasing order, one can use the result obtained from the previous h_0 as the starting point for the following film height. This way, the computational costs can be minimised[1].

5.2.3.2 *Moving Wettability Profile*

Analogous to the wettability profiles considered in chapter 3 and section 4.1, a velocity can be introduced into eq. (5.5), resulting in a moving wettability pattern. The resulting moving wettability pattern is again given by eq. (5.5) with an adapted definition of the parameter s

$$s(\tilde{\mathbf{x}}) = \sqrt{(\tilde{x})^2 + (\tilde{y})^2}. \tag{5.7}$$

Here $\tilde{x}$, $\tilde{y}$ denote the values of x and y shifted by the velocity times the time $v_{\text{inhom}}t$ with an additional remapping to include the periodic boundary conditions. This coordinate transformation is again given by eq. (3.4) adapted to the two dimensional substrate such that x corresponds to x (y), c to c_x (c_y) and L to L_x (L_y).
The pattern can analogously to chapter 3 and section 4.1 be used as a method to induce a desired liquid movement. While in the case of a horizontal substrate, the droplet remained stationary without applying

1 This method only works under the assumption that the change of driving force has a larger impact on the dynamics than the increase of the base area for all film heights.

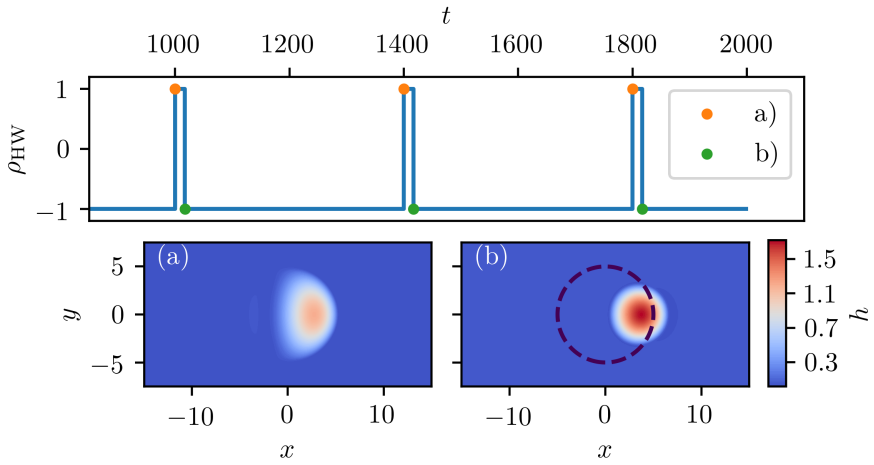

Figure 5.14: The upper panel displays the value of ρ_{HW} during a simulation, where a wettability profile analogous to fig. 5.13 with instantaneous switches between $\rho_{HW} = \pm 1$ was applied. The orange points mark the states immediately after switching to the homogeneous substrate S2. The height profile of this state is portrayed in panel a). The green dots indicate the states immediately after switching back to the heterogeneous substrate S1. The corresponding height profile is displayed in panel b).

a (moving) wettability profile, the liquid on a homogeneous inclined substrate inevitably starts moving. As discussed in section 5.2.2, stationary wettability patterns may be applied to inhibit any movement of the liquid, resulting in an equilibrium pinned state. Using the *moving* wettability profile, however, the movement of the droplet can be altered. Examples include slowing down, or speeding up, the droplet's decline by applying a wettability profile with a velocity smaller, or larger than the velocity of the droplet on an analogous homogeneous substrate. For the slowed movement, the limiting case is the pinned droplet discussed in section 5.2.2, as it corresponds to a completely halted droplet movement. Thus, using the wettability parameters leading to a pinned state, one can arbitrarily slow the liquid's movement down the incline. The parameters for the pinned states shown in figs. 5.11 and 5.12 may, therefore, be used as a starting point for the determination of wettability parameters suitable to induce the desired speed reductions.

Choosing the parameters used in fig. 5.8 the droplets velocity can be set by the speed of the inhomogeneity profile v_{inhom}, as long as the droplet's sliding speed on a homogeneous, equally inclined substrate is larger than v_{inhom} and $v_{inhom} \geq 0$. This was done for fig. 5.15. The upper panel displays a time series of the point's of maximum height position along the x-axis x_{max} during the simulation of a droplet on a homogeneous substrate (blue), with $\omega(\mathbf{x}, t) = 1$, as well as, for the wettability profile given by eq. (5.5), with the same parameters as for fig. 5.8 and $v_{inhom} = 0.05$ (orange). Both substrates are inclined

by $\alpha = 65°$. While the liquid's initial adaption to the inclined substrate causes both curves to overlap for small simulation times t, a clear divergence of both curves can be observed for larger times. Both graphs show a linear increase, as is to be expected from a constant driving force. The curve for the droplet on the heterogeneous substrate exhibits a significantly smaller inclination than the curve for the droplet on a homogeneous substrate. The bottom panels of fig. 5.15 display two states obtained during the simulation of the heterogeneous substrate. Their corresponding positions in the upper panel are marked and labelled according to the panel labels. While fig. 5.15 a) was obtained during the initial adaption process of the droplet to the inclined substrate, b) corresponds to the equilibrium state of the advected droplet, moving at constant speed and shape. Measuring the steepness of the curve after the initial adaption process, i. e., for $t > 100$, one can confirm that the droplet's velocity matches the inhomogeneity speed $v_{\text{drop}} = v_{\text{inhom}} = 0.05$.

By decreasing the speed of the inhomogeneity further while keeping all other parameters constant, one can obtain arbitrarily slowed-down droplet velocities. If the speed of the profile is reduced to negative values, an uphill movement of the liquid may be induced. For this to occur, the force acting on the droplet due to the wettability gradient not only has to match the driving force, as was the case for pinned droplets (c.f. section 5.2.2), but rather has to exceed it. The droplet velocities obtainable for an uphill movement are, therefore, greatly reduced compared to the downward velocities. Note that this process is similar to the experimental realization in [6], where a constant wettability gradient covering the entire substrate was employed to induce an uphill movement. Using a moving wettability gradient has the advantage that the advection may be extended to arbitrary substrate lengths while exposing the droplet to a constant wettability strength. The upwards movement will not be investigated further here. Instead, in the following, the acceleration of a downward movement will be discussed.

A speed-up of the droplet's movement down the incline can be induced by choosing the velocity of the profile larger than the droplet's speed on the homogeneous substrate. Here the pinned state discussed in section 5.2.2 can no longer be considered the limiting case. Analogous to chapter 3, the speed obtainable depends strongly on the used parameters of the wettability profile, the height of the droplet and additionally the inclination angle. The general influence observed for the different parameters in chapter 3 can be extended to the moving wettability pattern on an inclined substrate, i. e., the largest droplet velocities can be obtained by using a strong wettability gradient while for too large velocities of the profile the liquid will be left behind. Note that the influence of the initial height h_0 on the maximum droplet speed is distinct from section 3.4.2, as the application of the moving

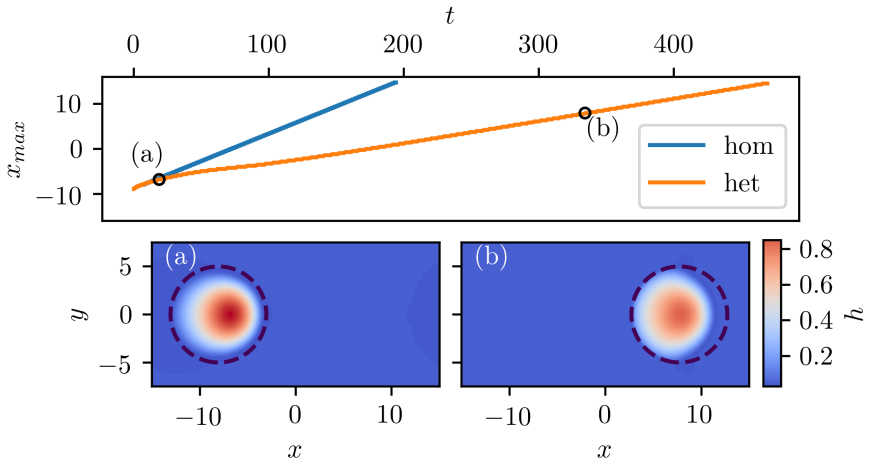

Figure 5.15: Shown in the upper panel is the x-coordinate of the position of maximum height for different times during the simulation of a liquid droplet with $h_0 = 1.6$ on a homogeneous substrate with $\omega(\mathbf{x}, t) = 1$ (blue) and on a moving wettability spot given by eq. (5.5) with $\rho_{\mathrm{HW}} = -1$, $\rho_{\mathrm{LW}} = 1.0$, $ls = 0.1$, $x_A = 5.0$ and $v_{\mathrm{inhom}} = 0.05$ (orange). The bottom panels show two states obtained for the droplet on the heterogeneous substrate. a) was obtained during the droplets adaption process to the heterogeneous, inclined substrate, whereas b) constitutes the equilibrium state of the droplet moving at a constant speed.

wettability profile only *alters* the sliding velocity of the droplet, while the sliding velocity itself strongly depends on the film height (c.f. eq. (2.1)).

The distance of the point of maximum height to the centre of the wettability profile along the x-axis for two different wettability speeds is displayed in the upper panel of fig. 5.16. The distance, or droplet lead as it was denoted in section 3.3, was calculated using the definition given in eq. (3.12), where L has to be replaced by L_x. The distance along the y-axis remains zero during the simulation as the droplet is not exposed to any forces acting parallel to the y-direction. The wettability parameters employed are the same as for fig. 5.15 except for the velocities of the profiles which were chosen as $v_{\mathrm{inhom}} = 0.17$ and $v_{\mathrm{inhom}} = 0.19$ plotted in orange and blue, respectively. Four states obtained during the simulations are portrayed in panel a) - d) of fig. 5.16. Their corresponding points in the upper panel are marked by colour-coded circles and additional labels indicating the associated panels. The states displayed in a) and b) were obtained during the initial times of the simulations using $v_{\mathrm{inhom}} = 0.19$ and $v_{\mathrm{inhom}} = 0.17$, respectively. Both droplets are entirely contained by the moving wettability profile and, due to the wettability profile being faster than the freely moving droplet, are concentrated at the left side of the moving wettability profile. For increasing times, one can observe in the upper panel of fig. 5.16 that both droplets increase their distance

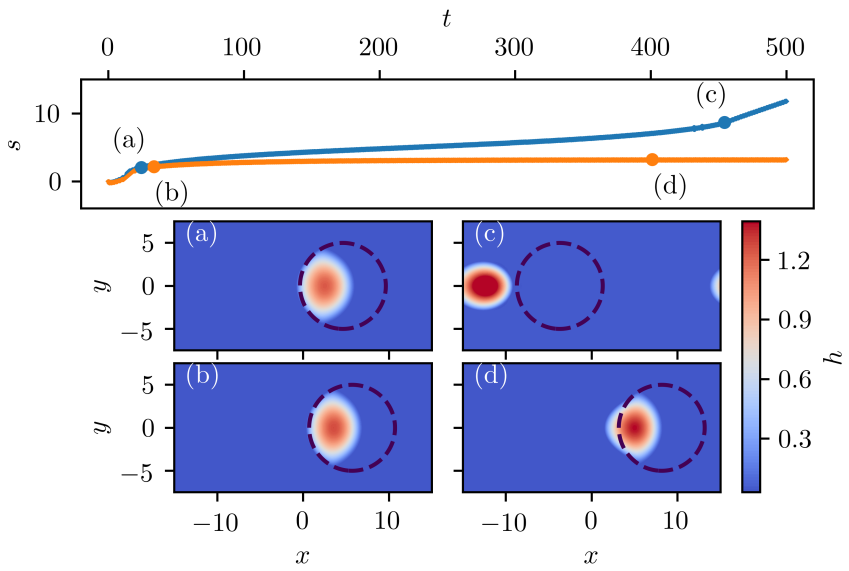

Figure 5.16: The upper panel shows the distance s along the x-direction between the point of maximum height and the centre of the wettability spot given by eq. (3.12). The two curves correspond to droplets with $h_0 = 1.6$ on a moving wettability profile analogous to the one used in fig. 5.15 with the velocities $v_{\text{inhom}} = 0.19$ (blue) and $v_{\text{inhom}} = 0.17$ (orange). The bottom panels display states obtained during the two simulations, here panel a) and c) correspond to $v_{\text{inhom}} = 0.19$ while the panel b) and d) were obtained for $v_{\text{inhom}} = 0.17$. The points in the upper panel corresponding to the displayed states are marked by dots and colour coded according to the used velocities.

to the centre of the inhomogeneity. For $v_{\text{inhom}} = 0.17$, similar to the behavior observed in section 3.3, this process stops once an equilibrium distance of $s \approx 3.2$ has been reached. The droplet continues to move down the incline with constant shape and distance to the profile, i. e., at a constant velocity $v_{\text{drop}} = v_{\text{inhom}}$. This behaviour results in a horizontal line in the upper panel of fig. 5.16. The corresponding state is displayed in fig. 5.16 d). For $v_{\text{inhom}} = 0.19$, the distance continues to increase, leading to the droplet slowly leaving the highly wettable spot. A snapshot of the droplet leaving the heterogeneity and thus ceasing to experience the wettability gradient is displayed in c). It results in a sudden change of the steepness of the corresponding curve in the upper panel since the velocity of the droplet reduces to the value on a homogeneous substrate with $\omega(\mathbf{x}, t) = 1$ while the wettability profile continuous moving at $v_{\text{inhom}} = 0.19$. Both of these dynamics were already observed for the horizontal substrate in chapter 3 and section 4.1.

The previously discussed method of slowing down or speeding up the liquid's decline can be employed as a control mechanism for droplets

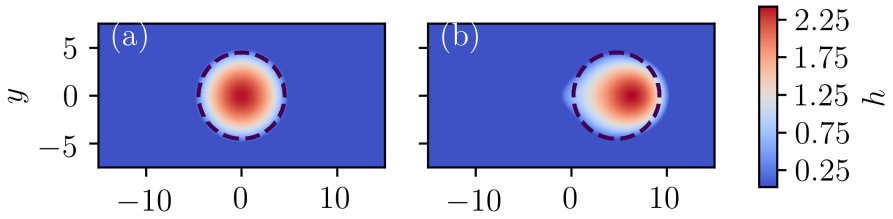

Figure 5.17: Snapshots obtained during the numerical simulation of a liquid droplet with $h_0 = 2.4$ on an inclined substrate with $\alpha = 65°$ and a moving wettability profile given by eq. (5.5) with $v_{\text{inhom}} = 0.212$, $\rho_{\text{HW}} = -1.0$, $\rho_{\text{LW}} = 1.0$, $ls = 0.1$ and $x_A = 4.5$. a) shows the initial state, i. e., at $t = 0$, whereas in b) the liquid's state at $t = 305$, i. e., after the droplet has crossed its initial position for the second time, is displayed. Panel b) corresponds to the equilibrium height form of the droplet.

exhibiting a pearling instability. While for the prevention of a pearling instability, the droplets need to be slowed down also, the induction of an instability is possible by increasing the velocity of a droplet below the critical volume.

Using a droplet given by eq. (4.1) with $h_0 = 2.4$ on a homogeneous substrate with the inclination angle $\alpha = 65°$ results in a pearling instability, as discussed in section 5.1. The speed of the point of maximum height during the beginning of the simulation, i. e., before the emission of the first satellite droplet, is approximately equal to $v_{\text{drop}} \approx 0.23$. Using a moving wettability profile with $v_{\text{inhom}} = 0.212$, $\rho_{\text{HW}} = -1.0$, $\rho_{\text{LW}} = 1.0$, $ls = 0.1$ and $x_A = 4.5$ results in the states shown in fig. 5.17. Here a) corresponds to the initial state of the liquid. The dashed black line marks the points of maximum steepness of the wettability profile. The droplet adapts to the inclined substrate and the wettability profile while at the same time being advected down the incline. Due to the employed wettability pattern, the form of the droplet is restricted. Simultaneously the velocity of the droplet is reduced to the speed of the heterogeneity. Both of these effects result in a stabilisation of the liquid structure. Thus, the form of the droplet, after the initial adaption to the substrate, does not change throughout the integration. The equilibrium shape of the liquid is displayed in fig. 5.17 b). The portrayed state was obtained at $t = 305$, after the droplet crossed the domain for the second time. The time at which fig. 5.17 b) was obtained corresponds approximately to the time at which fig. 5.2 f) was obtained. Comparing the two states, it is apparent that the moving wettability was successfully employed to prevent the pearling instability.

Snapshots of a direct numerical simulation, where the moving wettability profile was employed to induce a pearling instability for a droplet with a volume below the critical one, are displayed in fig. 5.18. The droplet is advected by a moving wettability profile with the pa-

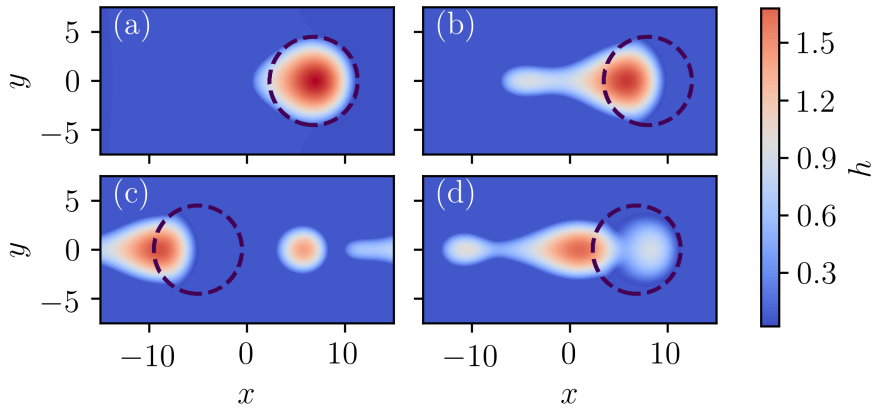

Figure 5.18: Snapshots obtained during the numerical simulation of a liquid droplet with $h_0 = 2.2$ on an inclined substrate with $\alpha = 65°$ being advected by a moving wettability profile given by eq. (5.5) with $v_{\text{inhom}} = 0.25$, $\rho_{\text{HW}} = -1.0$, $\rho_{\text{LW}} = 1.0$, $ls = 0.1$ and $x_A = 4.5$. a) shows the state shortly after the start of the simulation, where the droplet has formed a cusp. The cusp grows over time, leading to the formation of a pronounced tail, as shown in b). The droplet emits a satellite and continues to elongate, leading to the state shown in c). Due to the periodic boundary conditions, the emitted satellite droplet starts to experience the wettability spot and recombines with the main droplet, shown in d).

rameters given in the caption of fig. 5.18. At the beginning of the simulation, the liquid starts to form a cusp as shown in fig. 5.18 a). Analogous to the pearling instability on a homogeneous substrate discussed in section 5.1 liquid starts to accumulate in the cusp, leading to the formation of a tail. This state is displayed in fig. 5.18 b). Panel c) shows the state shortly after a droplet is emitted from the end of the tail and the elongation of the main droplet continuous. Due to the periodic boundary conditions, a cyclic behaviour occurs as the satellite droplets are absorbed by the main droplet again. Note that the position of maximum liquid height moves away from the centre of the wettability spot and for fig. 5.18 d) even lies outside of the spot. Therefore, the liquid is unable to keep up with the wettability structure and is ultimately left behind. However, if the wettability profile is applied for a sufficient time, a pearling instability can be induced for droplets below the critical volume by applying a moving wettability profile of appropriate strength and speed.

Since the maximum velocity of the droplet depends on the volume of the droplet itself, it is not possible to induce arbitrary droplet speeds. Thus, the droplet volume for which a pearling instability can be induced is limited.

In addition to the induction of a pearling instability, it is also possible to alter the exhibited instability. As discussed in section 5.1 and appendix B.2, the dynamics during the pearling instability depend on

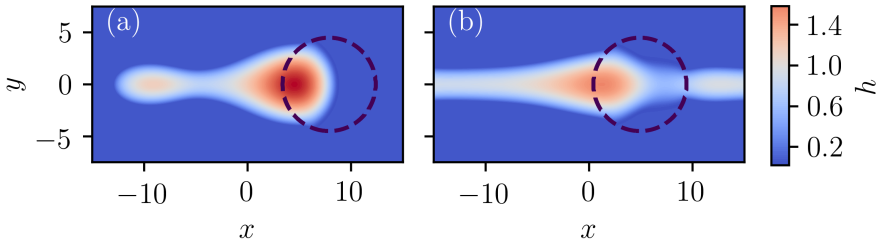

Figure 5.19: Snapshots obtained during the numerical simulation of a liquid droplet with $h_0 = 2.4$ on an inclined substrate with $\alpha = 65°$ being advected by a moving wettability profile given by eq. (5.5) with $v_{\text{inhom}} = 0.3$, $\rho_{\text{HW}} = -1.0$, $\rho_{\text{LW}} = 1.0$, $ls = 0.1$ and $x_A = 4.5$. a) shows the liquid's state after forming a pronounced tail. b) shows the equilibrium state, where the droplet has connected with itself and surface waves have formed.

the droplet's volume and the employed inclination angle. Different regimes were observed, which differ in the number of emitted satellites. Additionally, one regime, leading to the formation of surface waves was observed.

Snapshots of a simulation, where the moving wettability profile was used to induce the formation of surface waves for a droplet with an initial height $h_0 = 2.4$ are displayed in fig. 5.19. Note, that the dynamics on a homogeneous substrate are displayed in fig. 5.2.

Figure 5.19 a) shows the state of the liquid at $t = 126$, where a pronounced tail has formed. Due to the periodic boundary conditions, the liquid can connect with itself. After some time the structure takes on the shape displayed in fig. 5.19 b), which was obtained at $t = 1316$. This state corresponds to a surface wave. A similar state was also observed during the naturally occurring pearling instability in fig. B.7. In contrast to the homogeneous substrate, here, the wettability gradients at the boundaries of the spot result in a deformation of the liquid. For large simulation times, i. e., $t = \mathcal{O}(10^{13})$, the liquid retains the shape displayed in fig. 5.19 b). The maximum continues to move down the incline at the speed of the inhomogeneity .

The method presented here for controlling the pearling instability using moving wettability profiles may be used as a starting point to develop more reliant methods with a broader applicability, e. g. by tuning the employed parameters.

6 SUMMARY AND OUTLOOK

Within this thesis, the liquid dynamics on switchable, prestructured substrates were investigated numerically. For this, direct numerical simulations of the nonlinear thin-film equation [20, 46, 48] were performed using the finite element method implemented by the open-source library OOMPH-LIB [19]. The driver code employed during this thesis was developed in [40] and extended for this work.
The first part of this thesis focused on the investigation of horizontal substrates. For this, in chapter 3 initial considerations of a one-dimensional droplet on a substrate with a moving wettability profile were performed. Here, the switchable substrate was utilized as a method to advect the liquid droplet. Investigations of the maximum advection speed were performed, which showed that the speed depends on the employed wettability profile parameters and the liquid volume. During these investigations, it was shown that a proportionality obtained from the Cox-Voinov law [18] also holds for the model employed here.
An attempt was made to extend the one-dimensional results to a two-dimensional system in section 4.1. It was shown that the obtained one-dimensional results could be extended if one employs the appropriate initial condition, i. e., a two-dimensional ridge. The general dynamics, however, also remain similar for a two-dimensional droplet.
In section 4.2, the so-called Plateau-Rayleigh instability, a transversal instability exhibited by liquid ridges, was observed, and the applicability of switchable substrates as control mechanisms investigated. Here, switching patterns for the employed wettability profile were determined with which one can obtain locally stable versions of the meta-stable plateau states which exhibit themselves during the naturally occurring Plateau-Rayleigh instability. Since a positive real eigenvalue was obtained for the locally-stable states, direct numerical simulations of distorted versions of these states were performed. These showed that the obtained states truly are locally stable.
Chapter 5 considered the dynamics of a thin liquid film on an inclined substrate. The pearling instability was initially examined in section 5.1. Here, the expected behaviour could be observed and multiple regimes determined (c.f. appendix B.2). A substrate with a time-dependent inclination angle was employed as a second kind of switchable substrate. The influence of a temporally varying inclination angle on a liquid droplet exhibiting a pearling instability was analyzed in section 5.2.1. Here, a method could be determined to prevent a pearling instability for a sliding droplet while maintaining a large advection speed down

the incline.

As another control mechanism for liquid dynamics on an inclined substrate, switchable wettability patterns were employed. By using static heterogeneities of the wettability profile, droplets on the inclined substrate were pinned in section 5.2.2. Here, the influence of the employed inclination angle and liquid volume on the pinning capabilities of the substrate were investigated. Periodically pinned states could be obtained by performing periodic switches of the employed wettability profile in section 5.2.3.1. For an initially pinned droplet, the dynamics here correspond to periods of a sliding motion down the incline, which, by switching the wettability pattern, turns into an uphill movement until again the pinned state is obtained and the switching pattern can be started anew.

In section 5.2.3.2 moving wettability patterns were employed for liquid droplets on an inclined substrate. These profiles were used to decrease or increase the velocity of the liquid structures' movement down the incline. The previously obtained results for pinned droplets could be used as a limiting case for lowering the sliding velocity. This method was applied to liquid droplets in the context of a pearling instability. By speeding up the sliding movement, a pearling-like instability could be induced for droplets which otherwise would not exhibit this kind of instability. Analogously, decreasing the velocity of droplets exhibiting a pearling instability resulted in a stabilization of the droplet's shape and, thus, the prevention of a pearling instability

The focus of the investigations performed during this work was the manipulation and control of liquid dynamics through the application of switchable substrates. A variety of control mechanisms were employed, where most of these can and should be studied more thoroughly. Further investigations of the employed switching patterns should be attempted to broaden the range of applications and optimize the switching schemes presented here. For some of the investigated topics, e. g. pinned droplets, the application of continuation methods could simplify the investigations compared to the employed direct numerical simulations.

Part I

APPENDIX

A

NONDIMENSIONALISATION

During this thesis a nondimensionalised form of the thin-film equation is being employed. In the following, the process of performing this nondimensionalisation will be explained. An analogous nondimensionalisation was applied in [41, 49] for horizontal substrates.
The full form[1] of the dimensional thin-film equation is given by

$$\begin{aligned} \partial_t h &= \nabla \left[\frac{h^3}{3\eta} \nabla P(h, \mathbf{x}, t) + G\boldsymbol{\alpha} \right], \\ P(h, \mathbf{x}, t) &= -\gamma \Delta h - \left(\frac{B}{h^6} - \frac{A}{h^3} \right) (1 + \omega(\mathbf{x}, t)). \end{aligned} \tag{A.1}$$

Here η is the fluid's dynamic viscosity, γ the surface tension and A and B correspond to long- and short-range Hamaker-type constants, respectively [20, 32]. G is the gravitational constant, equal to the density of the liquid ρ times the gravitational acceleration g. One can arrive at equations for A and B by first determining the zero of the disjoining pressure, i. e., the minimum of the wetting potential (c.f. fig. 2.2). As mentioned in section 2.1 the minimum corresponds to the height of the precursorfilm h_p, for which one thereby obtains

$$h_p = \left(\frac{B}{A} \right)^{1/3}. \tag{A.2}$$

Secondly, one can use a relation between the equilibrium contact angle θ_{eq} and the wetting potential $f(h, \mathbf{x}, t)$ [49]

$$\theta_{eq} = \sqrt{\frac{-2f(h_p, \mathbf{x}, t)}{\gamma}}. \tag{A.3}$$

This relates to the disjoining pressure through eq. (2.8).
Using eq. (A.2), eq. (A.3) and eq. (2.8) for the wetting potential, the following expressions for A and B can be derived

$$A = \frac{5}{3}\gamma\theta_{eq}^2 h_p^2, \quad B = \frac{5}{3}\gamma\theta_{eq}^2 h_p^5. \tag{A.4}$$

The generalized pressure can therefore be expressed as

$$P(h, \mathbf{x}, t) = -\gamma\Delta h - \frac{5}{3}\gamma\theta_{eq}^2 h_p^2 \left(\frac{h_p^3}{h^6} - \frac{1}{h^3} \right) [1 + \omega(\mathbf{x}, t)]. \tag{A.5}$$

To perform the nondimensionalisation, scales need to be introduced

$$\mathbf{x} \to x_0 \tilde{\mathbf{x}}, \quad h \to h_0 \tilde{h}, \quad G \to G_0 \tilde{G}, \quad t \to t_0 \tilde{t}. \tag{A.6}$$

1 neglecting the hydrostatic pressure as in [12]

Applying these scales to eq. (A.1) leads to

$$\begin{aligned}
\frac{h_0}{t_0}\partial_t\tilde{h} &= \nabla\frac{1}{x_0}\left\{h_0^3\frac{\tilde{h}^3}{3\eta}\left[\nabla\frac{1}{x_0}P(\tilde{h},\tilde{\mathbf{x}},\tilde{t}) + G_0\tilde{G}\boldsymbol{\alpha}\right]\right\},\\
P(\tilde{h},\tilde{\mathbf{x}},\tilde{t}) &= -\gamma\frac{h_0}{x_0^2}\Delta\tilde{h} - \Pi(\tilde{h},\tilde{\mathbf{x}},\tilde{t}),\\
\Pi(\tilde{h},\tilde{\mathbf{x}},\tilde{t}) &= \frac{5}{3}\frac{\gamma\theta_{eq}^2\chi^2}{h_0}\left(\frac{h_p^3}{h_0^3\tilde{h}^6} - \frac{1}{\tilde{h}^3}\right)[1+\omega(\tilde{\mathbf{x}},t)].
\end{aligned} \tag{A.7}$$

Here the variable $\chi = \frac{h_p}{h_0}$ with the height of the precursor film h_p and the nondimensionalisation scale h_0 was introduced. Setting all prefactors, except the one contained in the disjoining pressure equal to one, results in the following set of equations

$$\begin{aligned}
\frac{\gamma h_0^3 t_0}{3\eta x_0^4} = 1,\ \frac{5}{9}\frac{\gamma h_0 t_0}{\eta x_0^2}\theta_{eq}^2\chi^2 &= \frac{5}{3}\theta_{eq}^2\chi^2,\\
\frac{h_0^3 t_0 G_0}{3\eta x_0^2} = 1,\ \frac{h_0^2 t_0 G_0}{3\eta x_0} &= 1.
\end{aligned} \tag{A.8}$$

These are fulfilled for the scales

$$x_0 = h_0,\ \ t_0 = \frac{3\eta h_0}{\gamma},\ \ G_0 = \frac{\gamma}{h_0^2}. \tag{A.9}$$

Employing these scales results in the non-dimensionalised form of the thin-film equation

$$\begin{aligned}
\partial_t h &= \nabla\left\{\, h^3\left[\,\nabla P(h,\mathbf{x},t) + G\boldsymbol{\alpha}\,\right]\right\}\\
P(h,\mathbf{x},t) &= -\Delta h - \frac{5}{3}\theta_{\mathrm{eq}}^2\chi^2\left(\frac{\chi^3}{h^6} - \frac{1}{h^3}\right)\left[1+\omega(\mathbf{x},t)\right].
\end{aligned} \tag{A.10}$$

A result of this scaling is that all spatial direction are scaled equally, i. e., the same scaling is applied in the plane of the substrate as well as for the film height orthogonal to the substrate's plane.
During this thesis, $h_0 = 1$ is employed and G is defined using the surface tension of water. The macroscopical equilibrium contact angle θ_{eq} is kept at $\theta_{eq} = \sqrt{5/3}$. Due to the modulation term $1+\omega(\mathbf{x},t)$, an effective equilibrium contact angle $\theta_{\mathrm{eq}}^{\mathrm{eff}}$ is determined by the parameter θ_{eq} as well as $\omega(\mathbf{x},t)$ [41]

$$\theta_{\mathrm{eq}}^{\mathrm{eff}} = \theta_{\mathrm{eq}}\sqrt{(1+\omega(\mathbf{x},t))}. \tag{A.11}$$

In the thesis references to the contact angle and the variable θ_{eq}, if not mentioned otherwise, refer to the effective contact angle.

B

ADDITIONAL RESULTS

B.1 EIGENFUNCTIONS OF THE STABILIZED STATES

This section includes several eigenfunctions determined for the stabilized versions of the meta-stable two bulges and ridge state. For both states, the expected varicose mode [20] could be observed. These are displayed in fig. B.1 a) and b) for the ridge and two bulges state, respectively. The remaining eigenfunctions for the two bulges include eigenfunctions corresponding to the movement of the liquid either along the wettability stripe, as shown in fig. 4.12 a), or orthogonal to it, as displayed in fig. 4.12 c). Additionally, the eigenmode displayed in fig. 4.12 b) was obtained, which corresponds to a formation of a liquid ridge. The eigenfunctions obtained for the ridge state resemble the formation of various numbers of bulges. Displayed in fig. B.3 are the eigenfunctions corresponding to the formation of one, three, and four bugles in panels a), b) and c), respectively.

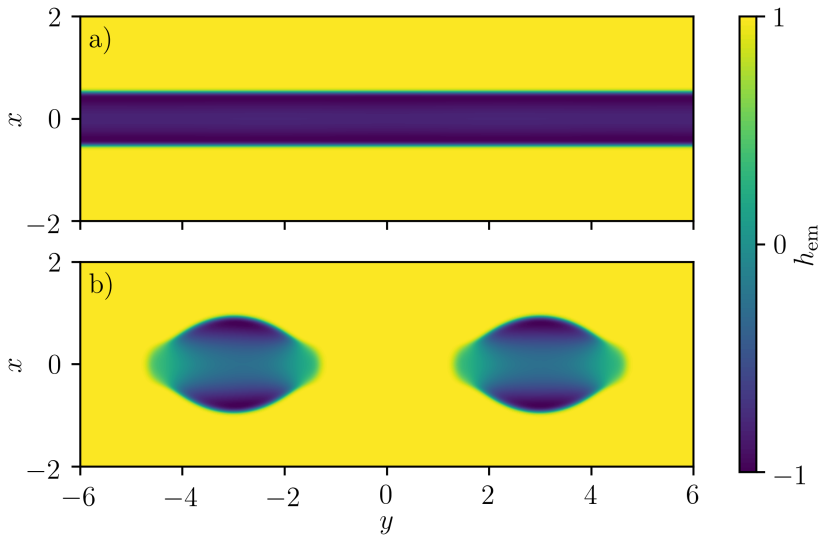

Figure B.1: a) and b) display the varicose eigenmodes of the stabilized ridge and two bulges state discussed in sections 4.2.2.1 and 4.2.2.2, respectively.

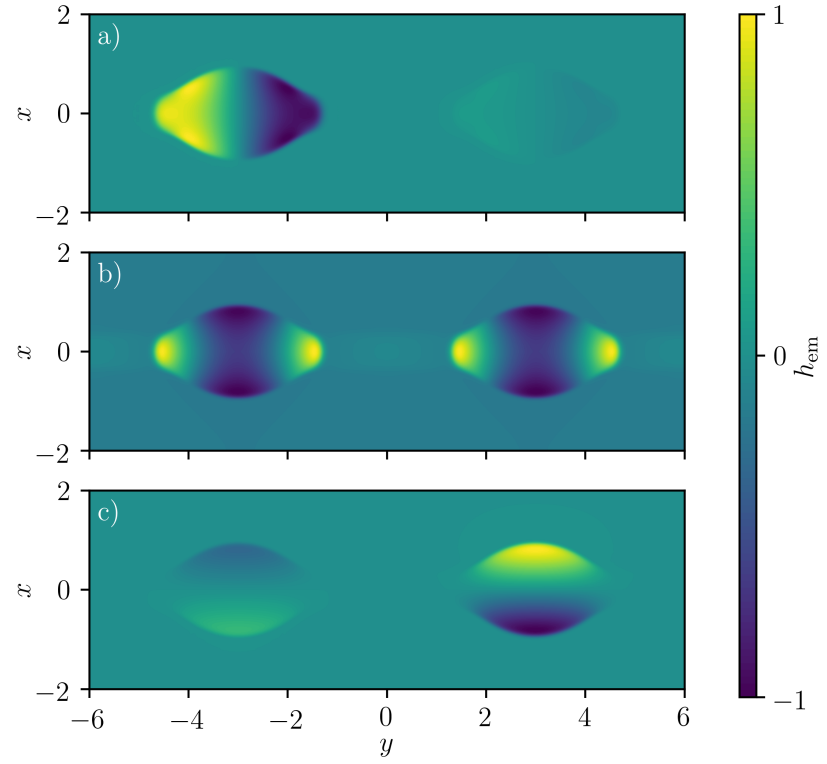

Figure B.2: Eigenmodes of the stabilized two bulges state discussed in section 4.2.2.2. a) and c) correspond to a movement of one of the bulges parallel and orthogonal to the stripe pattern, respectively. b) corresponds to the formation of a liquid ridge. The associated eigenvalues are a) $\lambda = -5 \cdot 10^{-5}$, b) $\lambda = -0.07$ and c) $\lambda = -0.07$.

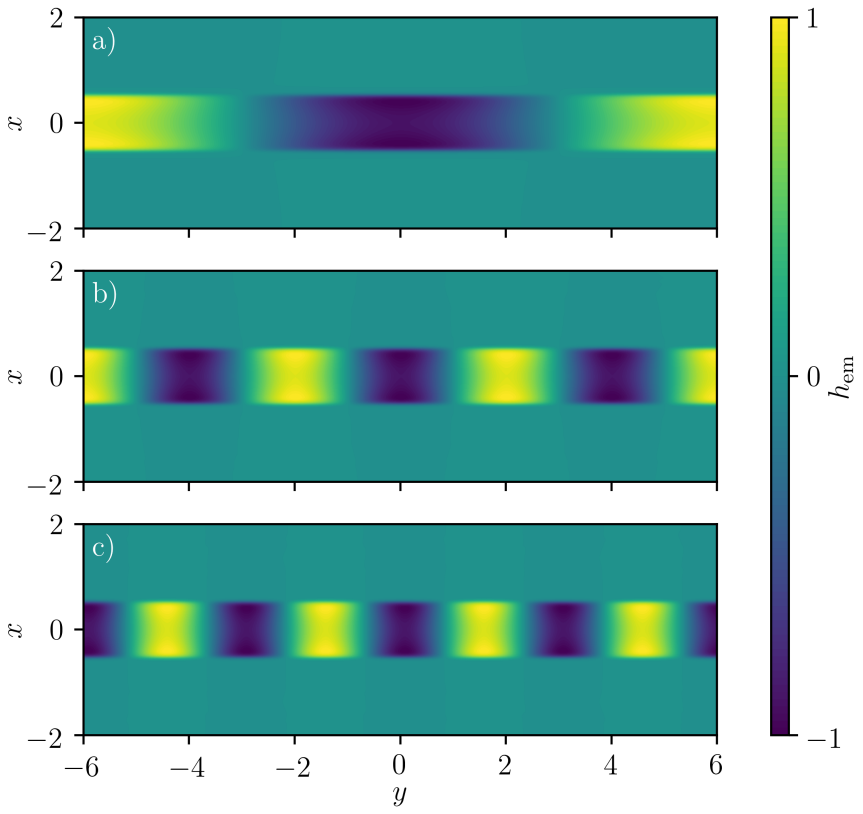

Figure B.3: Eigenfunctions of the stabilized ridge state discussed in section 4.2.2.2. a), b) and c) correspond to the formation of one, three, and four bulges, respectively. The associated eigenvalues are a) $\lambda = 5 \cdot 10^{-3}$, b) $\lambda = -16 \cdot 10^{-4}$ and c) $\lambda = -6 \cdot 10^{-2}$.

B.2 PEARLING INSTABILITY

This section includes snapshots of the different regimes of the pearling instability observed for a droplet flowing down an incline. It is an extension to the consideration of section 5.1.
Figure B.4 shows snapshots of two droplets flowing down an incline. The droplet in the upper row (panel a) and b)) has an initial film height of $h_0 = 1.846$ while for the droplet on the bottom row (panel c) and d)), $h_0 = 2.215$ was chosen. Both heights, i. e., volumes are below the critical value, thus, no pearling instability occurs. While the images on the left represent the initial condition at $t = 0$, the images on the right display the liquid profile for $t = 140$. One can see that the increased height of the bottom droplet leads to a more pronounced deformation and an increased sliding speed. The smaller droplet retains a circular base area while the larger droplet forms a cusp, i. e., an elongation opposing the direction of movement. Both shapes remain stable, such that due to the periodic boundary conditions the droplets slide down the incline, retaining their shape for all times.
Increasing the initial film height, the droplet becomes unstable once some critical value is surpassed. Analogous to the droplet portrayed in the bottom row of fig. B.4, a cusp forms, as the liquid adapts to the inclined substrate. In contrast to fig. B.4 d), however, this state does not remain stable but the elongation process continues, resulting in the formation of a tail. The tail elongates further, as it accumulates an increasing amount of liquid, resulting in a pinch-off and the formation of two separate droplets. The corresponding state is displayed in fig. B.5 for $h_0 = 2.26$ and $\alpha = 65°$. Both droplets flow down the incline. If the volume of the main droplet remains above the critical value after the emission of a satellite, the main droplet can emit another satellite droplet. The height profile after the emission of a second satellite is displayed in fig. B.5 b). Due to the larger volume of the main droplet, it can move down the incline more quickly and thus catch up with the emitted satellite droplets. After the recombination of the droplets, the process repeats itself in a cyclic behavior. Through the application of periodic boundary conditions the pearling instability, therefore, results in a pearling-coalescence cycle [12].
Note that for initial heights slightly above the critical value only a single satellite droplet should be emitted. However, using an inclination angle of $\alpha = 65°$, it was not possible to determine this region of h_0. This is partly due to the increased numerical cost since the integration time before the onset of the pearling instability steeply increases close to the critical region. For the simulation displayed in fig. B.5, i. e., $h_0 = 2.6$ the first satellite is emitted after roughly 36000 time-steps at $t \approx 2600$, compared to only 2600 time-steps for $h_0 = 2.46$ shown in fig. B.6. For $h_0 = 2.46$ three satellites are emitted during a single cycle. The states displayed in panels a), b) and c) of fig. B.6 were obtained

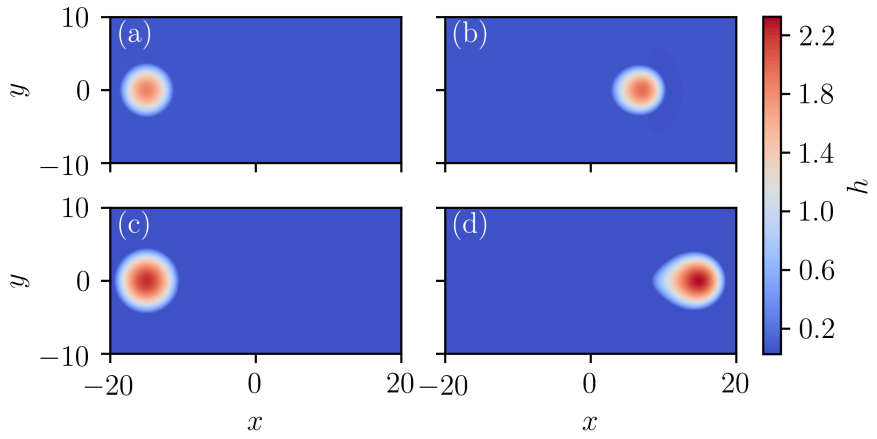

Figure B.4: Snapshots obtained during direct numerical simulations of a liquid droplet on an incline with $\alpha = 65°$. a) and b) show a droplet with the initial height $h_0 = 1.846$ at $t = 0$ and at $t = 140$ respectively. On the bottom row c) shows an initial droplet with $h_0 = 2.215$ while d) shows the same droplet after $t = 140$. The wettability is homogeneous with $\omega(\mathbf{x}, t) = 0$.

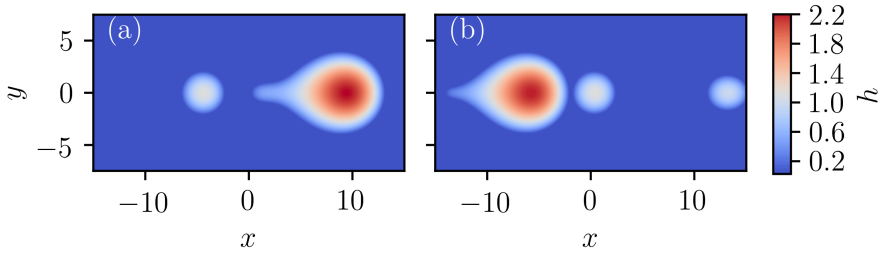

Figure B.5: Snapshots obtained by direct numerical simulations of liquid droplet with $h_0 = 2.26$ on an incline with $\alpha = 65°$. a) and b) show the liquid profile after the emission of one and two satellite droplets respectively. For larger times the main droplet catches up with the satellites and a new cycle starts.

shortly after the emission of one, two, and three satellites, respectively.

The number of emitted satellites during a single cycle increases with increasing initial film heights h_0 until new dynamics arise once the initial film height crosses a second threshold value. Due to the employed periodic boundary conditions, the droplet can connect to itself once its elongation reaches the domain length in x-direction L_x. Snapshots obtained during the simulation of a droplet with an initial height above this critical value are shown in fig. B.7. Here a) shows the liquid film after some time on the substrate. The droplet has formed a tail spanning almost the entire domain and it is apparent that if the elongation would continue, a pearling instability would occur and two separate droplets would form. Due to the finite size of the domain and the applied periodic boundary conditions, the satellite droplet does

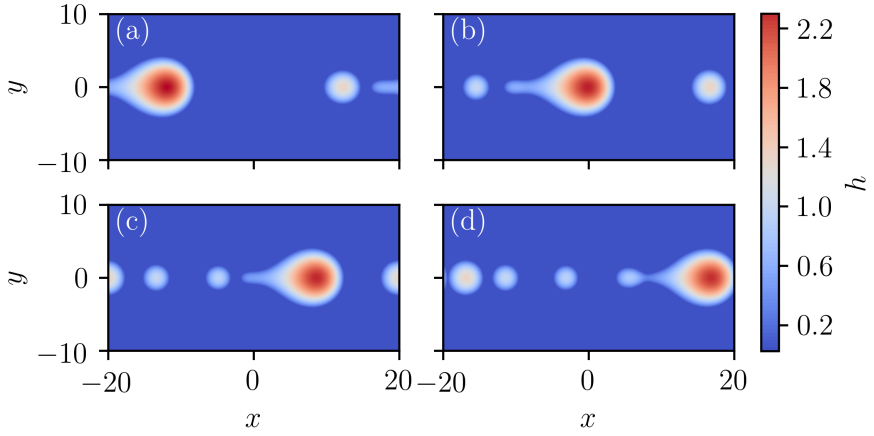

Figure B.6: Snapshots obtained by direct numerical simulations of a liquid droplet on an incline with the inclination angle $\alpha = 65°$ and an initial height of $h_0 = 2.46$. a) b) and c) show the liquid profile after the emission of one, two, and three satellite droplets respectively. Before the emission of a fourth satellite, the droplet reaches the initially emitted droplet. The state shortly before the reconnection with the initially emitted satellite is shown in d).

not pinch off but rather connects with itself, as the front of the droplet gets in contact with the end of its tail. This results in the formation of an inhomogeneous liquid ridge. Over time the inhomogeneities become smoother, such that surface waves form. These are portrayed in fig. B.7 b). The thickened part of the ridge continues to move down the incline with a velocity about 20% larger than the initial droplet's velocity. The increase in velocity stems from the fact, that the substrate is already covered by a relatively thick liquid layer, thus, the liquid can move more quickly down the incline.
A cross-section of the surface waves state (c.f. fig. B.7 b)) is portrayed in fig. B.8. The profile of the film consists of a homogeneous film of the height $h \approx 1$ with an additional droplet on top. Over time, only the droplet on top moves whereas the underlying film remains constant.
Dynamics, analogous to the ones along the cross section at $y = 0$ for the two-dimensional droplet of height $h_0 = 2.8$, can be observed for a one-dimensional droplet on an inclined substrate. Choosing the same parameters as for the two-dimensional case and a domain length $L = L_x$, one can again observe the formation of surface waves as is shown in fig. B.9. In contrast to the two-dimensional case, the amplitude of the one-dimensional surface waves decreases over time, such that for large times the liquid assumes the shape of a homogeneous film.

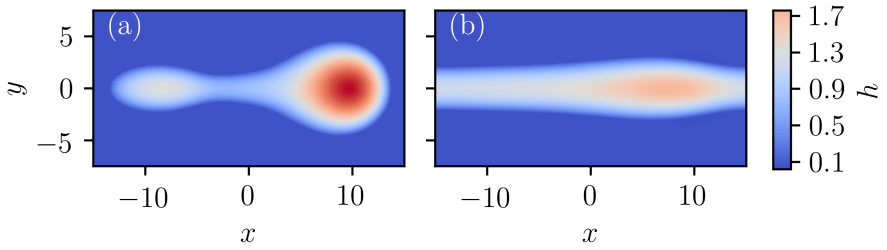

Figure B.7: Snapshots obtained by direct numerical simulations of a liquid droplet on an incline with the inclination angle $\alpha = 65°$ and an initial height of $h_0 = 2.8$. a) portrays the liquid after $t = 126$. The liquid has significantly elongated and a pronounced tail has formed. b) shows the liquid at $t = 1128$. The liquid has reconnected with itself such that an inhomogeneous liquid ridge parallel to the x-axis has formed.

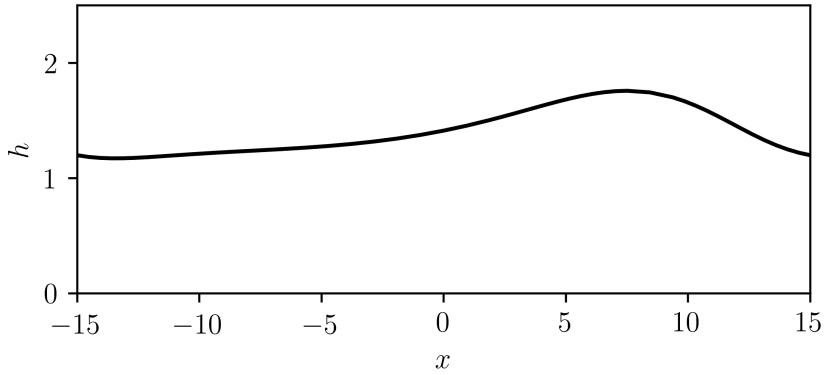

Figure B.8: Cross section along the x-axis for $y = 0$ of the surface waves state shown in fig. B.7.

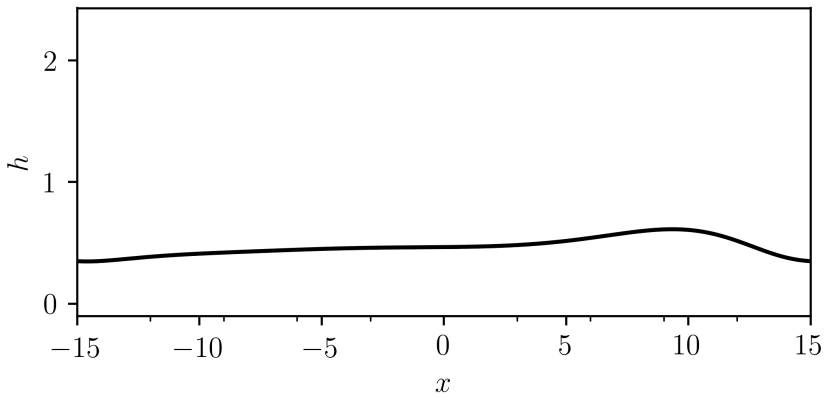

Figure B.9: Snapshot of a surface wave state obtained during the simulation of a one-dimensional system. As the initial condition a liquid droplet given by eq. (3.10) with $h_0 = 2.8$ was chosen and the domain size was set to $L = 30$, analogously to the two dimensional simulation portrayed in fig. B.7. All other parameters are chosen as they are in fig. B.7.

B.3 LIQUID RIDGE ON AN INCLINED SUBSTRATE

In an attempt to directly extend one-dimensional results (c.f. section 4.1) of a droplet on an inclined substrate, a liquid ridge with $h_0 = 2.3$ was simulated on an incline. The orientation of the ridge was chosen such that it is orthogonal to the direction of inclination. The inclination angle is again chosen as 65° and the wettability $\omega(\mathbf{x}, t) = 1$ is employed. The simulation is performed on a domain with $L_x \times L_y = 30 \times 15$. Note that periodic boundary conditions are in place such that the simulated ridge corresponds to a part of an infinitely long ridge.
Snapshots of the performed direct numerical simulation are portrayed in fig. B.10. The initial state of a homogeneous ridge with the height $h_0 = 2.3$ is shown in fig. B.10 a). Note that the ridge has not yet adapted to the substrate and is completely symmetrical along $x = 0$. For increasing times the ridge adapts to the substrate and elongates analogous to a single droplet (cf. fig. B.4 d). Initially, this elongation process does not affect the homogeneity of the ridge. After some time, however, the ridge starts to deform, resulting in a curved advancing contact line. This state is portrayed in fig. B.10 b). In a Plateau-Rayleigh-like instability, the deformation grows over time. Due to the height decrease of the liquid around $y = 0$, it moves more slowly down the incline, thus, lagging behind the larger liquid structure at the boundary. Additionally, the structure at the boundary also undergoes an elongation process. The corresponding snapshot is shown in fig. B.10 c). Analogous to fig. B.7, the structure at the boundary contains enough liquid to elongate over the entire domain without the emission of satellite droplets. The state shortly before the front part of the droplet connects with its own tail is portrayed in fig. B.10 d), while the state after the connection is shown in fig. B.10 e). Note that the latter corresponds to the surface waves states portrayed in fig. B.7 b). In contrast to the dynamics observed there, the surface waves do not remain stable here, but rather dissipate, leading to a formation of a homogeneous ridge parallel to the inclination. In total, the ridge has, therefore, changed its orientation and is now aligned with the inclination.

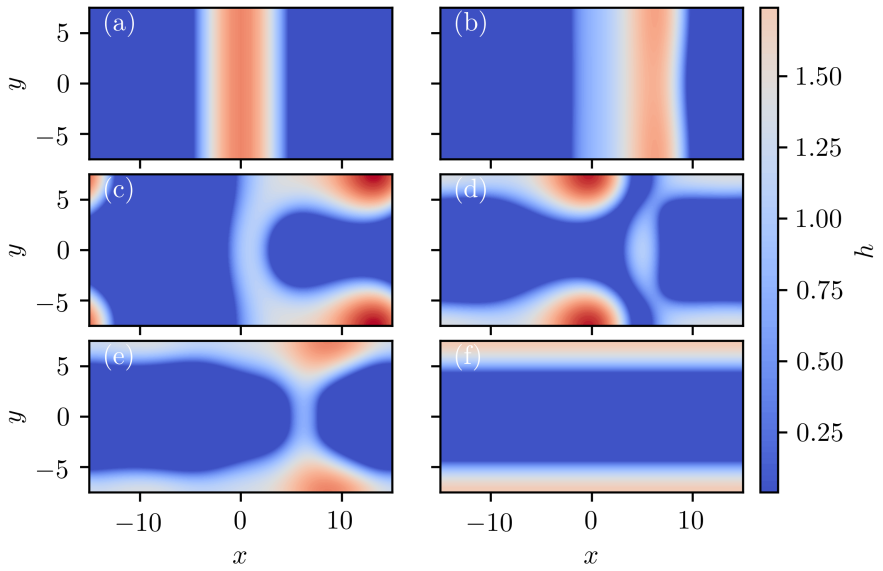

Figure B.10: Snapshots of the height profile during the simulation of a homogeneous ridge on an inclined substrate with the inclination angle $\alpha = 65°$. a) shows the initial state of a homogeneous ridge with the height $h_0 = 2.3$ oriented orthogonal to the direction of inclination. b) shows the liquid profile after it has adapted to the substrate with a slightly curved right contact line. The deformation leads to a formation of an elongated droplet at the boundary with a liquid stripe connecting the tails of the two halves shown in c). The elongation process continues resulting in the state shown in d) and ultimately leads to the connection of the droplet with itself shown in e). The resulting surface waves dissipate, resulting in the homogeneous ridge state shown in f).

BIBLIOGRAPHY

[1] Philippe Beltrame, Edgar Knobloch, Peter Hänggi, and Uwe Thiele. "Rayleigh and depinning instabilities of forced liquid ridges on heterogeneous substrates." In: *Phys. Rev. E* 83 (1 Jan. 2011), p. 016305. ISSN: 1539-3755. DOI: 10.1103/PhysRevE.83.016305. URL: https://link.aps.org/doi/10.1103/PhysRevE.83.016305.

[2] I. Berbezier, M. Aouassa, A. Ronda, L. Favre, M. Bollani, R. Sordan, A. Delobbe, and P. Sudraud. "Ordered arrays of Si and Ge nanocrystals via dewetting of pre-patterned thin films." In: *Journal of Applied Physics* 113.6 (2013), p. 064908. ISSN: 0021-8979. DOI: 10.1063/1.4790713.

[3] Daniel Bonn, Jens Eggers, Joseph Indekeu, Jacques Meunier, and Etienne Rolley. "Wetting and spreading." In: *Reviews of Modern Physics* 81 (2 2009), pp. 739–805. ISSN: 0034-6861. DOI: 10.1103/RevModPhys.81.739. URL: https://link.aps.org/doi/10.1103/RevModPhys.81.739.

[4] Dietrich Braess. *Finite Elemente - Theorie, schnelle Löser und Anwendungen in der Elastizitätstheorie*. Springer Berlin Heidelberg, 2007, pp. 275–352. ISBN: 978-3642347962. DOI: 10.1007/978-3-642-34797-9_6.

[5] Lutz Brusch, Heiko Kühne, Uwe Thiele, and Markus Bär. "Dewetting of thin films on heterogeneous substrates: Pinning versus coarsening." In: *Physical Review E* 66.1 (2002), p. 011602.

[6] Manoj K. Chaudhury and George M. Whitesides. "How to Make Water Run Uphill." In: *Science* 256.5063 (1992), pp. 1539–1541. ISSN: 0036-8075. DOI: 10.1126/science.256.5063.1539. URL: https://science.sciencemag.org/content/256/5063/1539.

[7] Anton A Darhuber, Sandra M Troian, Jeffrey M Davis, Scott M Miller, and Sigurd Wagner. "Selective dip-coating of chemically micropatterned surfaces." In: *Journal of Applied Physics* 88.9 (2000), pp. 5119–5126.

[8] Pierre-Gilles De Gennes. "Wetting: statics and dynamics." In: *Reviews of modern physics* 57.3 (1985), p. 827.

[9] B. V. Derjaguin, N. V. Churaev, V. M. Muller, and VI Kisin. *Surface forces*. 1st ed. Springer New York, NY, 1987. DOI: 10.1007/978-1-4757-6639-4.

[10] Peter Deuflhard. *Newton methods for nonlinear problems: affine invariance and adaptive algorithms*. Vol. 35. Springer Science & Business Media, 2005.

[11] Siegfried Dietrich. "Wetting phenomena." In: *Phase transitions and critical phenomena*. Academic Press, 1988, pp. 1–218.

[12] Sebastian Engelnkemper. "Nichtlineare Analyse physikochemisch getriebener Entnetzung - Statik und Dynamik." PhD thesis. Westfälische Wilhelms-Universität Münster, 2017.

[13] Sebastian Engelnkemper and Uwe Thiele. "The collective behaviour of ensembles of condensing liquid drops on heterogeneous inclined substrates." In: *EPL (Europhysics Letters)* 127.5 (2019), p. 54002.

[14] Sebastian Engelnkemper, Markus Wilczek, Svetlana V. Gurevich, and Uwe Thiele. "Morphological transitions of sliding drops: Dynamics and bifurcations." In: *Phys. Rev. Fluids* 1 (7 Nov. 2016), p. 073901. DOI: 10.1103/PhysRevFluids.1.073901.

[15] Alexandre Ern and Jean-Luc Guermond. *Finite Elements II*. Springer, 2021.

[16] Xinjian Feng, Jin Zhai, and Lei Jiang. "The Fabrication and Switchable Superhydrophobicity of TiO2 Nanorod Films." In: *Angewandte Chemie (International ed. in English)* 44 (Aug. 2005), pp. 5115–8. DOI: 10.1002/anie.200501337.

[17] Josua Grawitter and Holger Stark. "Droplets on substrates with oscillating wettability." In: *Soft Matter* 17.41 (2021), pp. 9469–9479. DOI: 10.1039/D1SM01113H.

[18] Josua Grawitter and Holger Stark. "Steering droplets on substrates using moving steps in wettability." In: *Soft Matter* 17.9 (2021), pp. 2454–2467. DOI: 10.1039/D0SM02082F.

[19] Matthias Heil and Andrew L. Hazel. "oomph-lib – An Object-Oriented Multi-Physics Finite-Element Library." In: *Fluid-Structure Interaction*. Ed. by Hans-Joachim Bungartz and Michael Schäfer. Berlin, Heidelberg: Springer Berlin Heidelberg, 2006, pp. 19–49. ISBN: 978-3-540-34596-1.

[20] Christoph Honisch, Te-Sheng Lin, Andreas Heuer, Uwe Thiele, and Svetlana V. Gurevich. "Instabilities of Layers of Deposited Molecules on Chemically Stripe Patterned Substrates: Ridges versus Drops." In: *Langmuir* 31.38 (Sept. 2015), pp. 10618–10631. ISSN: 0743-7463. DOI: 10.1021/acs.langmuir.5b02407. URL: https://ir.nctu.edu.tw/handle/11536/128271.

[21] Christian Honnigfort, Leon Topp, Natalia García Rey, Andreas Heuer, and Björn Braunschweig. "Dynamic Wetting of Photoresponsive Arylazopyrazole Monolayers is Controlled by the Molecular Kinetics of the Monolayer." In: *Journal of the American Chemical Society* 144.9 (2022), pp. 4026–4038. DOI: 10.1021/jacs.1c12832.

[22] Kunihiro Ichimura, Sang-Keun Oh, and Masaru Nakagawa. "Light-Driven Motion of Liquids on a Photoresponsive Surface." In: *Science (New York, N.Y.)* 288 (July 2000), pp. 1624–6. DOI: 10.1126/science.288.5471.1624.

[23] Arieh Iserles. *A first course in the numerical analysis of differential equations*. 44. Cambridge university press, 2009.

[24] Kazuhiko Ishihara, Akihiko Okazaki, Naoki Negishi, Isao Shinohara, Teruo Okano, Kazunori Kataoka, and Yasuhisa Sakurai. "Photoinduced change in wettability and binding ability of azoaromatic polymer." In: *Journal of Applied Polymer Science* 27 (Jan. 1982), pp. 239 –245. DOI: 10.1002/app.1982.070270125.

[25] Peter Lenz and Reinhard Lipowsky. "Morphological Transitions of Wetting Layers on Structured Surfaces." In: *Phys. Rev. Lett.* 80 (9 Mar. 1998), pp. 1920–1923. DOI: 10.1103/PhysRevLett.80.1920. URL: https://link.aps.org/doi/10.1103/PhysRevLett.80.1920.

[26] XL Li, CX Wang, and GW Yang. "Thermodynamic theory of growth of nanostructures." In: *Progress in Materials Science* 64 (2014), pp. 121–199.

[27] G D Martin, S D Hoath, and I M Hutchings. "Inkjet printing - the physics of manipulating liquid jets and drops." In: *Journal of Physics: Conference Series* 105 (Mar. 2008), p. 012001. DOI: 10.1088/1742-6596/105/1/012001. URL: https://doi.org/10.1088/1742-6596/105/1/012001.

[28] Vladimir Mitlin. "Dewetting of Solid Surface: Analogy with Spinodal Decomposition." In: *Journal of Colloid and Interface Science* 156 (Mar. 1993), pp. 491–497. DOI: 10.1006/jcis.1993.1142.

[29] A Moosavi, M Rauscher, and S Dietrich. "Motion of nanodroplets near chemical heterogeneities." In: *Langmuir* 24.3 (2008), pp. 734–742.

[30] Alexander Oron, Stephen H. Davis, and S. George Bankoff. "Long-scale evolution of thin liquid films." In: *Reviews of Modern Physics* 69 (1997), pp. 931–980. ISSN: 0034-6861. DOI: 10.1103/RevModPhys.69.931.

[31] LM Pismen. "Nonlocal diffuse interface theory of thin films and the moving contact line." In: *Physical Review E* 64.2 (2001), p. 021603.

[32] Len M Pismen and Uwe Thiele. "Asymptotic theory for a moving droplet driven by a wettability gradient." In: *Physics of Fluids* 18.4 (2006), p. 042104.

[33] Joseph Antoine Ferdinand Plateau. *Statique expérimentale et théorique des liquides soumis aux seules forces moléculaires*. Vol. 2. Gauthier-Villars, 1873.

[34] T. Podgorski, J.-M. Flesselles, and L. Limat. "Corners, Cusps, and Pearls in Running Drops." In: *Phys. Rev. Lett.* 87 (3 June 2001), p. 036102. DOI: 10.1103/PhysRevLett.87.036102. URL: https://link.aps.org/doi/10.1103/PhysRevLett.87.036102.

[35] Lord Rayleigh. "On the instability of jets." In: *Proceedings of the London mathematical society* 1.1 (1878), pp. 4–13.

[36] Lord Rayleigh. "XIX. On the instability of cylindrical fluid surfaces." In: *The London, Edinburgh, and Dublin Philosophical Magazine and Journal of Science* 34.207 (1892), pp. 177–180.

[37] Rohit Rosario, Devens Gust, Mark Hayes, Frank Jahnke, Joseph Springer, and Antonio A. Garcia. "Photon-Modulated Wettability Changes on Spiropyran-Coated Surfaces." In: *Langmuir* 18.21 (2002), pp. 8062–8069. DOI: 10.1021/la025963l. eprint: https://doi.org/10.1021/la025963l. URL: https://doi.org/10.1021/la025963l.

[38] S Shabahang, JJ Kaufman, DS Deng, and AF Abouraddy. "Observation of the Plateau-Rayleigh capillary instability in multimaterial optical fibers." In: *Applied Physics Letters* 99.16 (2011), p. 161909.

[39] V. M. Starov and M. G. Velarde. "Surface forces and wetting phenomena." In: *J. Phys.-Condens. Matter* 21 (2009), p. 464121. DOI: 10.1088/0953-8984/21/46/464121.

[40] Moritz Stieneker. "Dynamics of droplets on switchable prestructured substrates." MA thesis. WWU Münster, Sept. 2019.

[41] Moritz Stieneker, Leon Topp, Svetlana Gurevich, and Andreas Heuer. "Multiscale perspective on wetting on switchable substrates: mapping between microscopic and mesoscopic models." In: *arXiv preprint arXiv:2108.00641* (2021).

[42] Janik Suer, Moritz Stieneker, Svetlana Gurevich, and Simon Hartmann. "Implementation of the Thin-Film Equation on Prestructured, Switchable Substrates Using the oomph-lib Library." In: (Jan. 2022). DOI: 10.5281/zenodo.5821537. URL: https://doi.org/10.5281/zenodo.5821537.

[43] Endre Süli and David F Mayers. *An introduction to numerical analysis*. Cambridge university press, 2003.

[44] Ren-De Sun, Akira Nakajima, Akira Fujishima, Toshiya Watanabe, and Kazuhito Hashimoto. "Photoinduced Surface Wettability Conversion of ZnO and TiO2 Thin Films." In: *The Journal of Physical Chemistry B* 105.10 (Mar. 2001), pp. 1984–1990. ISSN: 1520-6106. DOI: 10.1021/jp002525j. URL: https://doi.org/10.1021/jp002525j.

[45] Barna Szabó and Ivo Babuška. "Finite Element Analysis: Method, Verification and Validation." In: (2021).

[46] Walter Tewes, Oleg Buller, Andreas Heuer, Uwe Thiele, and Svetlana V. Gurevich. "Comparing kinetic Monte Carlo and thin-film modeling of transversal instabilities of ridges on patterned substrates." In: *The Journal of Chemical Physics* 146.9 (2017), p. 094704. ISSN: 0021-9606. DOI: 10.1063/1.4977739. eprint: https://doi.org/10.1063/1.4977739.

[47] Uwe Thiele. "Thin film evolution equations from (evaporating) dewetting liquid layers to epitaxial growth." In: *Journal of physics. Condensed matter : an Institute of Physics journal* 22 (Feb. 2010), p. 084019. DOI: 10.1088/0953-8984/22/8/084019.

[48] Uwe Thiele, Lutz Brusch, Michael Bestehorn, and Markus Baer. "Modelling thin-film dewetting on structured substrates and templates: Bifurcation analysis and numerical simulations." In: *The European Physical Journal E* 11 (2003), pp. 255–271. ISSN: 1292-8941. DOI: 10.1140/epje/i2003-10019-5.

[49] Leon Topp, Moritz Stieneker, Svetlana Gurevich, and Andreas Heuer. "Wetting behavior of droplets on switchable substrates: A theoretical perspective." In: *arXiv preprint arXiv:2203.13719* (2022).

[50] Sarah Christine Trinschek. "Thin-Film Modelling of Complex Fluids and Bacterial Colonies." In: ().

[51] Rajagopal Vellingiri, Nikos Savva, and Serafim Kalliadasis. "Droplet spreading on chemically heterogeneous substrates." In: *Physical Review E* 84.3 (2011), p. 036305.

[52] Rong Wang, Kazuhito Hashimoto, Akira Fujishima, Makota Chikuni, Eiichi Kojima, Atsushi Kitamura, Mitsuhide Shimohigoshi, and Toshiya Watanabe. "Light-induced amphiphilic surfaces." In: *Nature* 388.6641 (July 1997), pp. 431–432. ISSN: 1476-4687. DOI: 10.1038/41233. URL: https://doi.org/10.1038/41233.

[53] Wenchong Wang and Lifeng Chi. "Area-Selective Growth of Functional Molecular Architectures." In: *Accounts of Chemical Research* 45.10 (2012). PMID: 22830409, pp. 1646–1656. DOI: 10.1021/ar200299w. eprint: https://doi.org/10.1021/ar200299w.

[54] Wenchong Wang et al. "High-Resolution Triple-Color Patterns Based on the Liquid Behavior of Organic Molecules." In: *Small* 7.10 (2011), pp. 1403–1406. DOI: https://doi.org/10.1002/smll.201002210.

[55] Markus Wilczek. "Pattern Formation in Driven Thin Layers of Simple and Complex Liquids." PhD thesis. WWU Münster, 2016.

[56] Bingwei Xin and Jingcheng Hao. "Reversibly switchable wettability." In: *Chemical Society Reviews* 39.2 (2010), pp. 769–782.

[57] Fei Zhu, Shiliang Tan, Manivannan Kalavathi Dhinakaran, Jing Cheng, and Haibing Li. "The light-driven macroscopic directional motion of a water droplet on an azobenzene-calix[4]arene modified surface." In: *Chem. Commun.* 56 (74 2020), pp. 10922–10925. DOI: 10.1039/D0CC00519C. URL: http://dx.doi.org/10.1039/D0CC00519C.

DECLARATION

I hereby confirm that this thesis on "Spatio-Temporal Control of Thin Liquid Films on Switchable Substrates" is solely my own work and that I have used no sources or aids other than the ones stated. All passages in my thesis for which other sources, including electronic media, have been used, be it direct quotes or content references, have been acknowledged as such and the sources cited.
I agree to have my thesis checked in order to rule out potential similarities with other works and to have my thesis stored in a database for this purpose.

Münster, September 23, 2022

Janik Suer